The roles of pyroxenite and peridotite in the mantle sources of oceanic basalts

Andrew K. Matzen[1*]

Bernard J. Wood[1]

Michael B. Baker[2]

Edward M. Stolper[2]

[1]University of Oxford, Department of Earth Sciences, Oxford, UK OX1 3AN.

[2]California Institute of Technology, Pasadena, CA 91125

*Corresponding author.

E-mail: andrew.matzen@earth.ox.ac.uk

Accepted in Nature Geoscience

May 11, 2017

Abstract

Subduction of oceanic crust generates chemical and lithological heterogeneities in the mantle. An outstanding question is the extent to which these heterogeneities contribute to subsequent magmas generated by mantle melting, but the answer differs depending on the geochemical behavior of the element(s) being investigated: incompatible elements (those that preferentially concentrate into silicate melts) suggest that recycled oceanic crust is an important contributor, while compatible elements (those that concentrate in crystalline residues) generally do not. Recently, however, the concentrations of Mn and Ni — two elements of varying compatibility— in early-crystallizing olivines, have been used to infer that erupted magmas are mixtures of partial melts of olivine-rich mantle rocks (i.e., peridotite) and of metasomatic pyroxene-rich mantle rocks (i.e., pyroxenite) formed by interaction between partial melts of recycled oceanic crust and peridotite. Here, we test whether melting of peridotite alone can explain the observed trend in olivine compositions by combining new experimental data on the partitioning of Mn between olivine and silicate melt under conditions relevant to basalt petrogenesis with earlier results on Ni partitioning. We show that the observed olivine compositions are consistent with melts of fertile peridotite at various pressures—importantly, melts from metasomatic pyroxenites are not required. Thus although recycled materials may well be present in the mantle source regions of some basalts, the Mn and Ni data can be explained without such a contribution. Furthermore, the success of modeling the Mn-Ni contents of olivine phenocrysts as low-pressure crystallization products of partial melts of peridotite over a range of pressures implies a simple new approach for constraining depths of mantle melting.

Main Text

The process of subduction recycles basaltic oceanic crust into the peridotitic mantle, generating pronounced chemical and lithological heterogeneities. A major geochemical question is the extent to which the more fusible basaltic components contribute to subsequent magmas generated by the upwelling of this "marble-cake"[1] mantle under mid-ocean ridges (MOR) and/or ocean islands[2,3]. For the most part, this question has been addressed using isotopic and incompatible trace elements (e.g., ref. 4,5). Recently, this problem has also been addressed by analyzing olivine (ol) phenocrysts from basalts[6,7]. At a given primitive olivine Mg# (Mg/[Mg+Fe], atomic), the Ni and Mn contents of olivines are inversely correlated (Fig. 1, see methods for calculation). Figure 1 shows this correlation for NiO_{89} and MnO_{89} in olivine phenocrysts from igneous provinces worldwide (where 89 indicates that MnO and NiO are corrected to an Mg# of 0.89). Further, Ni and Mn contents in primitive olivines are correlated with lithospheric thickness[6] (qualitatively shown in Fig. 1), and any successful model must also explain this.

One possible explanation of the correlations between Ni and Mn contents of olivines and of both with lithospheric thickness relates to the fate of recycled basaltic crust during mantle upwelling. It has been argued that the basaltic component begins to melt first[8], generating a silica-rich melt that infiltrates and reacts with the surrounding peridotite, producing a metasomatic pyroxene-rich rock with (relative to other pyroxenites) high bulk Ni (e.g., ref. 9). Later melting of this metasomatic, or second-stage, pyroxenite would generate Ni-rich, Mn-poor melts that, when mixed with partial melts of the peridotite, precipitate olivines with Ni and Mn contents that correlate with the amount of melt contributed by the pyroxenite source. Using this framework, it has been estimated that recycled oceanic crust is responsible for ~17% of the volume of mid-ocean ridge basalts and ~60% of basalts erupted through thick (>70 km) lithosphere[6]. The

correlation with lithospheric thickness is suggested to arise from the fact that, at fixed mantle potential temperature, pyroxenite generally starts to melt at a higher pressure than peridotite[10]; thus, in regions under thick lithosphere where the mean depth of melting is higher, melts would be expected to contain a greater proportion of liquid derived from melting of pyroxenite. However, it is important to note that alternative hypotheses have been proposed to explain the observed variations in Ni and Mn (for example, refs 11–15).

Given the potential importance of the pyroxenite-melting hypothesis for mantle temperature structure and for understanding the generation of basaltic magmas, our aim is to test whether a simple alternative model involving only partial melts of peridotite produced at different pressures can reproduce the inverse correlation seen in Fig. 1. Specifically, we combine our new data on Mn partitioning with recently published results for Ni[15,16] and calculate how these elements are expected to vary during partial melting of peridotite and then, using the same partitioning models, predict the compositions of olivine phenocrysts that precipitate when these melts cool at (or near) the Earth's surface.

Mn partitioning

We measured Mn concentrations of experimentally-produced coexisting olivine and basaltic glass using high-current (100–200 nA) electron microprobe analyses[16,17]; the measurements and the resulting partition coefficients are given in Table 1. These experiments can be considered in two groups: the first comprises one-atmosphere experiments on a synthetic analog of a Hawaiian picrite[17]. The second comprises several sets of experiments where, within each set, temperature and pressure were varied such that liquid and olivine compositions are approximately constant, resulting in data over a range of temperatures for liquids with ~12, 15, 18 and 21 wt. % MgO. In

Fig. 2 we show the resulting olivine-liquid partition coefficients. For each constant-MgO series, $D_{Mn}^{ol/liq}$(MnO^{olivine}/MnO^{liquid}, by wt.) is roughly constant and independent of temperature. However, the partition coefficient depends on melt composition, decreasing from 0.94 at ~12 wt. % MgO^{liq} to 0.55 at ~24 wt. % MgO^{liq}; these systematics agree with previous results from simple systems[18]. Such partition coefficients often depend on both melt and olivine composition[19], but exchange coefficients (a ratio of two partition coefficients of elements with equal valences) are generally less sensitive to phase composition and temperature[20,21]. In this case we define the olivine-liquid exchange coefficient, K_D, as the ratio of the partition coefficients of Mn to Mg ($K_{D,Mn-Mg}^{ol/liq} = D_{Mn}^{ol/liq}/D_{Mg}^{ol/liq}$). Data from the literature (both low- and high-precision) as well as the new measurements reported here, which are consistent with previously reported high-precision data, are shown in Supplemental Information Fig. S1. We parameterized $lnK_{D,Mn-Mg}^{ol/liq}$ in terms of the MgO content of the liquid (see methods for a discussion of the rationale for this functional form):

$$lnK_{D,Mn-Mg}^{ol/liq} = 0.0088 \pm 0.0013(\mathrm{MgO}^{liq}) - 1.503 \pm 0.023, \quad (1)$$

which recovers the experimentally-measured $D_{Mn}^{ol/liq}$ with an average error of 6% (relative). The corresponding equation for Ni has been shown to depend on temperature but not the MgO content of the liquid[15,16]:

$$lnK_{D,Ni-Mg}^{ol/liq} = \frac{4505 \pm 196}{T(K)} - 2.075 \pm 0.120 \quad (2)$$

Modeling peridotite melting

In order to examine alternatives to the hypothesis that the varying Mn and Ni concentrations of olivine phenocrysts are due to differing amounts of melt derived from metasomatic pyroxenite in their mantle sources, we began by considering melting of peridotite in the absence of pyroxenite. We forward-modeled melting of fertile mantle peridotite as follows: modal abundances, phase compositions, and temperatures were taken from experiments in which isobaric partial melting of peridotite was investigated at 1, 3, 4, and 4.5 GPa[22-25]; MnO and NiO contents of residual olivines were calculated using the olivine-liquid expressions given above; olivine-mineral [orthopyroxene (opx), clinopyroxene (cpx), spinel (sp), and garnet (gt)] partitioning expressions were fit to data from the literature (see methods); and whole-rock MnO and NiO contents were taken to be 0.131 wt. % and 0.25 wt. % respectively[26] (see methods). The analyses of phases in high-pressure peridotite melting experiments and in peridotite xenoliths show that olivine is the principal host for Mn and Ni in the upper mantle but that, in the garnet stability field, garnet can exert an important control on Mn partitioning between residual solids and coexisting melt (e.g., ref. 25).

With increasing degrees of partial melting at constant pressure, the Mg# of the residual olivine increases, and our calculations show that its MnO content decreases and its NiO content increases slightly (Fig. 3). And as shown in Fig. 3a, with increasing pressure at fixed olivine Mg#, the modeled MnO content of residual olivine decreases. There are two factors contributing to this pressure dependence. First, low-degree partial melts of peridotite become progressively richer in MgO as pressure increases[27,28], which is caused by a decrease in $D_{Mg}^{ol/liq}$ with increasing pressure and temperature at constant olivine Mg#. Because the $K_{D,Mn-Mg}^{ol/liq}$, which is defined as $D_{Mn}^{ol/liq}/D_{Mg}^{ol/liq}$, can be approximated as a constant (see equation 1), a decreasing $D_{Mg}^{ol/liq}$ with

increasing pressure means that $D_{Mn}^{ol/liq}$ must also decrease, resulting in the decreasing Mn content of the residual olivine with increasing pressure at constant olivine Mg# shown in Fig. 3a. The second factor contributing to the model decrease in MnO content of residual olivine with pressure is the appearance of garnet at the expense of spinel + pyroxene at ~3 GPa. Mn is appreciably more compatible in garnet than in either orthopyroxene or clinopyroxene (see methods); consequently, stabilization of garnet in the residue of melting at high pressure sequesters Mn relative to the coexisting olivines and pyroxenes, contributing to lower Mn contents in these phases. Finally, we note that the calculations presented here assume isobaric batch melting when, in reality, mantle melting is most likely nearly adiabatic (i.e., polybaric) and at least fractional to some degree (e.g., ref. 29). Despite these simplifications, the results of our calculations are still applicable because the style of melting has little effect on the concentrations of elements (like Mn and Ni) whose bulk partition coefficients are between ~0.5 and 10 (e.g., ref. 30); thus, even if eruptive products represent fractional melts accumulated from a range of pressures, systematics similar to those shown in Fig. 3 are expected (with the caveat that the most relevant pressure in the figure equivalent to Fig. 3 for integrated fractional melting would be the mean pressure of melting e.g., ref. 31).

Olivine phenocryst compositions

We took the results of our forward model of batch peridotite melting and assumed that the partial melts separate from the mantle residue at the pressure of melting; ascend to low pressure without significant olivine crystallization; and then precipitate forsterite-rich olivine on cooling at low pressure, near-surface conditions (e.g., at Hawaii, where magma transits a thick lithosphere, olivine crystallizes dominantly at low pressures based on the volatile contents of forsteritic olivine-hosted melt inclusions; e.g., ref. 32,33). For MnO, we see from equation 1 that the MnO

contents of such near-surface olivines should, at fixed MgO^{liq}, be the same as those in the residue from which the melt separated. Unlike Mn, however, the partitioning of Ni between olivine and silicate melt is temperature dependent (equation 2), and thus the temperature drop between high-pressure melting and low-pressure crystallization will result in near-liquidus, near-surface olivines with higher NiO contents than those left in the residue after high-pressure melting[16]. Temperatures of olivine saturation at 1 bar were estimated using olivine-melt equilibria[34], allowing the calculation of $D_{Ni}^{ol/liq}$ at low-pressure[15,16], which is all that is then need to calculate the NiO contents of near-liquidus olivines that crystallize as primitive magmas cool as they near the Earth's surface. Finally, we corrected our predicted olivine compositions down from the 1 bar liquidus to the point in the liquid line of descent at which Mg# 0.89 olivines are in equilibrium with the residual liquid. In order to do this objectively, we used the same median NiO and MnO vs. Mg# slopes used to correct the natural olivine data[6,35] (3.093 and –1.441, respectively; see methods) to make this correction.

Figure 4 shows that the NiO_{89} and MnO_{89} contents of $Mg\#_{89}$ olivines predicted to crystallize at low pressure from partial melts of peridotite based on our modeling generate a negative trend of NiO_{89} versus MnO_{89} that corresponds well to the trend observed in the natural phenocryst data.

As emphasized by Sobolev and coworkers[6], a key feature of the natural dataset is that olivines that erupt on thick lithosphere (e.g., Hawaii) tend to have high NiO_{89} and low MnO_{89} contents, while olivines with lower NiO_{89} and higher MnO_{89} contents tend to come from eruptions onto thinner lithosphere (e.g., MORBs). Our model of melting of a peridotite-only source—captures this behavior: i.e., as the pressure of melting increases, we predict that olivines that crystallize at low pressures will have progressively higher NiO_{89} and lower MnO_{89}, suggesting that significant contributions from a metasomatic pyroxenite[6] are not *required* to explain this trend. An

important consequence of this is that if basalts are, in fact, largely sourced by peridotites as assumed in our modeling, the Ni and Mn contents of $Mg\#_{89}$ olivines can provide quantitative constraints on the depth of peridotite melting leading to their parental magmas. We must emphasize, however, that our Mn and Ni modeling does not exclude the presence of metasomatic pyroxenite — either as a separate lithology or as an intimate mixture — in the peridotite sources of the basalts plotted in Fig. 1. We return to this point below.

In Fig. 5, we compare the NiO_{89}/MnO_{89} ratios of our model results (colored bars) with the subset of natural olivine phenocrysts (gray symbols) previously shown in Fig. 1 for which the depth to the lithosphere-asthenosphere boundary at the time of eruption is well-constrained[15,36]. The overlap between the trends in the natural data and our model results again suggests that the Ni and Mn contents of the olivines considered here can be explained by partial melts of fertile peridotites segregating from their residues at pressures corresponding to the lithosphere-asthenosphere boundary, without requiring any significant component of pyroxenite melting.

In contrast to the peridotite melting model we present, pyroxenite melting models (including both models of melting of metasomatic pyroxenite as described above and melting of basaltic rocks and their cumulates within the eclogite facies) have many free parameters, including initial pyroxenite composition, degree of partial melting, details and extent of reaction between melts of recycled crust and the surrounding peridotite, and details of how mixing occurs between melts from peridotite and pyroxenite source rocks. Considering the possible ranges of these parameters, judicious choices would likely be able to reproduce the NiO_{89}-MnO_{89} trends of Figs. 1 and 4. Nevertheless, we emphasize that the standard (and far simpler and better constrained) reference model based on partial melting of fertile peridotite as the dominant process contributing to basaltic melts worldwide reproduces the Ni-Mn trends seen in the natural olivine

phenocryst data. Although explaining these data was a prime motivation in the development of more complex models involving metasomatic pyroxenite, a key finding is that such models are not required to explain the main trend of these data. Note that we do not assert that source regions of basalts are uniform in composition: Compositional heterogeneities in the mantle, including the presence of pyroxene-rich lithologies, have been widely invoked to explain other aspects of the chemical and isotopic variability of basaltic magmas e.g., ref. 3,4,37-39. Some of the scatter, and some of the systematic behavior, observed in Figs. 1 and 4 could be due to compositional heterogeneities of peridotites and/or the presence of lithologically distinct recycled components (e.g., pyroxenites) in their sources. However, at Hawaii, trace element and isotopic evidence has been used to suggest that compositional heterogeneities are not segregated into a separate pyroxene-rich lithology (e.g., ref. 40,41; for an alternative view, see, for example, ref. 42). Regardless of the physical state of the recycled components in the sources of oceanic basalts, these pyroxenitic components are not needed to explain the first-order systematics observed in the MnO and NiO contents of olivine phenocrysts. Thus, despite the requirement (informed by isotopes and trace elements) for recycled material in the mantle, major and minor elements (including the Ni and Mn contents of olivines[43]) are consistent with a source that is dominantly peridotitic.

References:

1 Allègre, C. J. & Turcotte, D. L. Implications of a two-component marble-cake mantle. *Nature* **323**, 123-127 (1986).

2 White, W. M. Oceanic Island Basalts and Mantle Plumes: The Geochemical Perspective. *Annual Review of Earth and Planetary Sciences* **38**, 133-160, (2010).

3 Hofmann, A. W. Mantle geochemistry: the message from oceanic volcanism. *Nature* **385**, 219-229 (1997).

4 Stracke, A., Bizimis, M. & Salters, V. J. M. Recycling oceanic crust: Quantitative constraints. *Geochemistry, Geophysics, Geosystems* **4**, 8003 (2003).

5 Willbold, M. & Stracke, A. Trace element composition of mantle end-members: Implications for recycling of oceanic and upper and lower continental crust. *Geochemistry, Geophysics, Geosystems* **7**, Q04004 (2006).

6 Sobolev, A. V. *et al.* The amount of recycled crust in sources of mantle-derived melts. *Science* **316**, 412-417 (2007).

7 Sobolev, A. V., Hofmann, A. W., Sobolev, S. V. & Nikogosian, I. K. An olivine-free mantle source of Hawaiian shield basalts. *Nature* **434**, 590-597 (2005).

8 Hirschmann, M. M. & Stolper, E. M. A possible role for garnet pyroxenite in the origin of the "garnet signature" in MORB. *Contributions to Mineralogy and Petrology* **124**, 185-208 (1996).

9 Kelemen, P. B., Hart, S. R. & Bernstein, S. Silica enrichment in the continental upper mantle via melt/rock reaction. *Earth and Planetary Science Letters* **164**, 387-406 (1998).

10 Lambart, S., Baker, M. B. & Stolper, E. M. The role of pyroxenite in basalt genesis: Melt-PX, a melting parameterization for mantle pyroxenites between 0.9 and 5 GPa. *Journal of Geophysical Research: Solid Earth* **121**, 5708-5735 (2016).

11 Li, C. & Ripley, E. M. The relative effects of composition and temperature on olivine-liquid Ni partitioning: Statistical deconvolution and implications for petrologic modeling. *Chemical Geology* **275**, 99-104 (2010).

12 Niu, Y., Wilson, M., Humphreys, E. R. & O'Hara, M. J. The origin of intra-plate ocean island basalts (OIB): the lid effect and its geodynamic implications. *Journal of Petrology* **52**, 1443-1468 (2011).

13 Wang, Z. & Gaetani, G. A. Partitioning of Ni between olivine and siliceous eclogite partial melt: experimental constraints on the mantle source of Hawaiian basalts. *Contributions to Mineralogy and Petrology* **156**, 661-678 (2008).

14 Ryabchikov, I. D. High NiO content in mantle-derived magmas as evidence for material transfer from the Earth's core. *Doklady Earth Sciences* **389A**, 437-439 (2003).

15 Matzen, A. K., Baker, M. B., Beckett, J. R., Wood, B. J. & Stolper, E. M. The effect of liquid composition on the partitioning of Ni between olivine and silicate melt. *Contributions to Mineralogy and Petrology* **172**, 3 (2017).

16 Matzen, A. K., Baker, M. B., Beckett, J. R. & Stolper, E. M. The Temperature and Pressure Dependence of Nickel Partitioning between Olivine and Silicate Melt. *Journal of Petrology* **54**, 2521-2545 (2013).

17 Matzen, A. K., Baker, M. B., Beckett, J. R. & Stolper, E. M. Fe–Mg partitioning between olivine and high-magnesian melts and the nature of Hawaiian parental liquids. *Journal of Petrology* **52**, 1243-1263 (2011).

18 Kohn, S. C. & Schofield, P. F. The importance of melt composition in controlling trace-element behaviour: an experimental study of Mn and Zn partitioning between forsterite and silicate melts. *Chemical Geology* **117**, 73-87 (1994).

19 Banno, S. & Matsui, Y. On the formulation of partition coefficients for trace elements distribution between minerals and magma. *Chemical Geology* **11**, 1-15 (1973).

20 Roeder, P. L. & Emslie, R. F. Olivine-liquid equilibrium. *Contributions to Mineralogy and Petrology* **29**, 275-289 (1970).

21 O'Neill, H. S. C. & Berry, A. J. Activity coefficients at low dilution of CrO, NiO and CoO in melts in the system CaO-MgO-Al_2O_3-SiO_2 at 1400°C: Using the thermodynamic behaviour of transition metal oxides in silicate melts to probe their structure. *Chemical Geology* **231**, 77-89 (2006).

22 Baker, M. B. & Stolper, E. M. Determining the composition of high-pressure mantle melts using diamond aggregates. *Geochimica et Cosmochimica Acta* **58**, 2811-2827 (1994).

23 Baker, M. B., Hirschmann, M. M., Ghiorso, M. S. & Stolper, E. M. Compositions of near-solidus peridotite melts from experiments and thermodynamic calculations. *Nature* **375**, 308–311 (1995).

24 Hirschmann, M. M., Baker, M. B. & Stolper, E. M. The Effect of Alkalis on the Silica Content of Mantle-Derived Melts. *Geochimica et Cosmochimica Acta* **62**, 883-902 (1998).

25 Walter, M. J. Melting of garnet peridotite and the origin of komatiite and depleted lithosphere. *Journal of Petrology* **39**, 29-60 (1998).

26 McDonough, W. F. & Sun, S.-s. The composition of the Earth. *Chemical Geology* **120**, 223-253 (1995).

27 Presnall, D. C. *et al.* Liquidus phase relations on the join diopside-forsterite-anorthite from 1 atm to 20 kbar: Their bearing on the generation of crystallization of basaltic magma. *Contributions to Mineralogy and Petrology* **66**, 203-220 (1978).

28 Stolper, E. M. A phase diagram for mid-ocean ridge basalts: Preliminary results and implications for petrogenesis. *Contributions to Mineralogy and Petrology* **74**, 13-27 (1980).

29 Kelemen, P. B., Hirth, G., Shimizu, N., Spiegelman, M. & Dick, H. J. B. A review of melt migration processes in the adiabatically upwelling mantle beneath oceanic spreading ridges. *Philosophical Transactions of the Royal Society of London* **A355**, 283-318 (1997).

30 Plank, T., Spiegelman, M., Langmuir, C. H. & Forsyth, D. W. The meaning of "mean F": Clarifying the mean extent of melting at ocean ridges. *Journal of Geophysical Research* **100**, 15045-15052 (1995).

31 Asimow, P. D. & Longhi, J. The significance of multiple saturation points in the context of polybaric near-fractional melting. *Journal of Petrology* **45**, 2349-2367 (2004).

32 Wallace, P. J., Kamenetsky, V. S. & Cervantes, P. Melt inclusion CO_2 contents, pressures of olivine crystallization, and the problem of shrinkage bubbles. *American Mineralogist* **100**, 787-794 (2015).

33 Tuohy, R. M., Wallace, P. J., Loewen, M. W., Swanson, D. A. & Kent, A. J. R. Magma transport and olivine crystallization depths in Kīlauea's east rift zone inferred from experimentally rehomogenized melt inclusions. *Geochimica et Cosmochimica Acta* **185**, 232-250 (2016).

34 Beattie, P. Olivine-melt and ortho-pyroxene-melt equilibria. *Contributions to Mineralogy and Petrology* **115**, 103-111 (1993).

35 Vidito, C., Herzberg, C., Gazel, E., Geist, D. & Harpp, K. Lithological structure of the Galápagos Plume. *Geochemistry, Geophysics, Geosystems* **14**, 4214-4240 (2013).

36 Dasgupta, R., Jackson, M. G. & Lee, C.-T. A. Major element chemistry of ocean island basalts — Conditions of mantle melting and heterogeneity of mantle source. *Earth and Planetary Science Letters* **289**, 377-392 (2010).

37 Pietruszka, A. J., Norman, M. D., Garcia, M. O., Marske, J. P. & Burns, D. H. Chemical heterogeneity in the Hawaiian mantle plume from the alteration and dehydration of recycled oceanic crust. *Earth and Planetary Science Letters* **361**, 298-309 (2013).

38 Stracke, A. Earth's heterogeneous mantle: A product of convection-driven interaction between crust and mantle. *Chemical Geology* **330–331**, 274-299 (2012).

39 White, W. M. Isotopes, DUPAL, LLSVPs, and Anekantavada. *Chemical Geology* **419**, 10-28 (2015).

40 Stracke, A., Salters, V. J. M. & Sims, K. W. W. Assessing the presence of garnet-pyroxenite in the mantle sources of basalts through combined hafnium-neodymium-thorium isotope systematics. *Geochemistry, Geophysics, Geosystems* **1**, 1006 (1999).

41 Elkins, L. J., Gaetani, G. A. & Sims, K. W. W. Partitioning of U and Th during garnet pyroxenite partial melting: Constraints on the source of alkaline ocean island basalts. *Earth and Planetary Science Letters* **265**, 270–286 (2008).

42 Jackson, M. G., Weis, D. & Huang, S. Major element variations in Hawaiian shield lavas: Source features and perspectives from global ocean island basalt (OIB) systematics. *Geochemistry, Geophysics, Geosystems* **13**, Q09009 (2012).

43 Herzberg, C. *et al.* Phantom Archean crust in Mangaia hotspot lavas and the meaning of heterogeneous mantle. *Earth and Planetary Science Letters* **396**, 97-106 (2014).

Acknowledgements:

C. Ma and Steven Creighton are thanked for their guidance and support using the electron microprobe, and for sharing xenolith data, respectively. Funding was provided by National Science Foundation grant EAR-1019886, National Aeronautics and Space Administration grant NNG04GG14G, and European Research Council grant 267764.

Author Contributions:

A.K.M. analyzed the experiments, constructed the geochemical models and wrote the manuscript. B.J.W., M.B.B., and E.M.S. provided intellectual guidance throughout the project and wrote the manuscript.

Author Information:

Reprints and permission information is available at www.nature.com/reprints. The authors declare no competing financial interests. Readers are welcome to comment on the online version of the paper. Correspondence and requests for materials should be addressed to A.K.M. (andrew.matzen@earth.ox.ac.uk)

Competing interest Declaration: None

Supplemental Information for this manuscript is available online at nature.com/ngeo

Figure Captions:

Figure 1.

Covariation of NiO_{89} and MnO_{89} in a global array of olivines. Motivated by ref. 6, after correction to an Mg# of 0.89 (see methods), there is a good correlation between NiO_{89} and

MnO_{89} concentrations (in wt. %) in primitive olivine phenocrysts in basalts[6,35] (Spearman rank-order correlation coefficient of –0.79, $p < 0.001$). Lithospheric thickness appears to play a role; Ni increases and Mn decreases moving from olivines from MORBs (orange fill) to those erupted on thin (<70 km, cyan fill) and thick (>70 km, magenta fill) lithosphere. NATP, North-Atlantic Tertiary Province; FB, flood basalts; OIBs, other ocean-island basalts (including seamounts); Haw-Emp, Hawaiian-Emperor seamount chain. Dotted lines connect samples from localities where olivines with Mg#s of ~0.89 have MnO and NiO concentrations that differ substantially from the calculated values, see methods.

Figure 2.

Olivine-liquid manganese partition coefficients ($D_{Mn}^{ol/liq}$), by weight. Triangles denote 1-atm experiments on a synthetic Hawaiian picrite[17]; circles denote those experiments where temperature and pressure were varied in concert in an attempt to keep the liquid composition constant[15,16]. Symbol fill corresponds to the MgO concentration of the experimentally-produced glass, in wt. % (MgO^{liq}). $D_{Mn}^{ol/liq}$ values appear to be insensitive to temperature and pressure; they do correlate with the MgO content of the coexisting silicate liquid, decreasing from ~0.9 to ~0.5 as MgO^{liq} increases from 12 to 24 wt. %.

Figure 3.

Model MnO (a) and NiO (b) contents (in wt. %) of olivines during partial melting of peridotite. Olivine MnO and NiO concentrations were calculated using the phase fractions, major-element compositions, and temperatures from peridotite partial melting experiments[22-25], along with partitioning expressions in the text and methods. In (a), dotted lines connect subsolidus

experiments to the lowest melt fraction experiment run at the same pressure. Dashed lines are approximate melt fraction contours (in wt. %). Solid lines are least-squares fits to each isobaric supersolidus dataset. MnO contents of residual olivines depend strongly on both the pressure and extent of melting (see text).

Figure 4.

Comparison of model peridotite melting results to natural olivine phenocryst NiO_{89} and MnO_{89} values. The plotted olivine NiO and MnO contents from the high-pressure experiments have been corrected to a Mg# of 0.89 using two steps: calculating 1-atm liquidus olivine compositions for the high-pressure melts; then projecting these liquidus olivine compositions to a Mg# of 0.89 (see text and methods); symbols and sources of data for natural olivines as in Fig 1. Predicted olivine compositions from 1.0, 3.0, and 4.0–4.5 GPa are shown in green, orange, and purple, respectively. The overlap between our modeling results and the natural olivine phenocrysts suggest that the covariation between NiO_{89} and MnO_{89} can be largely explained by varying degrees of batch melting of peridotite at different pressures.

Figure 5.

NiO_{89}/MnO_{89} as a function of depth to the lithosphere-asthenosphere boundary (LAB). Only samples where the LAB at the time of eruption is well-constrained[15,36] are shown, see methods and Supplementary Table S1 (light grey symbols; olivine compositions from Fig. 1). NiO_{89}/MnO_{89} agrees well with the depth corresponding to the pressure of our partial melting calculations. This suggests that (1) the NiO_{89}/MnO_{89} ratio can be used as a broad indicator of the depth of peridotite melting, and (2) for the majority of natural samples in the dataset, the Ni and

Mn contents are well-explained by equilibration of melts with peridotite at pressures corresponding to the lithosphere-asthenosphere boundary.

Methods:

MnO_{89} and NiO_{89}

Direct comparison of natural olivine phenocrysts to each other and to our model results requires consideration of the effects of fractionation on their MnO and NiO contents. In order to do this objectively we performed, for each location, an iterative, bisquare-weighted fit of high-precision natural olivine data for NiO and MnO[6,35] as a function of Mg# (all fits are shown in the Supplementary Information, Figures S6–S63). This yields MnO and NiO at a Mg# of 0.89 for each location. We chose Mg# of 0.89 because many locations report olivines at, or very near to, this Mg#, thereby minimizing any error due to extrapolation (we excluded those locations where the maximum Mg# was less than 0.885). Corrected values for NiO and MnO at an Mg# of 0.89 (NiO_{89} and MnO_{89}, respectively) are reported in Table S1 and are shown in Figure 1. Note that some samples from the Galápagos report multiple analyses on a single olivine phenocryst. For these samples, we performed our fits using only the analysis from each phenocryst with the highest Mg#. For the Galápagos samples we also excluded analyses that did not report both the Ni and Mn contents of an olivine. In some locations, analyses from different samples display distinct NiO or MnO contents, relative to the other samples from the same location. In these cases, samples were divided and fit independently; it is for this reason that we report multiple NiO_{89} and MnO_{89} values for some locations (e.g., Mid-Atlantic Ridge samples from 43°N). During the fitting process our default position was to group samples from a given location

together; to be fit separately, a sample (or group of samples) needed to have, at a range of Mg#s, NiO or MnO contents that were not only higher or lower than the majority of other analyses from the same location, but also values that fell consistently outside of the distribution of NiO or MnO contents generated by the other samples from the same location.

For each location the NiO and MnO data were fit using either a linear [$y = a(x) + b$] or a power-law [$y = a(x^b) + c$] function. Linear fits were used if 1) the exponent in the power-law fit was, within uncertainty (1σ), unity, 2) if the calculated NiO_{89} or MnO_{89} for the linear and power-law fits overlapped at 1σ, and 3) if the minimum Mg# olivine for the location was >0.89. For NiO, linear fits were also used if the curvature of the power-law fit was concave down. Several exceptions were made for the MnO vs. Mg# fits: for Kilauea Iki; Koolau, Makapuu; Koolau, KSDP; Reykjanes, Sulur/Stapafell; Snaefellsness, Sydri–/Ytri–Raudamelur; 9° N Mid-Atlantic Ridge; Bouvet; and Galápagos, San Cristobal-1, linear fits were used as these fits did a superior job of describing the high-Mg# olivines for these samples. The results of our fits are listed in Table S1 and shown in the Supplementary Figures.

There are seven suites that are problematic and/or merit further discussion. Galápagos, San Cristobal–2: this sample set contains only nine analyses and although the five most magnesian span a range of Mg#s from 0.878 to 0.911, the NiO contents of these five olivines *increase* with decreasing Mg#. It is clear that these olivine compositions are not related via simple fractionation and although the fits are included in the Supplemental Information, this locality is not included in any further analysis or on any figures. The problems associated with the remaining six suites fall into three general categories: (1) the total number of olivine analyses is small and the data show appreciable scatter in NiO^{ol} and MnO^{ol} vs. olivine Mg# space (La Gomera; irrespective of the scatter, we calculated NiO_{89} and MnO_{89} values based on the best-fit

regression lines). (2) All the olivine Mg#s plot above the target value of 0.89 requiring an extrapolation down to NiO_{89} and MnO_{89} values (Siqueros Fracture Zone and 43°N Mid-Atlantic Ridge-1). However, olivine NiO and MnO contents in both of these suites are well characterized by the regression lines (see Supplementary Figures) and the extrapolations are relatively minor (0.006 and 0.004 Mg# units, respectively). (3) The bulk of the analyses in the final three suites (Koolau, KSDP; Kauai, Haena; and Reykjanes, Haleyjabunga) are well described by best-fit lines, but each suite contains a small number of olivine analyses with NiO and (in two of the suites) MnO values that are visibly offset from the majority of the data (see Supplementary Figures). In each suite, one of these "offset" compositions has an Mg# that is very close to 0.89 and in Figs. 1 and 4, we show both the calculated NiO_{89} and MnO_{89} values (based on regressions of all of the data in each sample set) and the "offset" compositions closest to 0.89 (pairs of NiO and MnO values are connected by a dotted line; the Mg#s for the three plotted "offset" olivines are: 0.891, Koolau, KSDP; 0.889, Kauai, Haena; and 0.890, Reykjanes, Haleyjabunga and both sets of NiO and MnO values are reported in the Supplementary Information). Although NiO and MnO values for these six "problematic" suites of samples are shown in the figures, their data is not given any interpretational weight; i.e., the NiO_{89}-MnO_{89} slope quoted in the main text considers only the other 51 locations listed in the Supplementary Table.

As described in the main text, we use the median slopes of the NiO and MnO vs. Mg# fits to correct the olivine NiO and MnO values from our peridotite melting calculations to an Mg# of 0.89. When a power-law expression was fit to the data, if the maximum Mg# from the location was less than 0.89 we determined the slope for that location by taking the derivative of the fit at an Mg# of 0.89; if the maximum Mg# from the location was greater than 0.89 we took the slope at the midpoint between the maximum Mg# of the sample set and 0.89. Note that the reported

slopes for Galápagos, Floreana are simply the first derivative of the fits at an Mg# of 0.89 due to the dearth of olivines with Mg#s between ~0.908 (the highest Mg# for this location) and 0.89.

Errors reported for MnO_{89} and NiO_{89} reflect solely the uncertainty associated with the fits, and are only shown on Figs. 1 and 4 when significantly larger than the symbol size.

Depths to the lithosphere-asthenosphere boundary (LAB) at the time of eruption were largely taken from ref. 36 (see also ref. 15).

Analytical Methods

Glass and olivine compositions were measured on Caltech's JEOL JXA-8200 electron microprobe. Mn in glasses was analyzed using a 200-nA beam, a 20-μm spot, and ~90 sec on peak counting times (in all cases, high and low background positions were measured for half of the on-peak counting time). Glass major-element compositions were determined in a separate analytical session (using a 10-nA beam and a 10-μm spot), and the high-current analyses were processed[44] using the major- and minor-element concentrations from the low-beam-current analyses. Olivine compositions were measured using a 1-μm spot, a 100-nA beam current and an accelerating voltage of 15 kV; the on-peak counting time for Mn in olivines was 60 s. Glass[45] and olivine (San Carlos and Guadeloupe) secondary standards were repeatedly analyzed during each analytical session to monitor and correct for inter- and intra-session drift.

Partitioning expressions

Using modal abundances and major-element phase compositions from high-pressure experiments, we calculated the abundances of Mn in all phases using olivine-liquid and olivine-mineral partitioning expressions obtained by fitting experimental and xenolith-derived

partitioning data to either temperature-based or composition-based functional forms. For Mn partitioning, most of the previously-published experiments were obtained from two sources, (a) the olivine-liquid compilations used by Matzen et al.[16,17], and (b) the library of experimental phase relations, LEPR[46]. LEPR was interrogated for experiments whose starting material contained at a minimum, Si, Al, Fe, Mn, Mg, and Ca and the phases of interest. Note that we also included experimental data from Davis et al.[47] in our initial datasets. In an attempt to include only high-quality data, a series of filters were applied to the reported analyses: under oxidizing conditions a fraction of Mn in a silicate liquid may be trivalent[48]; thus, we included only those experiments conducted under reducing conditions (reported fO_2s < 2 log units above the QFM buffer, or where the sample was run in a graphite, Fe, or Mo capsule). Olivines were only accepted if they had 3 ± 0.15 cations and 1 ± 0.15 Si per formula unit, respectively. Orthopyroxene and clinopyroxene analyses were included only if they had 4 ± 0.15 cations per formula unit. Garnet analyses with fewer than 7.9 total cations and 2.95 silicon per formula unit were excluded. Lastly, in an attempt to fit only those experiments where Mn was measured with relatively high precision, we filtered experiments by the fractional error (1 σ/value) of their partition coefficients. We excluded olivine-liquid partitioning measurements where the fractional error was >0.066, the average plus two standard deviations of the fractional errors associated with the $D_{Mn}^{ol/liq}$ values reported here. For olivine-mineral partition coefficients we were less restrictive, excluding those experiments with fractional errors greater than 0.15, (a value that is approximately two times the largest fractional error for the olivine-liquid measurements reported here); experiments from the LEPR database that did not report errors on the phase compositions were not included in the fit. These criteria excluded a large number of experiments, resulting in ol-liq, ol-opx, ol-cpx, and ol-gt datasets with 68, 20, 44, and 11 experiments, respectively. Due to

the relatively small number of experiments in the ol-opx, ol-cpx, and ol-gt datasets, we also included Mn partitioning data from xenoliths. To the experimental ol-opx and ol-cpx dataset, we added data from 24 well-equilibrated spinel peridotite xenoliths where Mn was measured with high precision[49], and to the ol-gt data we added 30 garnet peridotite xenoliths that appear to be well-equilibrated[50]. For the garnet-bearing xenoliths, we used agreement between five different thermometers[51-54] as evidence of equilibration, selecting only those xenoliths where the standard deviation between thermometers was <30° (using the Al in orthopyroxene barometer[52] to calculate pressure). For the selected garnet-bearing xenoliths, temperature was calculated by taking the median of the two-pyroxene[52], the olivine-garnet[51], and the garnet-clinopyroxene[54] thermometers.

Major- and minor-element partitioning between olivine and liquid is often described using an exchange reaction that involves Mg e.g., ref. 18,20,55,56-58. The Mn-Mg, the exchange reaction is:

$$MgSi_{0.5}O_2^{ol} + MnO^{liq} \leftrightarrow MnSi_{0.5}O_2^{ol} + MgO^{liq}, \quad (3)$$

for which we can write an expression for the free energy of the reaction as:

$$\Delta_{r(3)}G^{\circ}_{T,P} = -RT\ln\left(\frac{X^{ol}_{MnSi_{0.5}O_2} X^{liq}_{MgO}}{X^{ol}_{MgSi_{0.5}O_2} X^{liq}_{MnO}} \times \frac{\gamma^{ol}_{MnSi_{0.5}O_2} \gamma^{liq}_{MgO}}{\gamma^{ol}_{MgSi_{0.5}O_2} \gamma^{liq}_{MnO}}\right), \quad (4)$$

where $\Delta_{r(3)}G^{\circ}_{T,P}$ is the standard-state Gibbs free energy of reaction (3) at temperature (T) and pressure (P), X_i^{φ} and γ_i^{φ} are the mole fraction and activity coefficient of the i^{th} component in phase φ, and R is the gas constant. In detail, $\Delta_{r(3)}G^{\circ}_{T,P}$ depends on the standard state enthalpies and entropies, the isobaric change in heat capacity $\left(\Delta_{r(3)}C^{\circ}_{p}\right)$ at P_{ref}, and the temperature and pressure dependent volume change $\left(\Delta_{r(3)}V\right)$ of reaction (3). Assuming that: (a) over moderate

ranges in temperature and pressure $\Delta_{r(3)}C_p^\circ$ and $\Delta_{r(3)}V$ are small enough to be safely neglected[16,59]; (b) at high temperatures, olivines can be treated as ideal solutions e.g., ref. 60,61; and (c) the ratio of activity coefficients for divalent cations in silicate liquids is approximately one, equation (4) simplifies to:

$$-\frac{\Delta_{r(3)}H^\circ_{T_{ref},P_{ref}}}{RT}+\frac{\Delta_{r(3)}S^\circ_{T_{ref},P_{ref}}}{R}=\ln\left(D_{Mn}^{molar}\right)+\ln\left(\frac{X_{MgO}^{liq}}{X_{MgSi_{0.5}O_2}^{ol}}\right)=\ln\left(K_{D,Mn-Mg}^{ol/liq}\right), \quad (5)$$

where $D_{Mn}^{molar}=\frac{X_{MnSi_{0.5}O_2}^{ol}}{X_{MnO}^{liq}}$. Note that although the ratio of activity coefficients for divalent cations in silicate melts is unlikely to be equal to one, there is evidence to suggest that it can be taken as approximately constant (e.g., ref. 21), in which case, the $\Delta_{r(3)}S^\circ_{T_{ref},P_{ref}}$ term will also contain the liquid activity coefficient term. If the assumptions listed above are valid, $lnK_{D,Mn-Mg}^{ol/liq}$ should be independent of composition and there should be a linear relationship between $lnK_{D,Mn-Mg}^{ol/liq}$ and inverse temperature. As shown in Supplemental Information Fig. S2, however, there is a clear dependence of $lnK_{D,Mn-Mg}^{ol/liq}$ on liquid composition with the highest MgO^{liq} series having the highest $lnK_{D,Mn-Mg}^{ol/liq}$ values. Furthermore, most of the fits to $lnK_{D,Mn-Mg}^{ol/liq}$ and inverse temperature for the individual constant composition series do not overlap at one sigma with the fit to the dataset as a whole (slopes for the 12, 15, 18, and 21 MgO^{liq} series, and the dataset as a whole are 418 ± 1488, 762 ± 918, 480 ± 594, 1235 ± 1545, and −745 ± 260 (K) respectively. This result supports earlier inferences[18,57] that either the temperature dependence of $K_{D,Mn-Mg}^{ol/liq}$ is small and/or that the ratio of the activities of MgO and MnO in the liquid is not constant. Because each constant-compositional series has a temperature dependence that is zero, within error (Supplemental Information Fig. S2), and because MgO^{liq} has the highest linear correlation

coefficient with the residuals in a fit of $lnK_{D,Mn-Mg}^{ol/liq}$ vs. inverse temperature (Supplemental Information Fig. S1a), we parameterized the exchange coefficient as a function of the MgO content of the liquid [equation (1)]. Equation (1) successfully predicts (within one standard deviation of their measured values) 86 % of our new measurements of $D_{Mn}^{ol/liq}$. For the experiments reported here and the low-error experiments from the literature, comparing calculated and measured $D_{Mn}^{ol/liq}$values results in a median percent error of 3.22, where percent error is defined as $100\left|D_{Mn,calc}^{ol/liq} - D_{Mn,meas}^{ol/liq}\right| / D_{Mn,meas}^{ol/liq}$. Fitting the same partitioning data against $D_{Mg}^{ol/liq}$ [34,62,63] results in median errors that are only slightly higher, 3.37 or 3.86 % depending on whether the fitting is done in wt. % or cation fraction, respectively.

Olivine-orthopyroxene and olivine-garnet partitioning were parameterized using the exchange reaction approach[55,56,64]. This results in the following ol-opx and ol-gt models:

$$K_{D,Mn-Mg}^{ol/opx} = \exp(-328 \pm 106/\mathrm{T(K)} - 0.099 \pm 0.075) \quad (6)$$

$$K_{D,Mn-Mg}^{ol/gt} = \exp(-4171 \pm 302\ /\mathrm{T(K)} + 1.11 \pm 0.22), \quad (7)$$

Supplemental Information Figs. S3 and S4 show the data as well as the resulting fits. Note that on these figures we also show the peridotite melting experiments that form the basis of our melting calculations[22-25]. Although these studies did not measure Mn to high precision, our fits, based on high-precision analyses of selected experiments and well-equilibrated xenoliths, are consistent with their findings.

Large cations such as Ca, Mn and the REE partition into the large M2 site in clinopyroxene in ways which are readily systematized using the lattice-strain model[65,66]. The ideal cation radius

(r_o) is observed to increase with increasing Ca content of the M2 site and the energy "penalty" for replacing Ca by Mn depends on the Young's Modulus (E) of the site which is similar to that of clinopyroxene itself [65]. In our model, r_o was varied linearly between that of pure Ca and Mg in the M2 site (using ionic radii from ref. 67), and E was assumed to be two thirds of the value for rare-earth elements[66]. In practice, the functional form of the lattice strain model for clinopyroxene is well described by a 4th order polynomial based on the CaO content (in wt. %) of the coexisting cpx. The strain-based model was fit to the data by varying only the constant term, equivalent to varying D_0. The resulting expression is:

$$D_{Mn}^{ol/cpx} = 2.1101\text{x}10^{-5}(\text{CaO}^{\text{cpx}})^4 - 7.5872\text{x}10^{-4}(\text{CaO}^{\text{cpx}})^3 + 1.3204\text{x}10^{-2}(\text{CaO}^{\text{cpx}})^2 - 0.\ 10348\ (\text{CaO}^{\text{cpx}}) + 1.2147 \pm 0.0213. \quad (8)$$

To estimate the uncertainty associated with the constant term in equation (8), we used the bootstrap method and the reported errors on $D_{Mn}^{ol/cpx}$ and CaO^{cpx} from the LEPR database. Errors on the MnO and CaO contents of the xenolith samples were not reported, thus we assumed that errors (1σ) on the MnO contents of olivine and clinopyroxene in the xenoliths were 4 % (the upper limit of the external precision estimate)[49], and that the errors on the CaO content of the clinopyroxenes were 0.87 wt. %, a value that is two times the median of the errors on CaO^{cpx} from the experiments fit from the LEPR database. Fits and data are shown in Supplemental Information Fig. S5.

To parameterize Mn-Mg exchange between olivine and spinel, we performed a least-squares fit to well-equilibrated spinel-lherzolite xenoliths[49] using the functional form of ref. 68 (applied to ol-sp Ni-Mg partitioning) that incorporates the effect of spinel composition as well as temperature on the K_D. The resulting equation is:

$$K_{D,Mn-Mg}^{ol/sp} = \exp[-2292.2 \pm 110.8(Cr\#_{wt}^{sp})/\mathrm{T(K)} - 0.161 \pm 0.027], \quad (9)$$

where $Cr\#_{wt}^{sp}$ is defined as $Cr_2O_3/(Cr_2O_3 + Al_2O_3 + Fe_2O_3)$ in the spinel, by weight. Finally, the fertile peridotite MnO content was assumed to be 0.131 wt. % [26,69].

To model Ni contents we used the olivine-liquid partitioning expression from [15]. Olivine-orthopyroxene, olivine-clinopyroxene, and olivine-spinel partitioning was modeled using the expressions presented by ref. 68:

$$K_{D,Ni-Mg}^{ol/opx} = \exp(1419/\mathrm{T(K)} - 0.241), \quad (10)$$

$$K_{D,Ni-Mg}^{ol/cpx} = \exp(1773/\mathrm{T(K)} - 0.422), \text{ and} \quad (11)$$

$$K_{D,Ni-Mg}^{ol/sp} = \exp[1{,}722(Cr\#_{mol}^{sp})/\mathrm{T(K)} - 1.118] \quad (12)$$

where $Cr\#_{mol}^{sp}$ is the molar $Cr_2O_3/(Cr_2O_3 + Al_2O_3 + Fe_2O_3)$ in the spinel.

Olivine-garnet partitioning was calculated according to [70]

$$K_{D,Ni-Mg}^{ol/gt} = \exp(5264 \pm 589/\mathrm{T(K)} - 2.065 \pm 0.405). \quad (13)$$

The fertile peridotite NiO content was assumed to be 0.25 wt. %[26], identical (within 7 ppm) to the value used by ref. 7.

To calculate errors on the MnO content of olivines in our peridotite-melting model, we used the bootstrap method, incorporating the reported errors on the major-element compositions of the peridotite melting experiments (as changing phase compositions affect the calculated phase fractions and thus our calculated MnO^{oliv}) and the errors on the Mn partitioning expressions

presented above. We used an unweighted mass balance calculation and assumed that all errors were normally distributed. The errors shown in Fig. 3 are one standard deviation of 10,000 iterations of our error-propagation calculation. Errors were not calculated for NiO since uncertainties on the coefficients in equations (10), (11), and (12) were not reported[68].

Data availability

The authors declare that the data supporting the findings of this study are available within the article and its supplementary information files. In addition to the high-precision measurements reported in Table, 1, data from other authors used in this study are referenced in the main text, the methods section, and in the Supplemental Information.

Code availability

A spreadsheet that contains our forward model of batch peridotite melting is included in the Supplemental Information.

References: (Methods Only)

44 Armstrong, J. T. in *Microbeam Analysis* (ed D.E. Newbury) 239–246 (San Francisco Press, San Francisco, 1988).

45 Jochum, K. P. *et al.* MPI-DING reference glasses for in situ microanalysis: New reference values for element concentrations and isotopic ratios. *Geochemistry, Geophysics, Geosystems* **7**, Q02008 (2006).

46 Hirschmann, M. M. *et al.* Library of Experimental Phase Relations (LEPR): A database and Web portal for experimental magmatic phase equilibria data. *Geochemistry, Geophysics, Geosystems* **9**, Q03011 (2008).

47 Davis, F. A., Humayun, M., Hirschmann, M. M. & Cooper, R. S. Experimentally determined mineral/melt partitioning of first-row transition elements (FRTE) during partial melting of peridotite at 3 GPa. *Geochimica et Cosmochimica Acta* **104**, 232-260 (2013).

48 Schreiber, H. D. *et al.* An Electromotive Force Series in a Borosilicate Glass-Forming Melt. *Journal of the American Ceramic Society* **67**, C-106-C-108 (1984).

49 Witt-Eickschen, G., Palme, H., O'Neill, H. S. C. & Allen, C. M. The geochemistry of the volatile trace elements As, Cd, Ga, In and Sn in the Earth's mantle: New evidence from in situ analyses of mantle xenoliths. *Geochimica et Cosmochimica Acta* **73**, 1755-1778 (2009).

50 Creighton, S. A semi-empirical manganese-in-garnet single crystal thermometer. *Lithos* **112S**, 177-182 (2009).

51 O'Neill, H. S. C. & Wood, B. J. An experimental study of Fe-Mg partitioning between garnet and olivine and its calibration as a geothermometer. *Contributions to Mineralogy and Petrology* **70**, 59-70 (1979).

52 Brey, G. P. & Köhler, T. Geothermobarometry in four-phase lherzolites II. New thermobarometers, and practical assessment of existing thermobarometers. *Journal of Petrology* **31**, 1353-1378 (1990).

53 Harley, S. L. An experimental study of the partitioning of Fe and Mg between garnet and orthopyroxene. *Contributions to Mineralogy and Petrology* **86**, 359-373 (1984).

54 Krogh, E. J. The garnet-clinopyroxene Fe-Mg geothermometer — a reinterpretation of existing experimental data. *Contributions to Mineralogy and Petrology* **99**, 44-48 (1988).

55 Hart, S. R. & Davis, K. E. Nickel partitioning between olivine and silicate melt. *Earth and Planetary Science Letters* **40**, 203-219 (1978).

56 Kinzler, R. J., Grove, T. L. & Recca, S. I. An experimental study on the effect of temperature and melt composition on the partitioning of nickel between olivine and silicate melt. *Geochimica et Cosmochimica Acta* **54**, 1255-1265 (1990).

57 Watson, E. B. Partitioning of manganese between forsterite and silicate liquid. *Geochimica et Cosmochimica Acta* **41**, 1363-1374 (1977).

58 Le Roux, V., Dasgupta, R. & Lee, C-T. A. Mineralogical heterogeneities in the Earth's mantle: Constraints from Mn, Co, Ni and Zn partitioning during partial melting. *Earth and Planetary Science Letters* **307**, 395-408 (2011).

59 Wood, B. J. & Fraser, D. G. *Elementary Thermodynamics for Geologists*. (Oxford University Press, Oxford, 1976).

60 Nafziger, R. H. & Muan, A. Equilibrium phase compositions and thermodynamic properties of olivines and pyroxenes in the system MgO-"FeO"-SiO_2. *American Mineralogist* **52**, 1364-1385 (1967).

61 Campbell, F. E. & Roeder, P. The stability of olivine and pyroxene in the Ni-Mg-Si-O system. *American Mineralogist* **53**, 257-268 (1968).

62 Beattie, P., Ford, C. & Russell, D. Partition coefficients for olivine-melt and orthopyroxene-melt systems. *Contributions to Mineralogy and Petrology* **109**, 212-224 (1991).

63 Jones, J. H. Temperature- and pressure-independent correlations of olivine/liquid partition coefficients and their application to trace-element partitioning. *Contributions to Mineralogy and Petrology* **88**, 126-132 (1984).

64 Leeman, W. P. & Lindstrom, D. J. Partitioning of Ni^{2+} between basaltic and synthetic melts and olivines—an experimental study. *Geochimica et Cosmochimica Acta* **42**, 801-816 (1978).

65 Blundy, J. & Wood, B. Prediction of crystal-melt partition coefficients from elastic moduli. *Nature* **372**, 452-454 (1994).

66 Wood, B. J. & Blundy, J. D. A predictive model for rare earth element partitioning between clinopyroxene and anhydrous silicate melt. *Contributions to Mineralogy and Petrology* **129**, 166-181 (1997).

67 Shannon, R. D. Revised effective ionic radii and systematic studies of interatomic distances in halides and chalcogenides. *Acta Crystallographica Section A* **32**, 751-767 (1976).

68 Witt-Eickschen, G. & O'Neill, H. S. C. The effect of temperature on the equilibrium distribution of trace elements between clinopyroxene, orthopyroxene, olivine and spinel in upper mantle peridotite. *Chemical Geology* **221**, 65-101 (2005).

69 Workman, R. K. & Hart, S. R. Major and trace element composition of the depleted MORB mantle (DMM). *Earth and Planetary Science Letters* **231**, 53-72 (2005).

70 Yaxley, G. M. & O'Neill, H. S. C. Ni in Garnet Thermometry – A New Experimental Calibration at 3.0 – 4.5 GPa of Ni-Mg Exchange between Garnet and Olivine at Upper Mantle Pressures. *9th International Kimberlite Conference Extended Abstract*, 9IKC-A-00200 (2008).

Table 1. Run Conditions and Phase Compositions

Run	T(°C)	P(kbar)	n^{liq}	MgO^{liq}	MnO^{liq}	n^{ol}	MgO^{ol}	$Mg\#^{ol}$	MnO^{ol}	$D_{Mn}^{ol/liq}$
Matzen et al. 2011										
26	1500	0.001	10	23.9	0.162(6)	10	50.7	92.4	0.088(6)	0.54(4)
24	1451	0.001	10	20.8	0.166(4)	10	49.9	91.2	0.102(4)	0.62(3)
21	1452	0.001	7	21.0	0.166(4)	10	49.9	91.5	0.101(6)	0.61(4)
17	1401	0.001	10	18.1	0.168(3)	9	49.0	90.0	0.115(6)	0.68(4)
27	1398	0.001	10	18.4	0.169(4)	10	48.7	90.0	0.111(4)	0.65(3)
28	1350	0.001	9	15.9	0.172(5)	10	47.5	89.0	0.121(5)	0.70(3)
15	1349	0.001	10	15.4	0.169(3)	10	47.8	88.6	0.132(5)	0.78(3)
6	1302	0.001	10	13.2	0.167(4)	8	47.0	87.7	0.148(8)	0.89(5)
46	1300	0.001	9	14.0	0.171(3)	10	47.1	87.8	0.140(5)	0.82(3)
Matzen et al. 2013										
6	1450	10	9	17.7	0.193(2)	10	48.6	89.7	0.142(5)	0.73(3)
7	1450	10	10	17.4	0.191(1)	9	48.5	89.8	0.138(8)	0.72(4)
8	1450	10	9	17.4	0.192(2)	10	48.1	89.6	0.140(6)	0.73(3)
9	1500	20	8	18.9	0.196(6)	10	49.0	90.2	0.133(5)	0.68(3)
10	1500	20	9	18.4	0.197(2)	8	48.7	90.0	*0.136(4)*	0.69(2)
13	1525	25	10	17.2	0.195(4)	7	47.9	89.7	0.141(5)	0.72(3)
17R	1450	10	8	17.8	0.191(4)	6	48.5	90.1	0.140(6)	0.73(3)
25	1400	0.001	11	18.1	0.198(3)	7	48.8	90.3	*0.140(3)*	0.71(2)
28R	1500	20	8	17.2	0.191(1)	11	48.2	89.8	*0.143(4)*	0.75(2)
30	1550	30	12	18.3	0.205(8)	7	48.4	89.7	*0.140(5)*	0.68(4)
32R	1400	0.001	8	17.1	0.203(2)	8	47.1	89.7	*0.147(3)*	0.72(2)
33R	1550	30	9	16.3	0.207(3)	9	46.7	88.1	*0.147(5)*	0.71(2)
45R	1450	10	11	17.4	0.191(3)	11	48.3	89.7	0.139(7)	0.73(4)
Matzen et al. 2017										
49	1430	15	10	15.2	0.184(3)	10	47.7	88.5	*0.154(4)*	0.83(3)
50	1450	20	9	14.6	0.191(2)	10	47.0	87.7	*0.158(6)*	0.83(3)
51	1400	10	10	15.1	0.181(3)	10	48.2	88.8	*0.149(7)*	0.82(4)
52	1375	15	10	12.0	0.183(2)	6	46.6	86.7	*0.174(6)*	0.95(3)
53	1350	10	9	12.2	0.173(3)	10	47.2	87.6	*0.166(5)*	0.96(3)
56	1475	25	10	14.7	0.197(3)	7	47.0	87.2	*0.154(6)*	0.78(3)
58	1550	20	5	21.3	0.206(3)	10	49.3	90.1	*0.131(6)*	0.63(3)
59	1575	25	10	21.1	0.208(8)	10	49.5	90.2	*0.132(5)*	0.63(4)
62R	1400	20	7	11.8	0.183(2)	8	44.7	85.7	*0.168(5)*	0.92(3)
63R	1475	25	10	14.1	0.197(3)	7	45.7	86.5	*0.157(6)*	0.79(4)
64R	1600	30	10	20.4	0.206(3)	10	48.9	90.0	*0.133(4)*	0.65(2)
65	1348	0.001	10	15.9	0.195(2)	10	48.5	88.9	*0.153(7)*	0.78(3)
67R	1348	0.001	10	15.4	0.196(3)	9	46.8	88.5	*0.155(5)*	0.79(3)
68	1300	0.001	10	13.2	0.196(4)	10	47.3	87.5	*0.171(7)*	0.87(4)
70	1451	0.001	10	21.9	0.189(3)	4	49.9	91.1	*0.123(8)*	0.65(4)

Selected run conditions and olvine (ol) and liquid (liq) compositions. Note: We do not report values for run 39 from Matzen et al. 2011 (ref. 17) as under oxidizing conditions Mn^{3+} may be present in the silicate liquid[48]. Numbers in parentheses are analytical uncertainties in terms of the least units cited, e.g., 0.162(6) corresponds to 0.162±0.006 where 0.162 represents the average of n analyses, and 0.006 is one standard deviation of those analyses. Italicized olivine

analyses have been previously published. $D_{Mn}^{ol/liq}$, by weight, number enclosed in parentheses represents propagated analytical uncertainty (one sample standard deviation) of MnO in the olivine and glass.

Figure 1

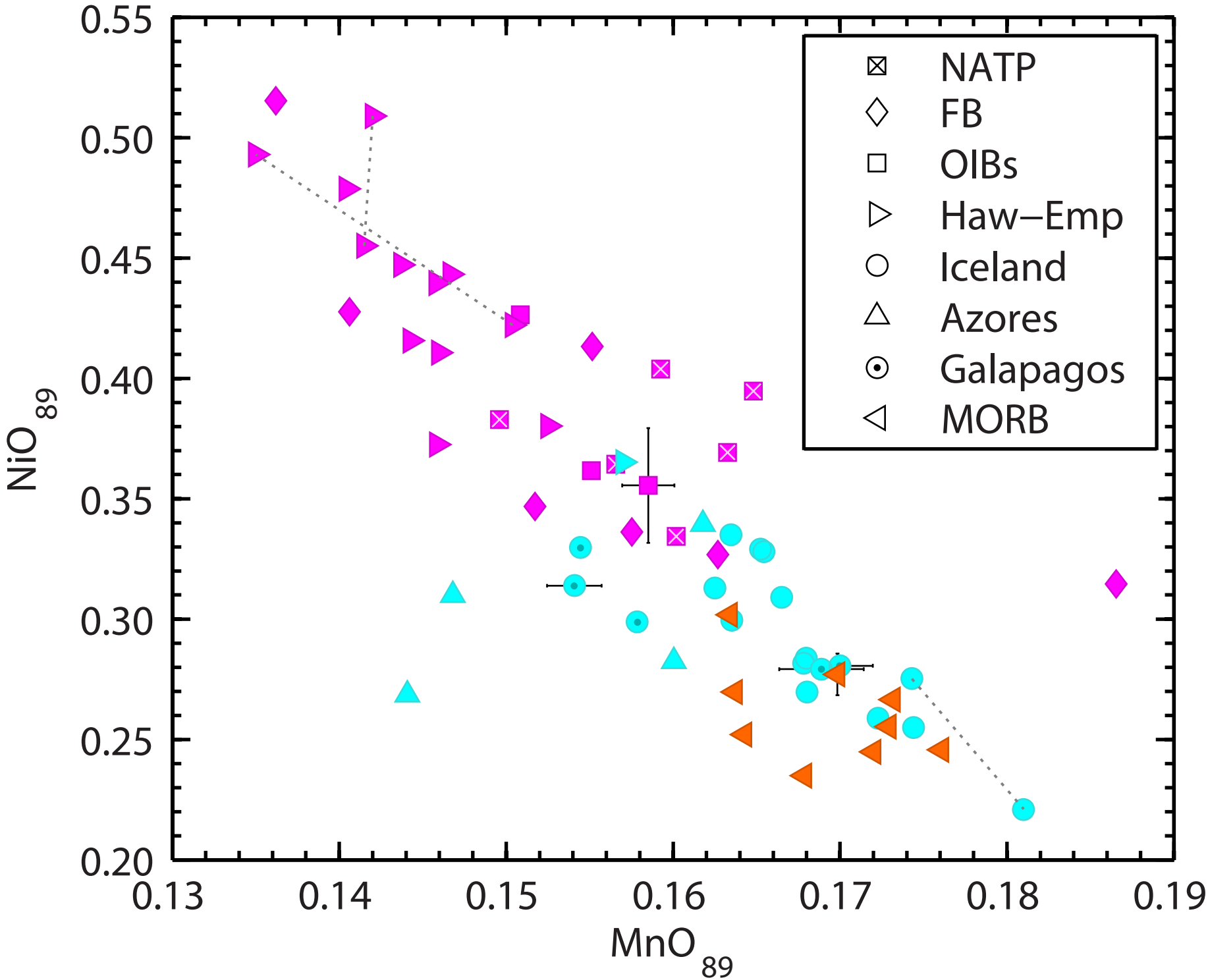
0.55
0.50
0.45
0.40
0.35
0.30
0.25
0.20
NiO89
0.13
0.14
0.15
0.16
0.17
0.18
0.19
MnO89
NATP
FB
OIBs
Haw–Emp
Iceland
Azores
Galapagos
MORB

Figure 2

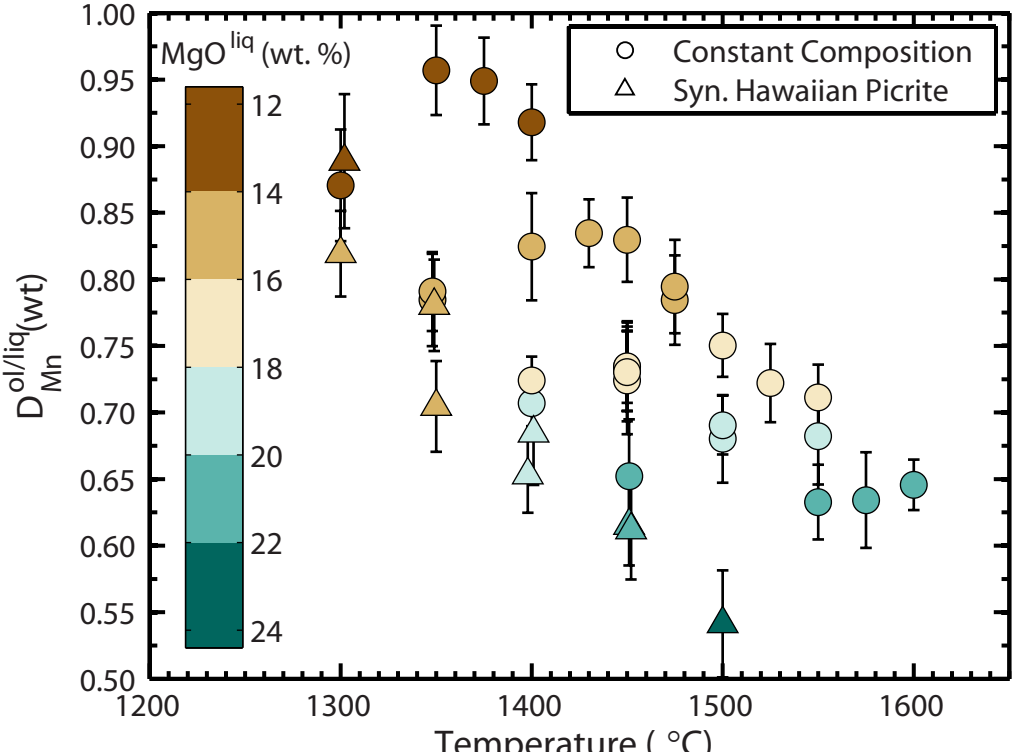
MgO liq (wt. %)
12
14
16
18
20
22
24
Constant Composition
Syn. Hawaiian Picrite
D Mn ol/liq (wt)
1.00
0.95
0.90
0.85
0.80
0.75
0.70
0.65
0.60
0.55
0.50
1200
1300
1400
1500
1600
Temperature (°C)

Figure 3

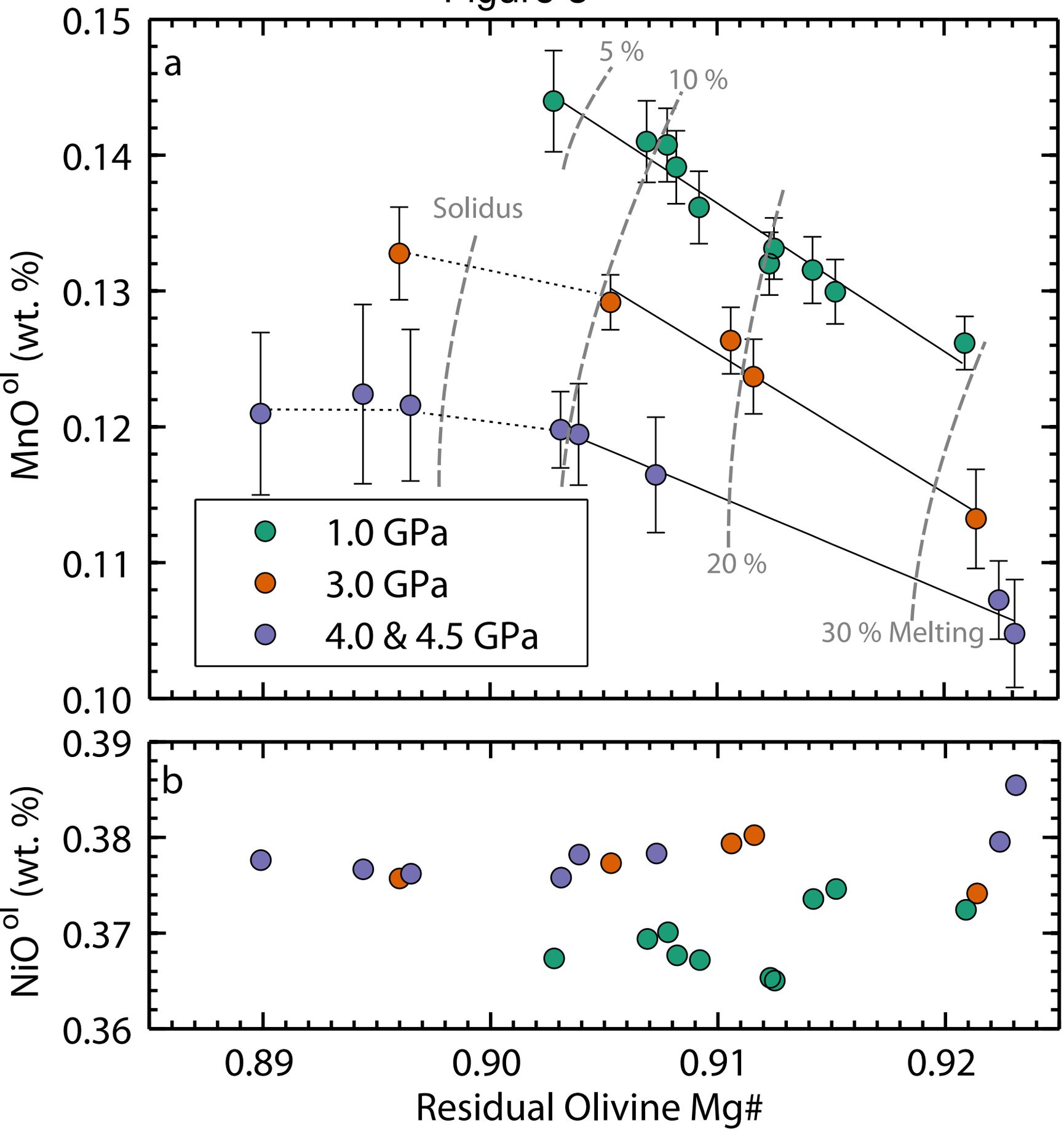
a
b
5 %
10 %
20 %
30 % Melting
Solidus
1.0 GPa
3.0 GPa
4.0 & 4.5 GPa
MnO^ol (wt. %)
NiO^ol (wt. %)
Residual Olivine Mg#
0.15
0.14
0.13
0.12
0.11
0.10
0.39
0.38
0.37
0.36
0.89
0.90
0.91
0.92

Figure 4

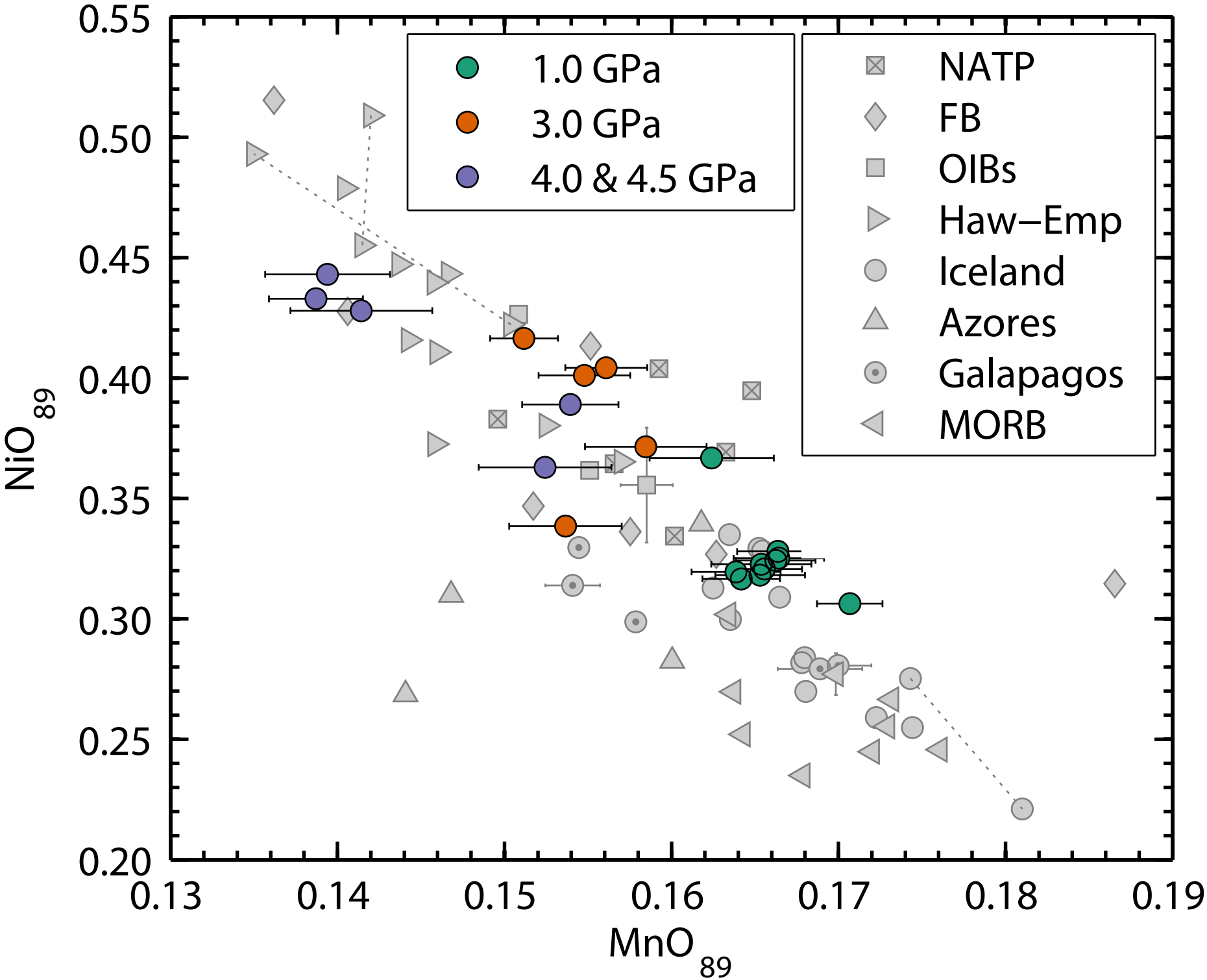
1.0 GPa
3.0 GPa
4.0 & 4.5 GPa
NATP
FB
OIBs
Haw–Emp
Iceland
Azores
Galapagos
MORB
NiO89
MnO89
0.55
0.50
0.45
0.40
0.35
0.30
0.25
0.20
0.13
0.14
0.15
0.16
0.17
0.18
0.19

Figure 5

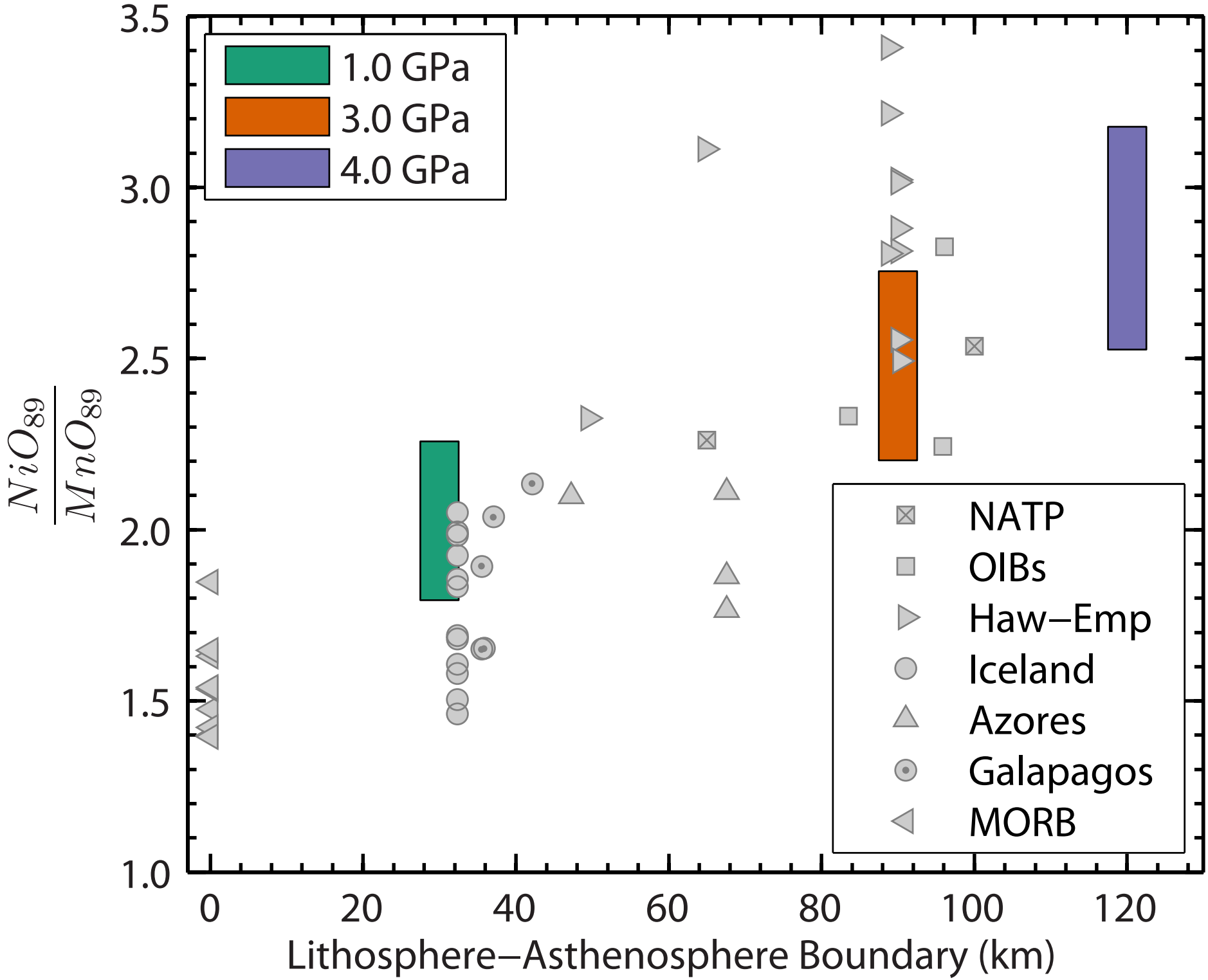
1.0 GPa
3.0 GPa
4.0 GPa
NATP
OIBs
Haw–Emp
Iceland
Azores
Galapagos
MORB
$\frac{NiO_{89}}{MnO_{89}}$
3.5
3.0
2.5
2.0
1.5
1.0
0
20
40
60
80
100
120
Lithosphere–Asthenosphere Boundary (km)

Supplementary Information to the manuscript "The roles of pyroxenite and peridotite in the mantle sources of oceanic basalts," by Andrew K. Matzen, Bernard J. Wood, Michael B. Baker, and Edward M. Stolper.

Figure S1

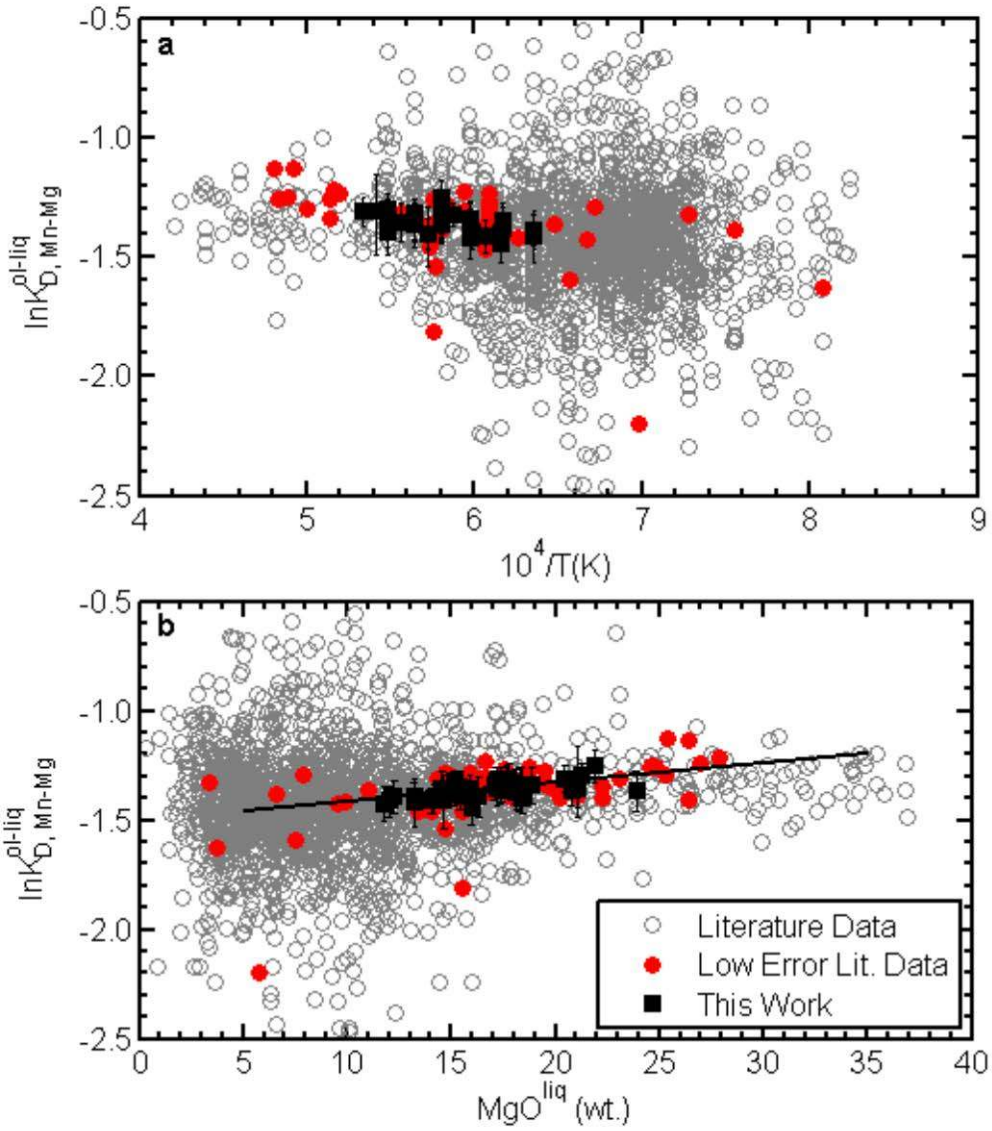

Supplemental Information Figure S1.
Mn-Mg olivine-liquid exchange coefficients vs. 10^4/T(K), (a) and vs. MgO content of experimental liquids (in wt. %), (b). Constant-composition series experiments from this work show no statically-significant temperature dependence (see Supplemental Information Fig. S2), but our work, and high-precision experiments from the literature, show a slight compositional effect on the exchange coefficient. Solid black line in (b) is a bisquare-weighted fit to both the low-error literature data and data from this work (Equation 1, main text). Note that axes are scaled such that 22 experiments are not shown

Figure S2

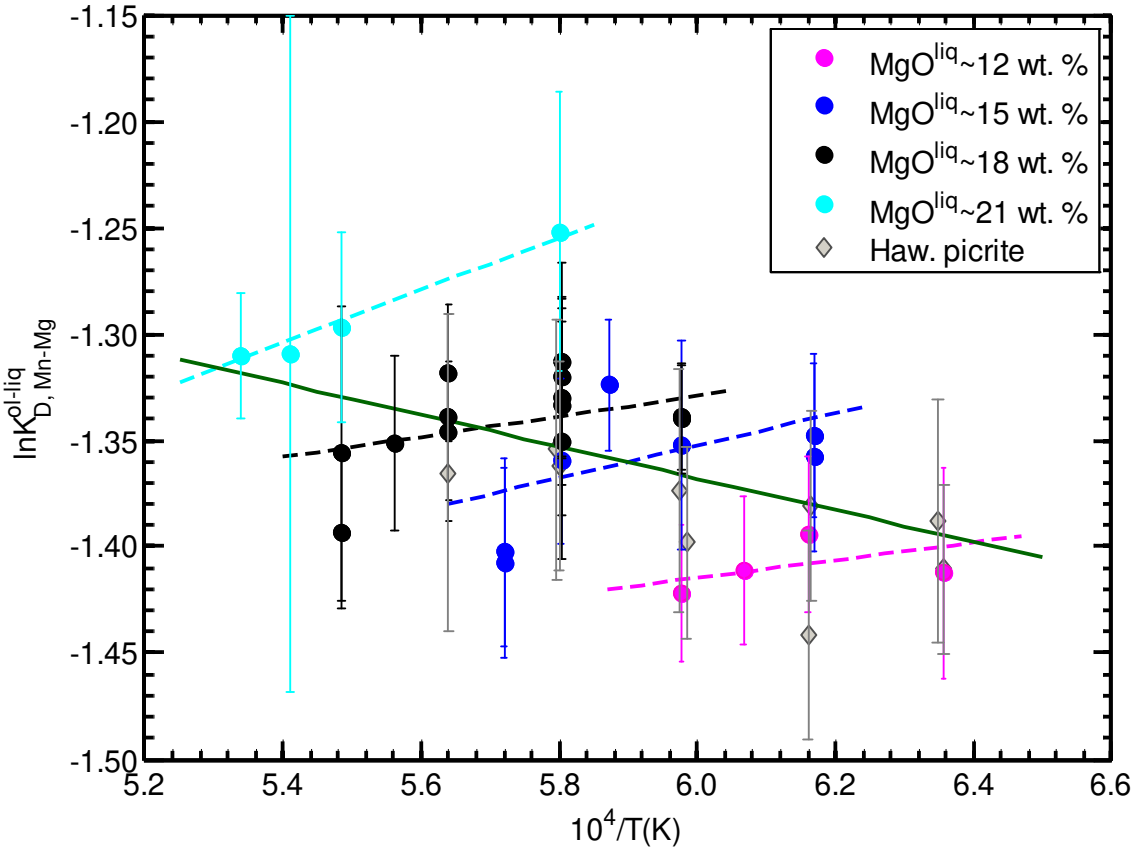

Supplemental Information Figure S2

Mn-Mg olivine-liquid exchange coefficient vs. 10^4/T(K) for only the new data presented here. Weighted fits to the constant composition series (where temperature and pressure were changed in concert to produce liquids with ~12, 15, 18 and 21 wt. % MgO) are shown as dashed lines whose color corresponds to that of the dataset fit, a weighted fit to the dataset as a whole is shown as a solid line. If the assumptions used to arrive at equation 5 are operative, each constant-composition series should have a slope and intercept that is equal to that of the dataset as a whole (see methods).

Figure S3

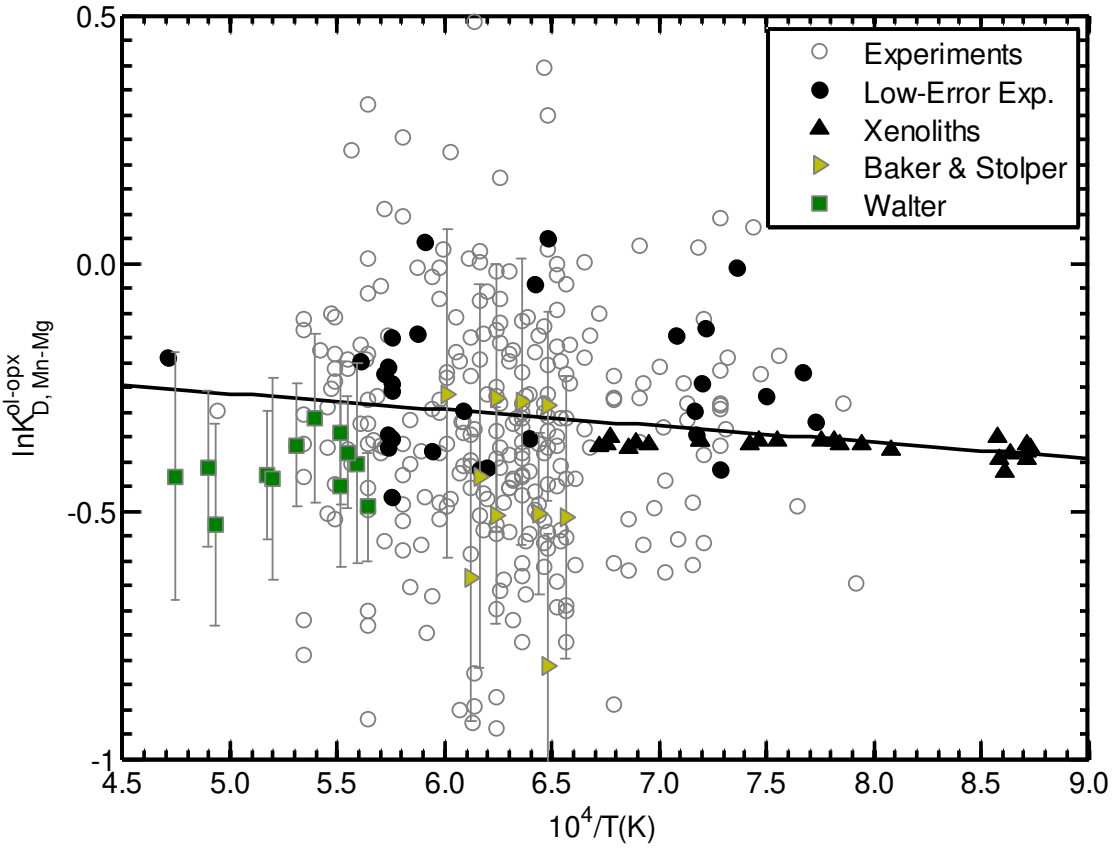

Supplemental Information Figure S3.
Mn-Mg olivine-orthopyroxene exchange coefficient vs. 10^4/T(K), and a bisquare-weighted fit (solid black line). Exchange coefficients from the experiments of Walter[25] (squares) and Baker and Stolper[22] (rightward pointing triangles) are also shown, however they were not included in the fit since their major-element concentrations and phase fractions are used to construct a forward model of Mn and Ni partitioning during partial melting and their MnO contents were not determined to high precision. Note that y-axis minimum is set such that two experiments are not shown.

Figure S4

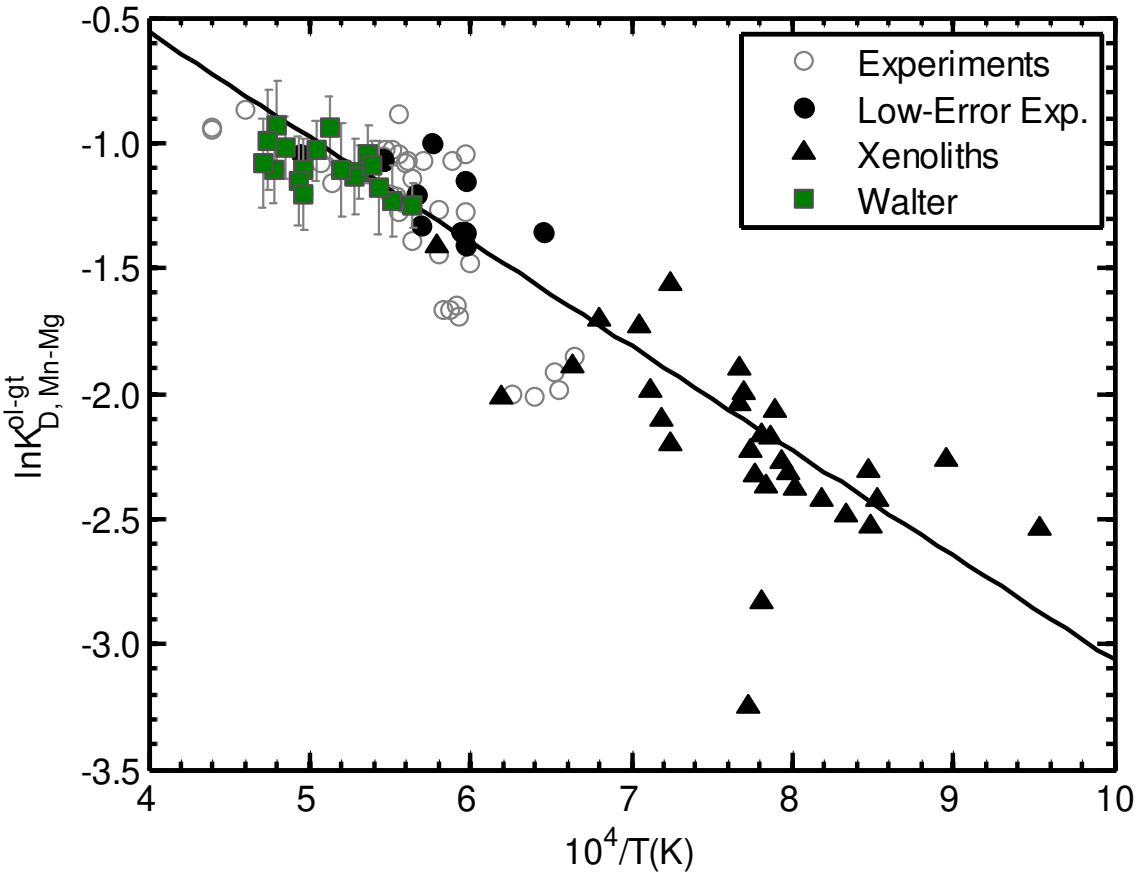

Supplemental Information Figure S4
Mn-Mg olivine-garnet exchange coefficient vs. 10^4/T(K), and a bisquare-weighted fit (solid black line) Exchange coefficients from the experiments of Walter[25] (squares) are also shown, however they were not included in the fit (for explanation, see caption to Supplemental Information Fig. S3).

Figure S5

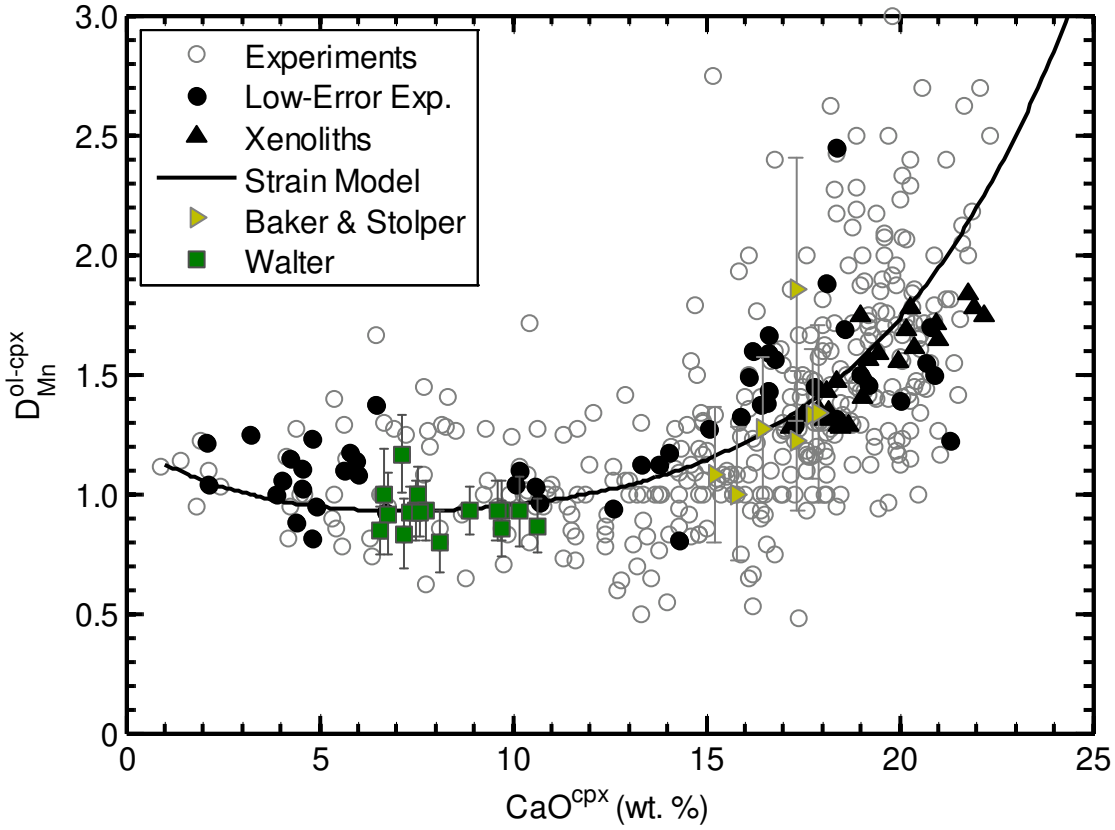

Supplemental Information Figure S5
Partitioning of Mn (in wt. %) between olivine and clinopyroxene; lattice strain model shown as a solid black line (see methods). Coefficients from the experiments of Walter[25] (squares) and Baker and Stolper[22] (rightward pointing triangles) are also shown, however they were not included in the fit (for explanation, see caption to Supplemental Information Fig. S3). Note y-axis is scaled such that 9 experiments with $D_{Mn}^{ol/cpx} > 3$ are not shown.

.

Figure S6

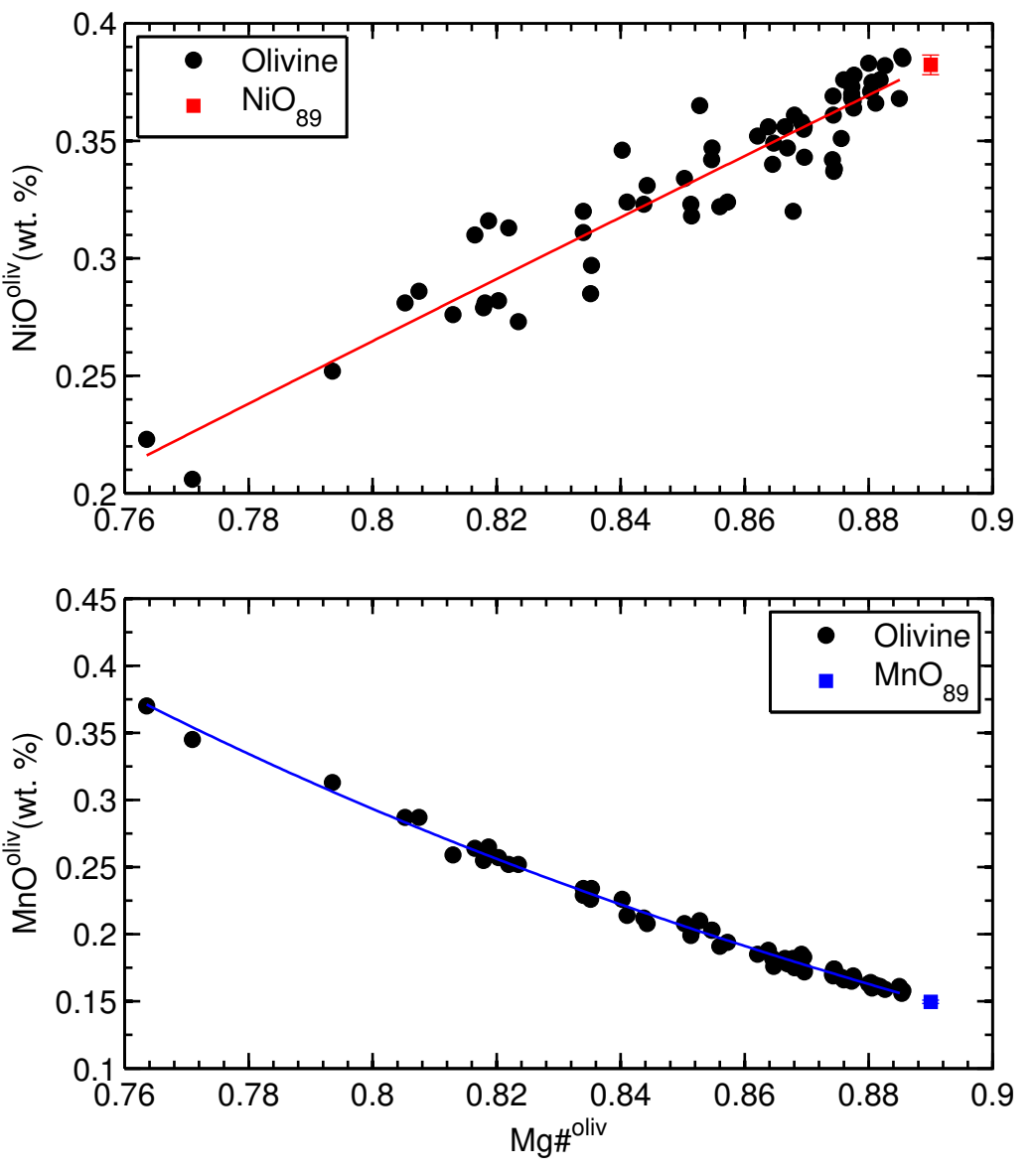
Mull Island–1
Olivine
NiO89
NiOoliv(wt. %)
0.4
0.35
0.3
0.25
0.2
0.76
0.78
0.8
0.82
0.84
0.86
0.88
0.9
Olivine
MnO89
MnOoliv(wt. %)
0.45
0.4
0.35
0.3
0.25
0.2
0.15
0.1
Mg#oliv

Figure S7

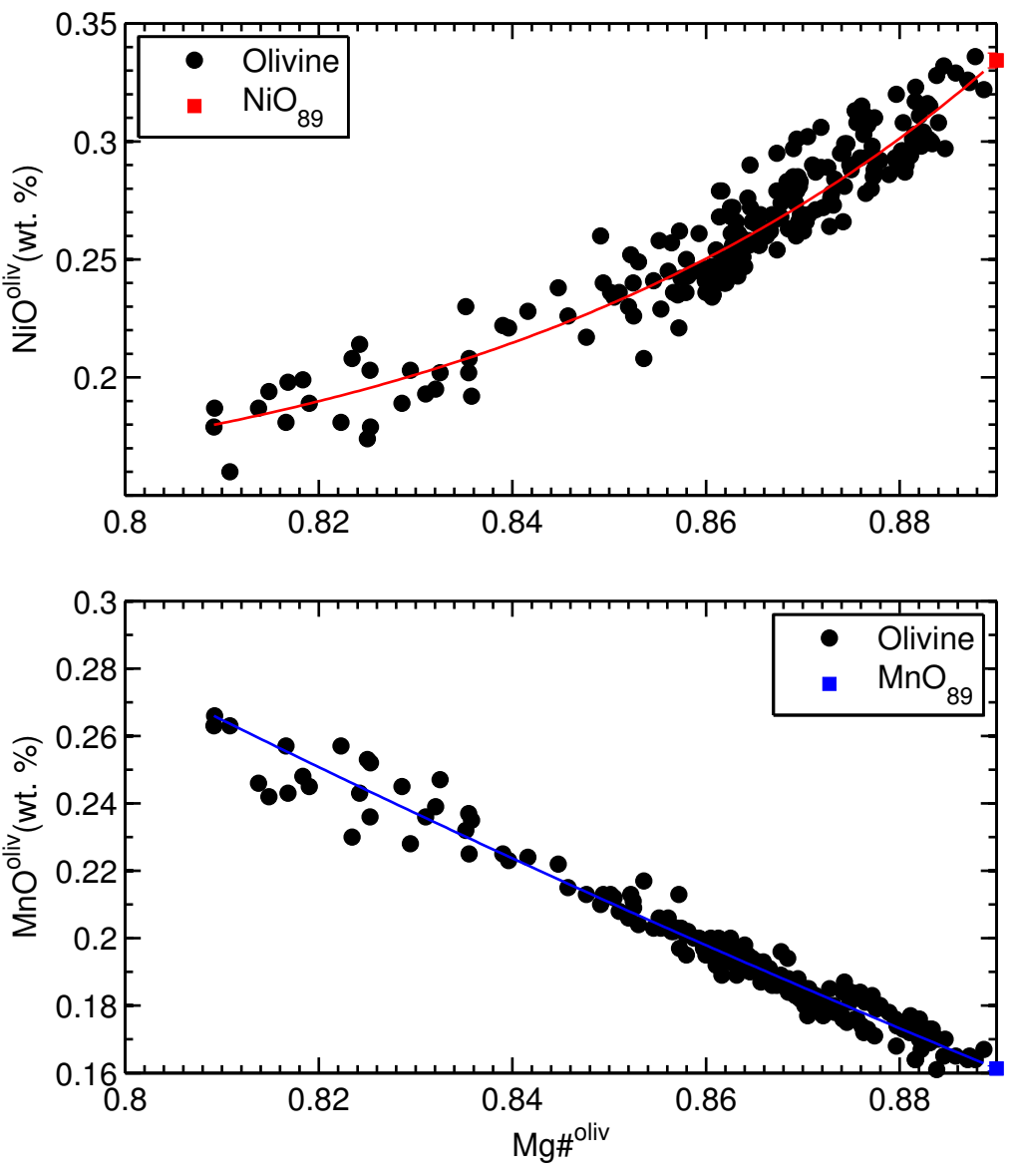
Mull Island–2
Olivine
NiO89
NiOoliv(wt. %)
0.35
0.3
0.25
0.2
0.8
0.82
0.84
0.86
0.88
Olivine
MnO89
MnOoliv(wt. %)
0.3
0.28
0.26
0.24
0.22
0.2
0.18
0.16
0.8
0.82
0.84
0.86
0.88
Mg#oliv

Figure S8

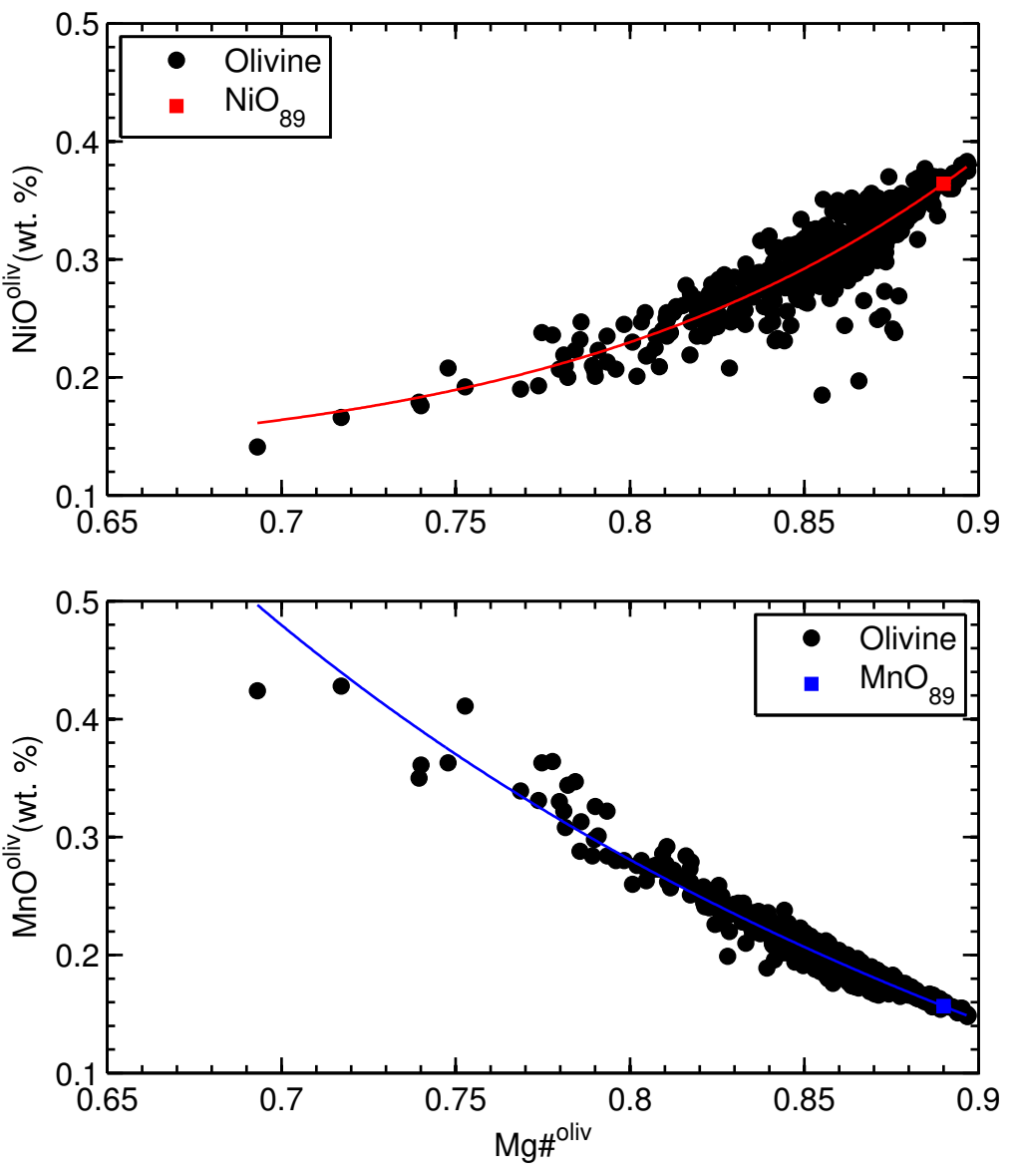
Mull Island–3
Olivine
NiO89
NiOoliv(wt. %)
0.5
0.4
0.3
0.2
0.1
0.65
0.7
0.75
0.8
0.85
0.9
Olivine
MnO89
MnOoliv(wt. %)
Mg#oliv

Figure S9

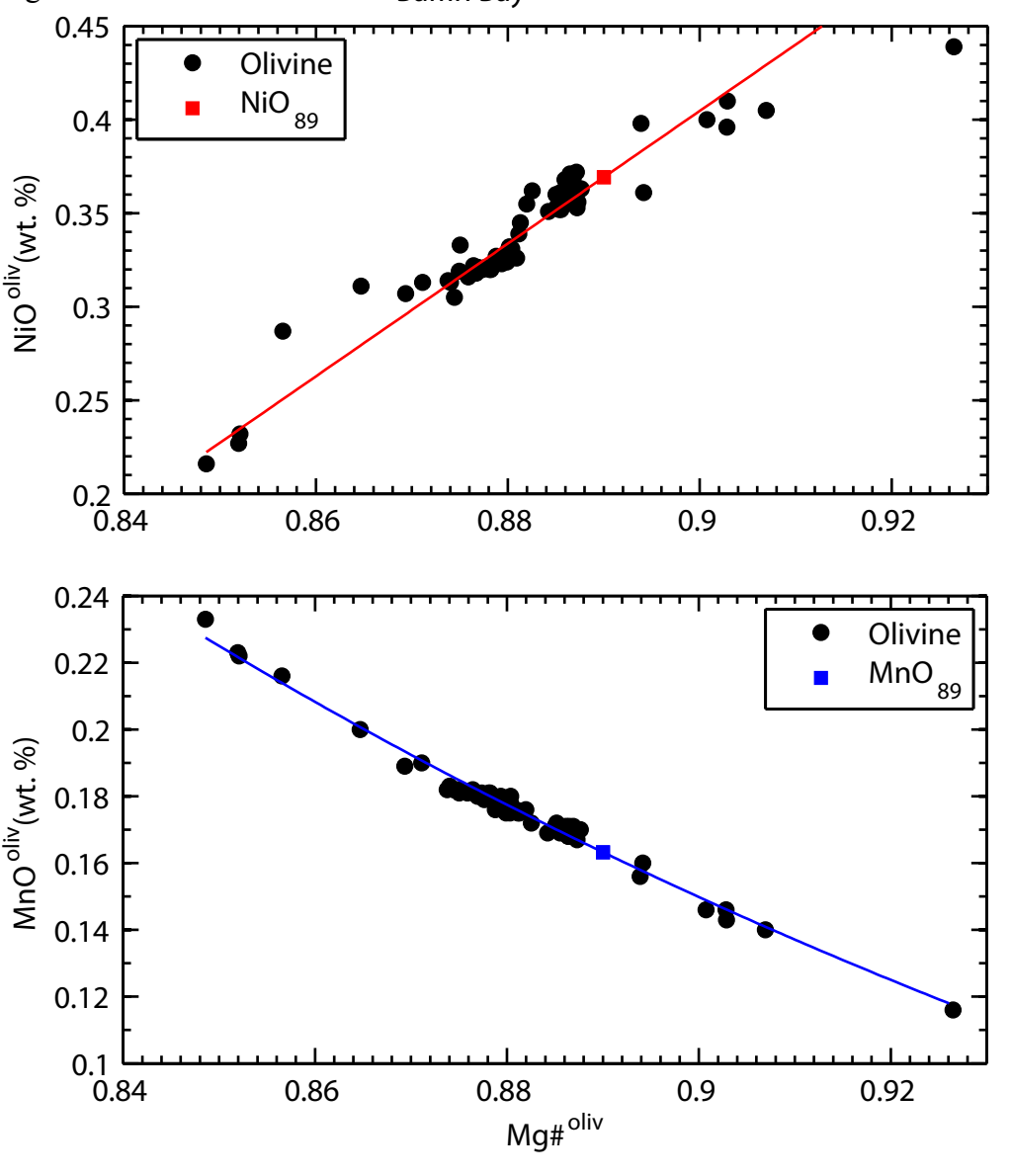
Baffin Bay
Olivine
NiO 89
NiO oliv (wt. %)
0.45
0.4
0.35
0.3
0.25
0.2
0.84
0.86
0.88
0.9
0.92
Olivine
MnO 89
MnO oliv (wt. %)
0.24
0.22
0.2
0.18
0.16
0.14
0.12
0.1
Mg# oliv

Figure S10

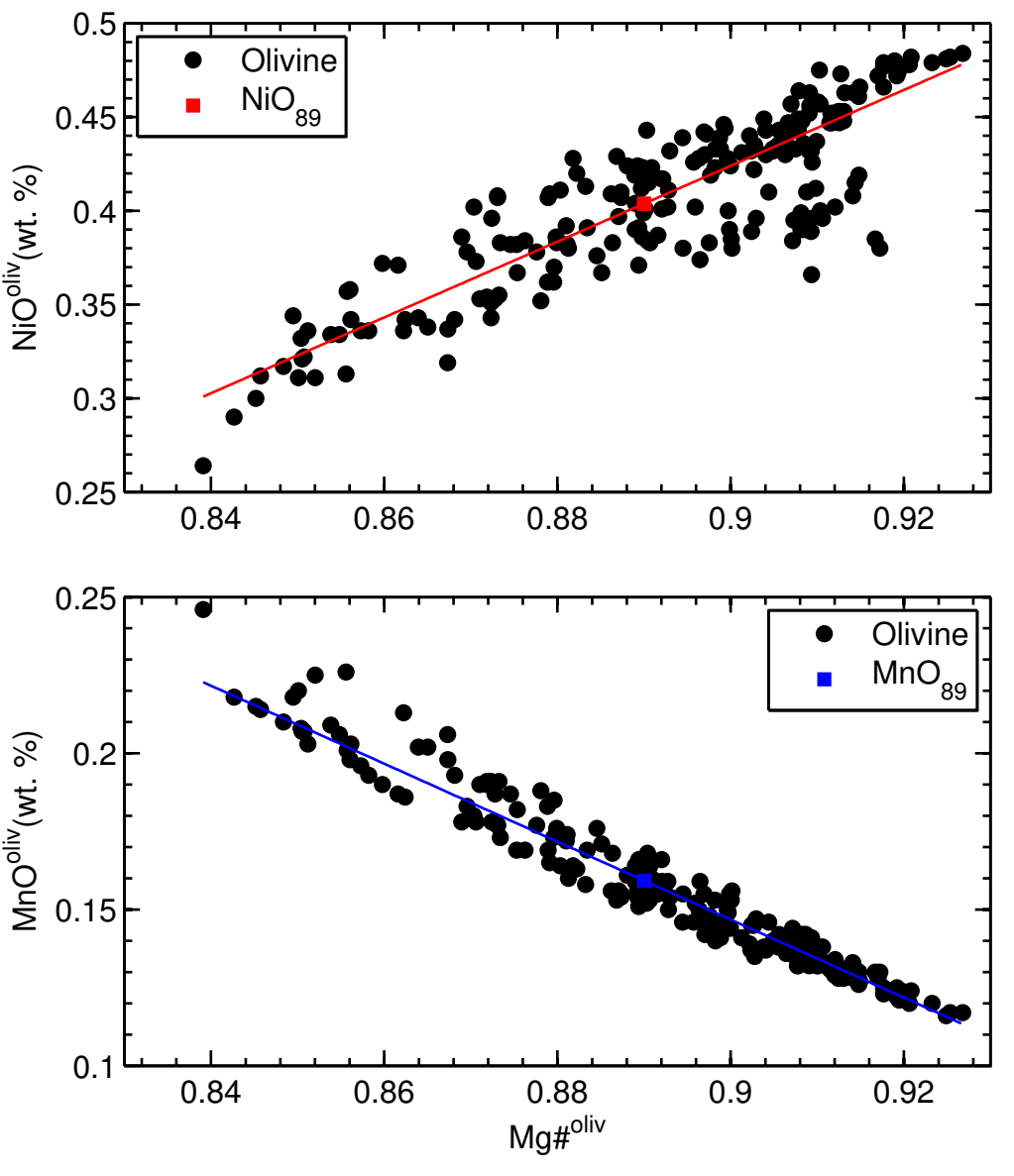
Greenland
Olivine
NiO89
NiOoliv(wt. %)
0.5
0.45
0.4
0.35
0.3
0.25
0.84
0.86
0.88
0.9
0.92
Olivine
MnO89
MnOoliv(wt. %)
0.25
0.2
0.15
0.1
0.84
0.86
0.88
0.9
0.92
Mg#oliv

Figure S11

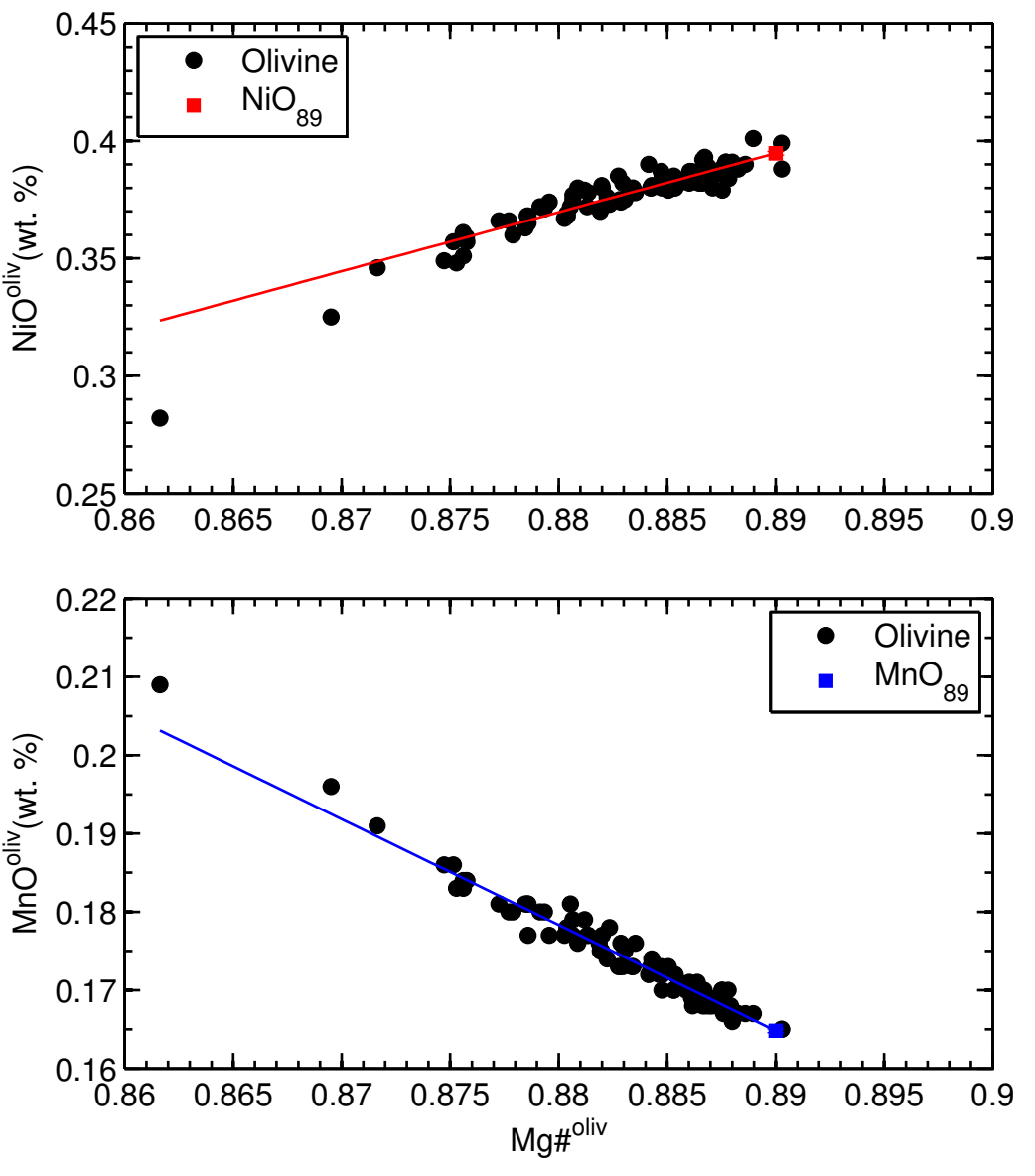
Disko
Olivine
NiO89
NiOoliv(wt. %)
0.45
0.4
0.35
0.3
0.25
0.86
0.865
0.87
0.875
0.88
0.885
0.89
0.895
0.9
Olivine
MnO89
MnOoliv(wt. %)
0.22
0.21
0.2
0.19
0.18
0.17
0.16
Mg#oliv

Figure S12

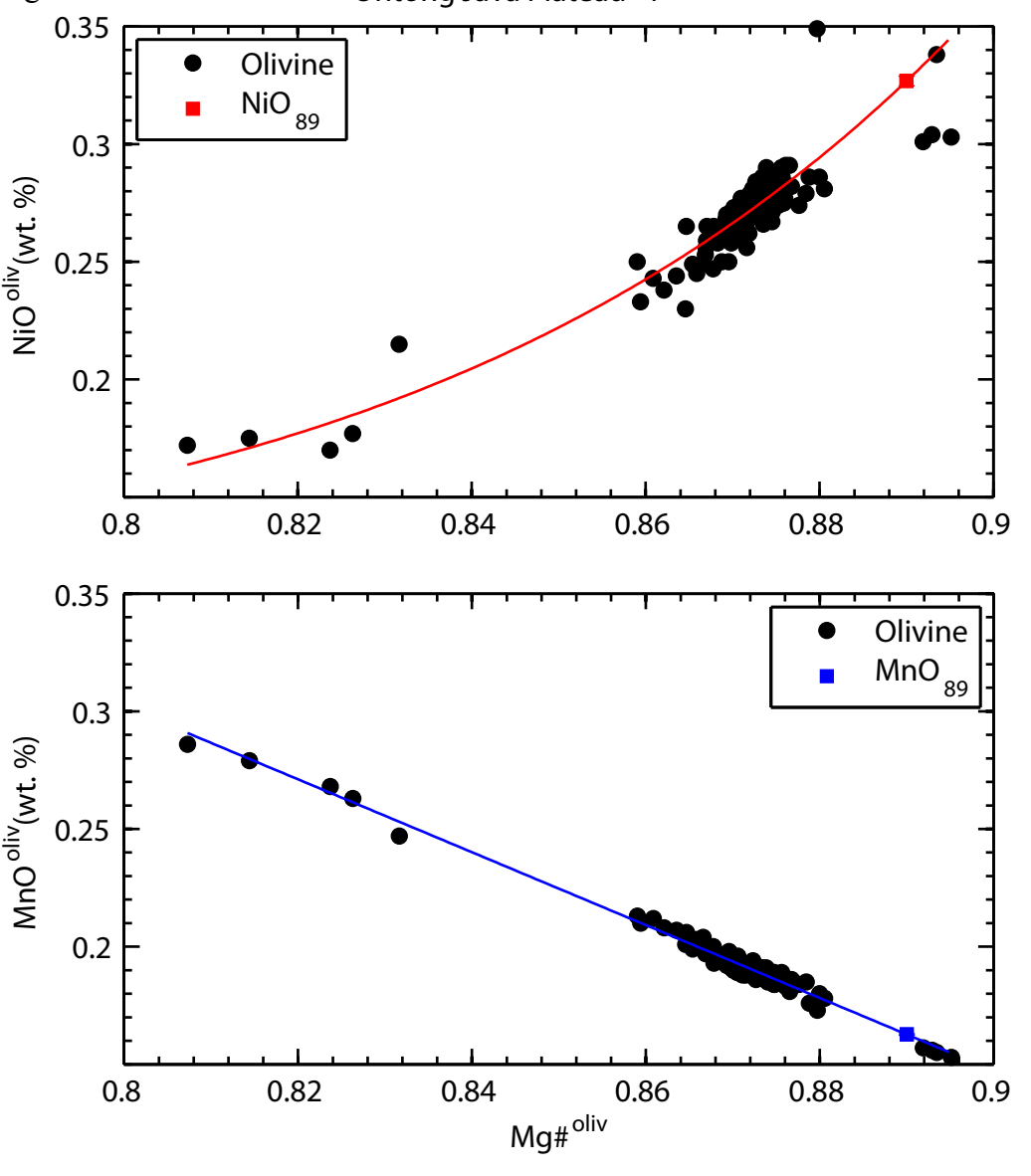
Ontong Java Plateau–1
Olivine
NiO 89
NiO oliv (wt. %)
0.35
0.3
0.25
0.2
0.8
0.82
0.84
0.86
0.88
0.9
Olivine
MnO 89
MnO oliv (wt. %)
Mg# oliv

Figure S13

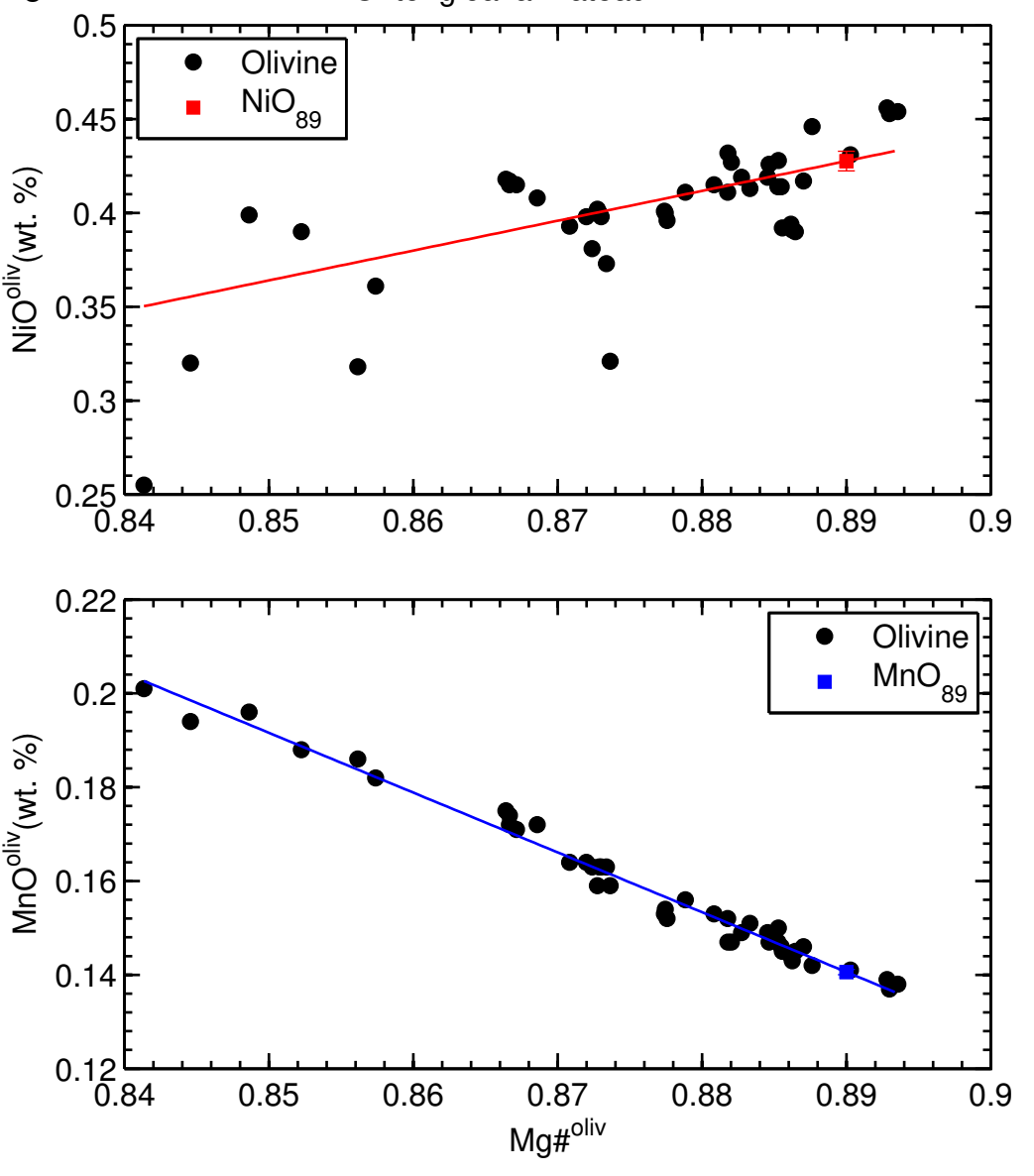
Ontong Java Plateau–2
Olivine
NiO89
NiOoliv(wt. %)
0.5
0.45
0.4
0.35
0.3
0.25
0.84
0.85
0.86
0.87
0.88
0.89
0.9
Olivine
MnO89
MnOoliv(wt. %)
0.22
0.2
0.18
0.16
0.14
0.12
Mg#oliv

Figure S14

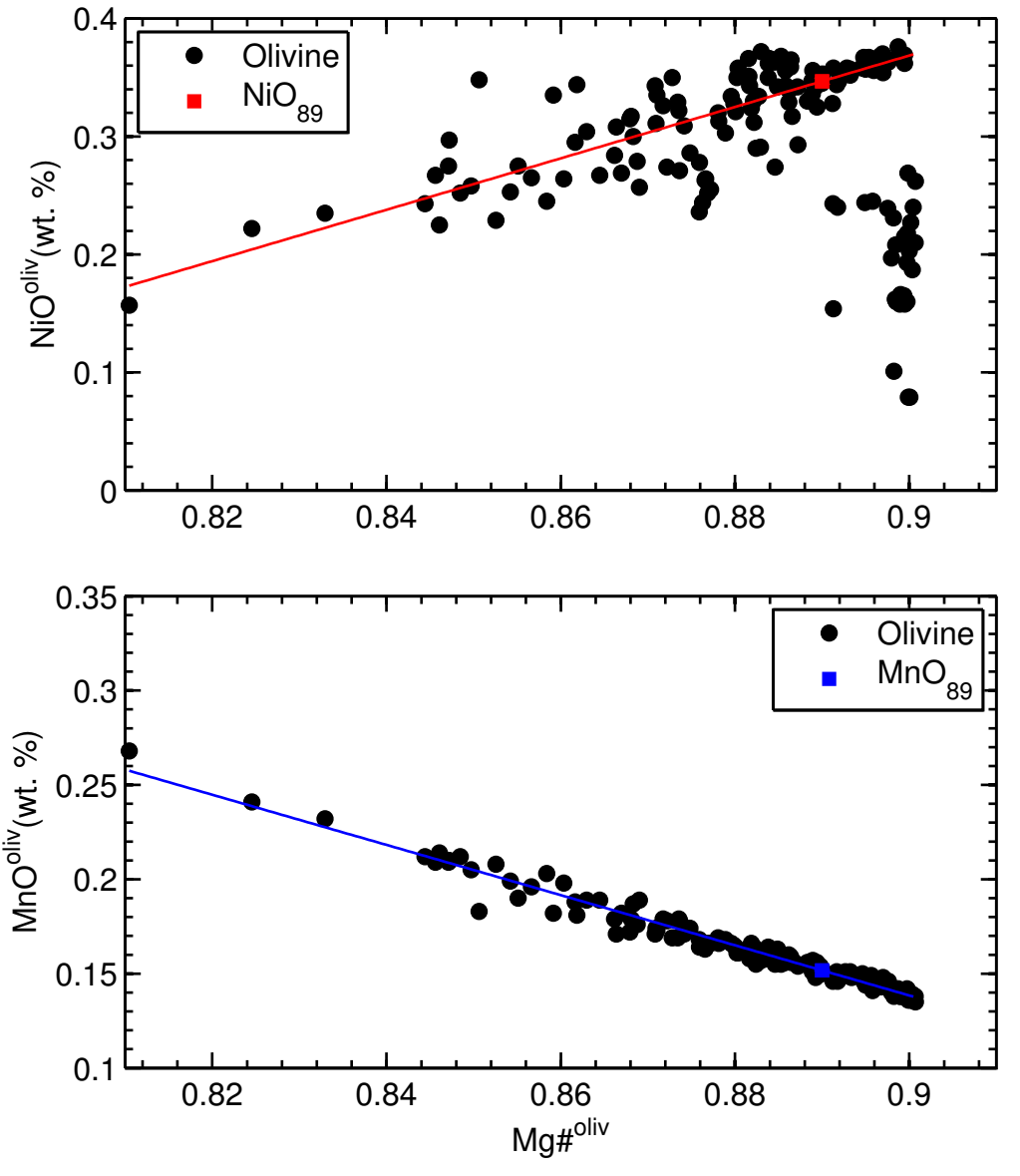
Karoo–1
Olivine
NiO89
NiOoliv(wt. %)
0.4
0.3
0.2
0.1
0
0.82
0.84
0.86
0.88
0.9
Olivine
MnO89
MnOoliv(wt. %)
0.35
0.3
0.25
0.2
0.15
0.1
0.82
0.84
0.86
0.88
0.9
Mg#oliv

Figure S15

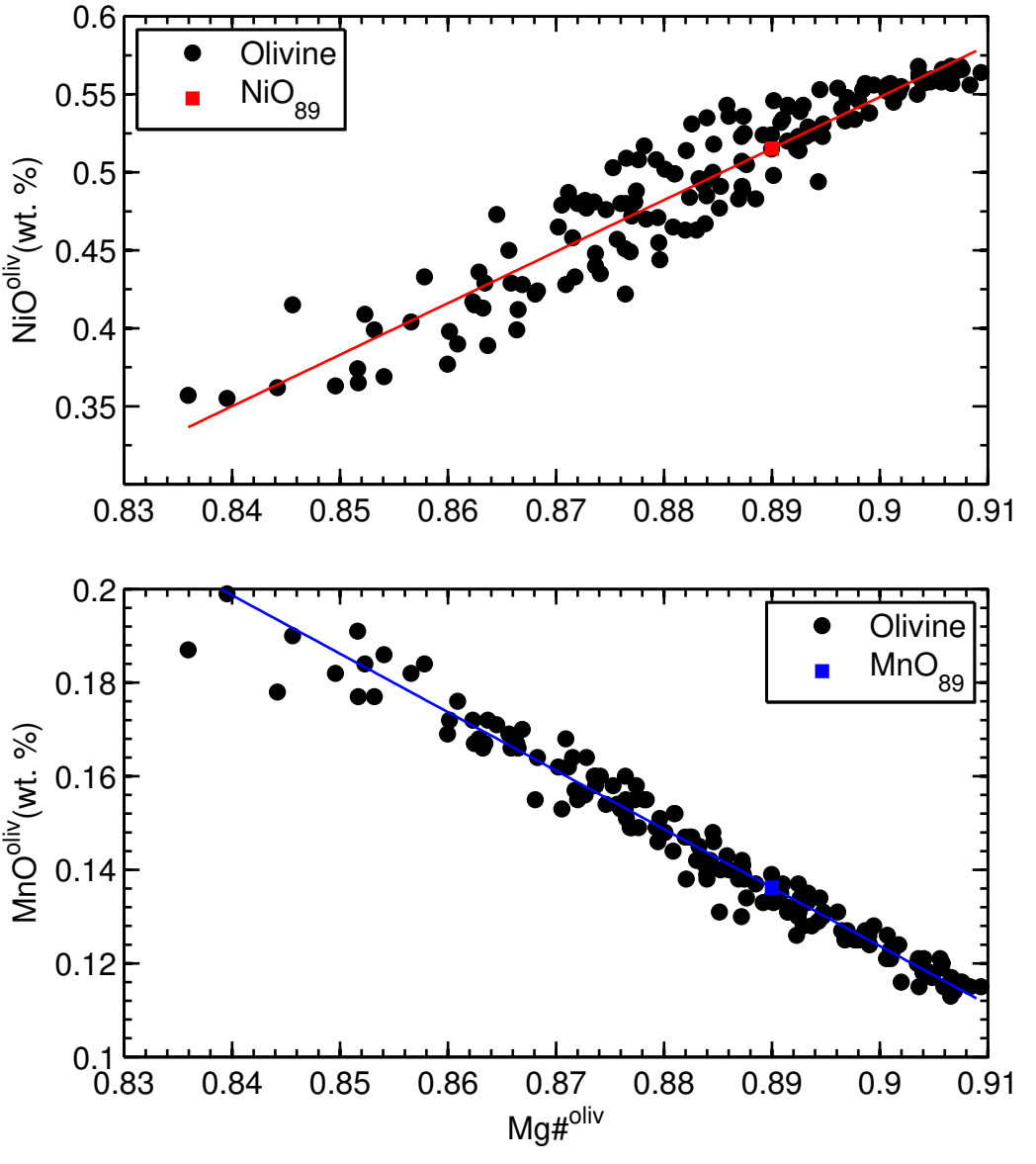
Karoo–2
Olivine
NiO89
NiOoliv(wt. %)
0.6
0.55
0.5
0.45
0.4
0.35
0.83
0.84
0.85
0.86
0.87
0.88
0.89
0.9
0.91
Olivine
MnO89
MnOoliv(wt. %)
0.2
0.18
0.16
0.14
0.12
0.1
Mg#oliv

Figure S16

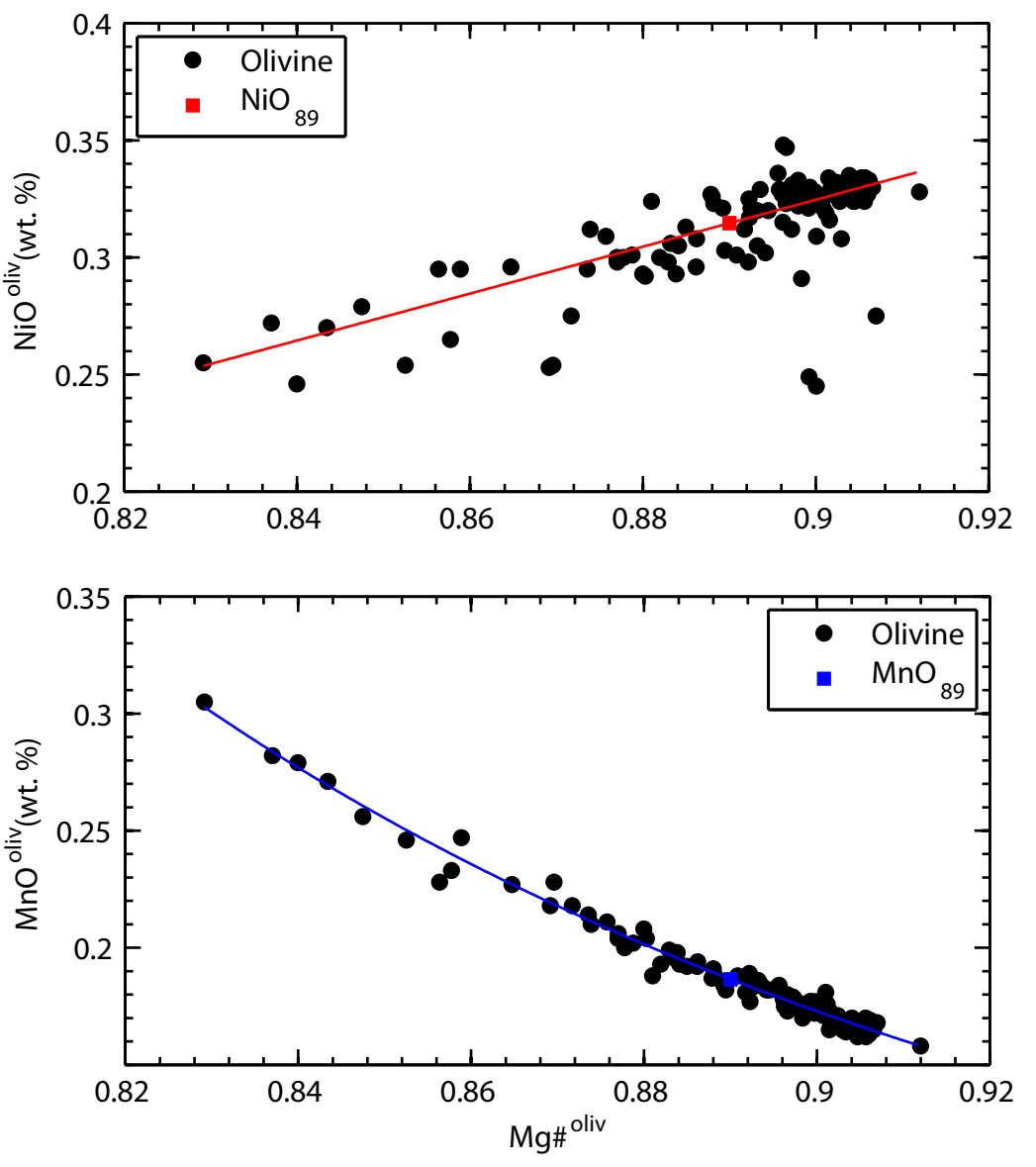
Emeishan−1
Olivine
NiO 89
NiO oliv (wt. %)
0.4
0.35
0.3
0.25
0.2
0.82
0.84
0.86
0.88
0.9
0.92
Olivine
MnO 89
MnO oliv (wt. %)
0.35
0.3
0.25
0.2
0.82
0.84
0.86
0.88
0.9
0.92
Mg# oliv

Figure S17

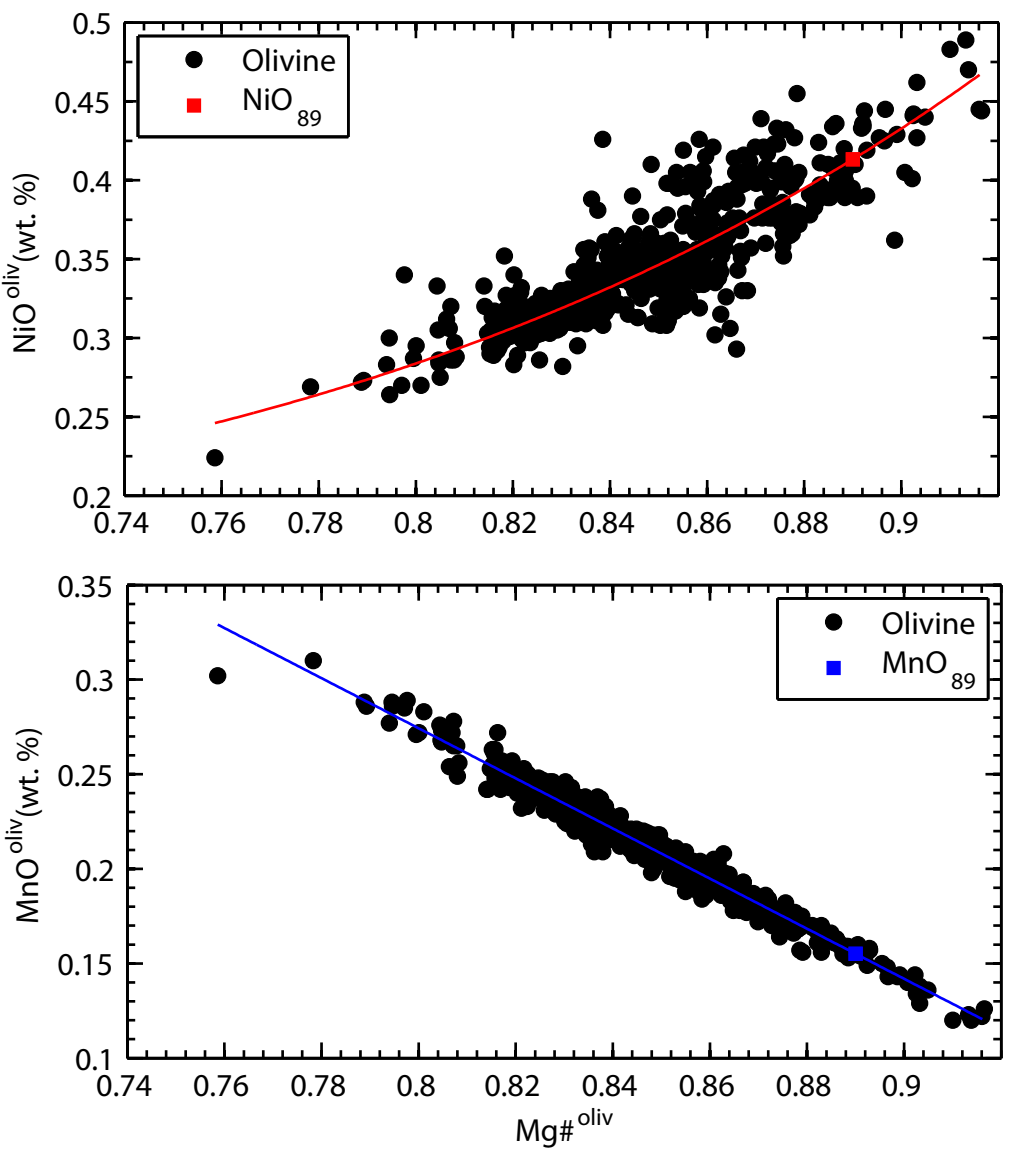
Emeishan−2
Olivine
NiO 89
NiO oliv (wt. %)
0.5
0.45
0.4
0.35
0.3
0.25
0.2
0.74
0.76
0.78
0.8
0.82
0.84
0.86
0.88
0.9
Olivine
MnO 89
MnO oliv (wt. %)
0.35
0.3
0.25
0.2
0.15
0.1
Mg# oliv

Figure S18

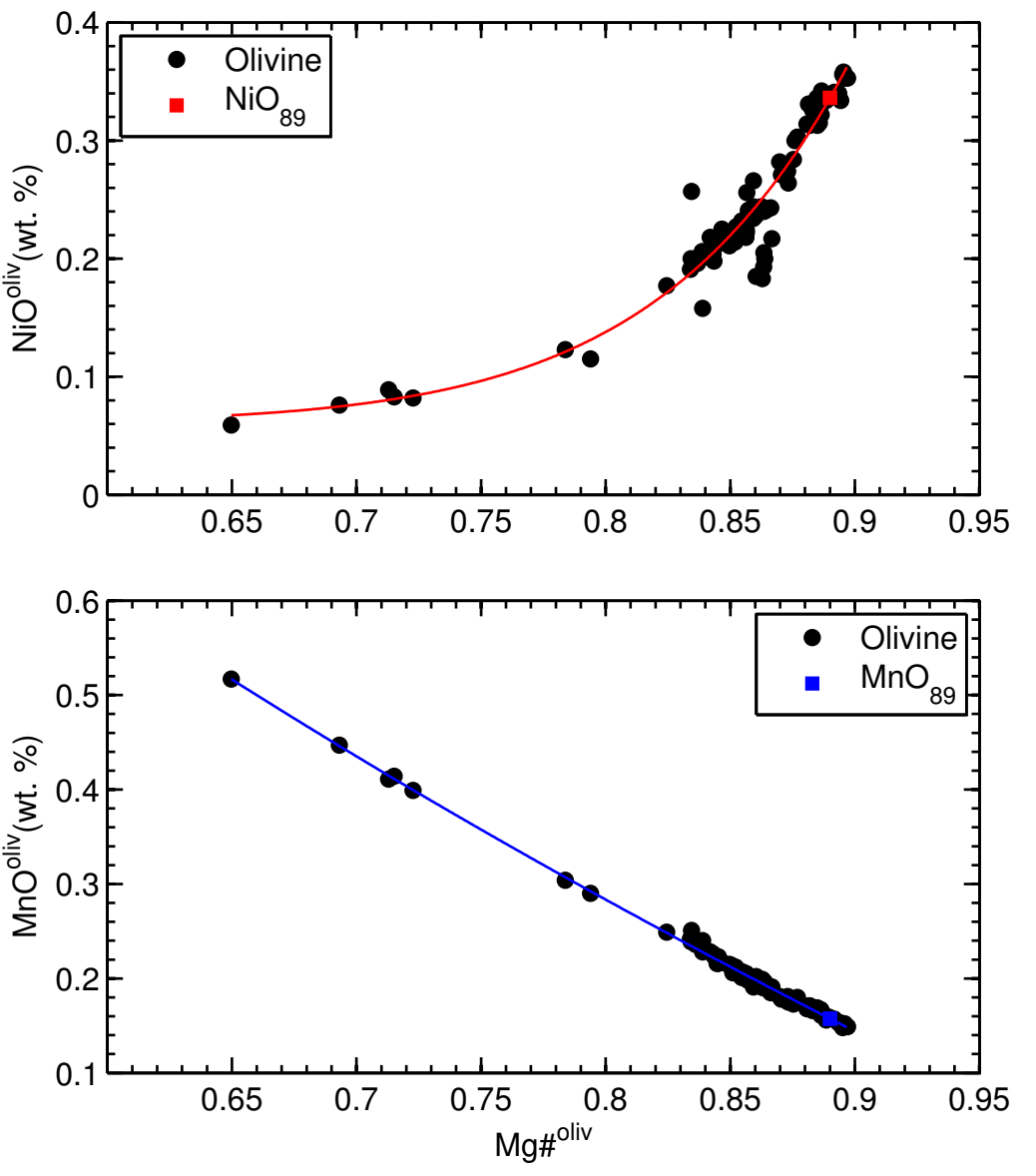
Zawl–Kelkelti
Olivine
NiO89
NiOoliv(wt. %)
0.4
0.3
0.2
0.1
0
0.65
0.7
0.75
0.8
0.85
0.9
0.95
Olivine
MnO89
MnOoliv(wt. %)
0.6
0.5
0.4
0.3
0.2
0.1
Mg#oliv

Figure S19

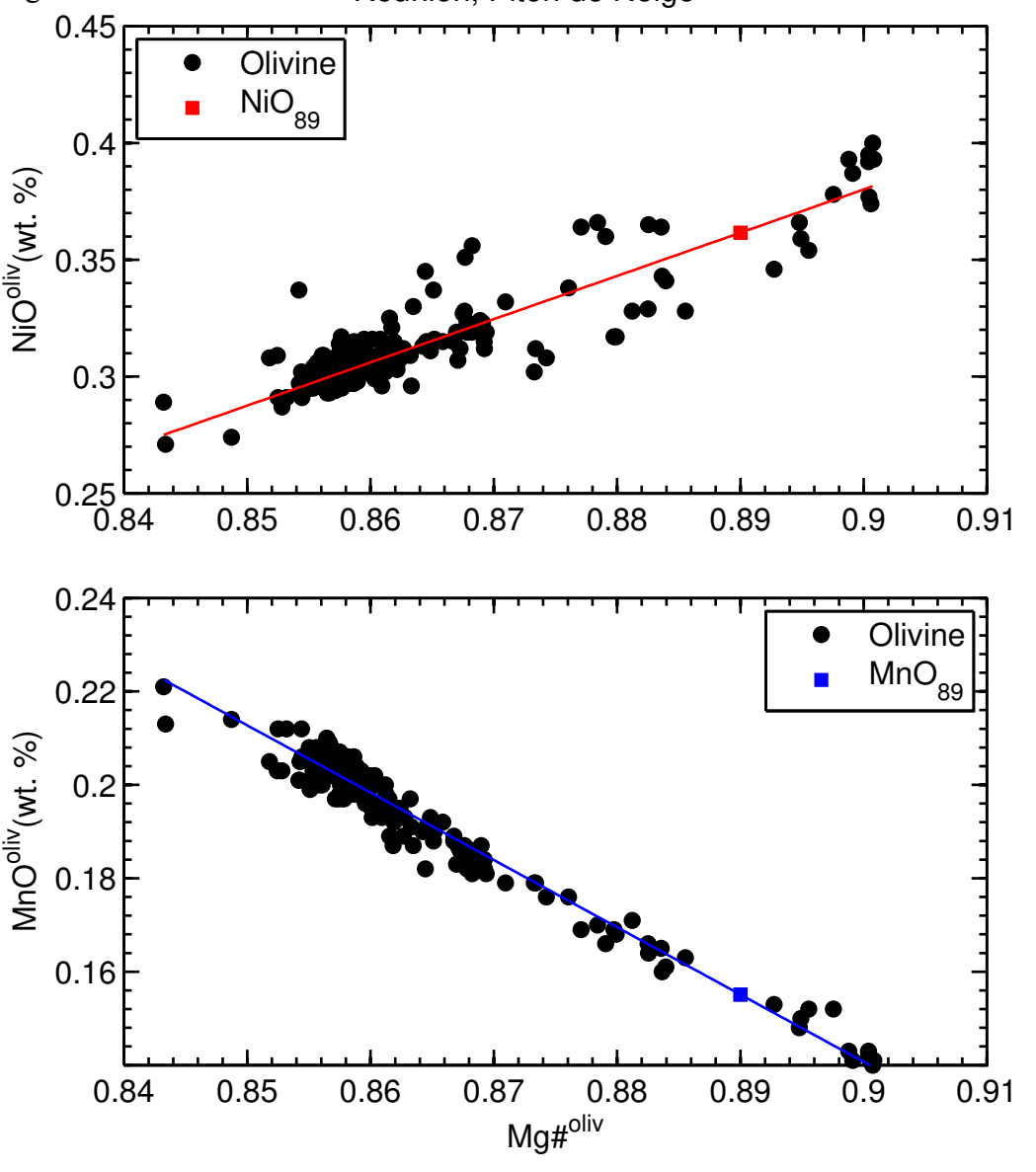
Reunion, Piton de Neige
Olivine
NiO89
NiOoliv(wt. %)
0.45
0.4
0.35
0.3
0.25
0.84
0.85
0.86
0.87
0.88
0.89
0.9
0.91
Olivine
MnO89
MnOoliv(wt. %)
0.24
0.22
0.2
0.18
0.16
Mg#oliv

Figure S20

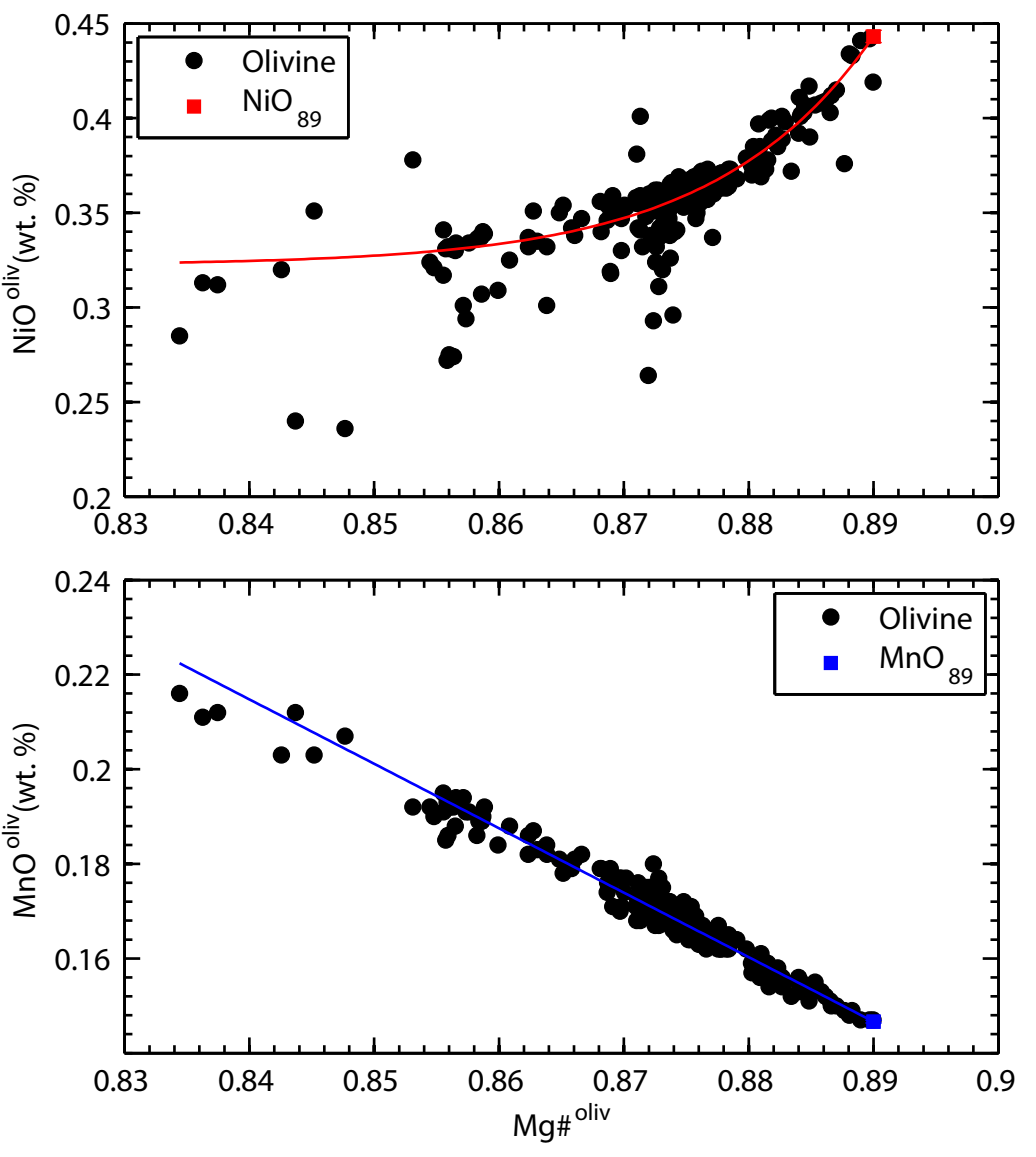
Kilauea Iki
Olivine
NiO 89
NiO oliv (wt. %)
0.45
0.4
0.35
0.3
0.25
0.2
0.83
0.84
0.85
0.86
0.87
0.88
0.89
0.9
Olivine
MnO 89
MnO oliv (wt. %)
0.24
0.22
0.2
0.18
0.16
Mg# oliv

Figure S21

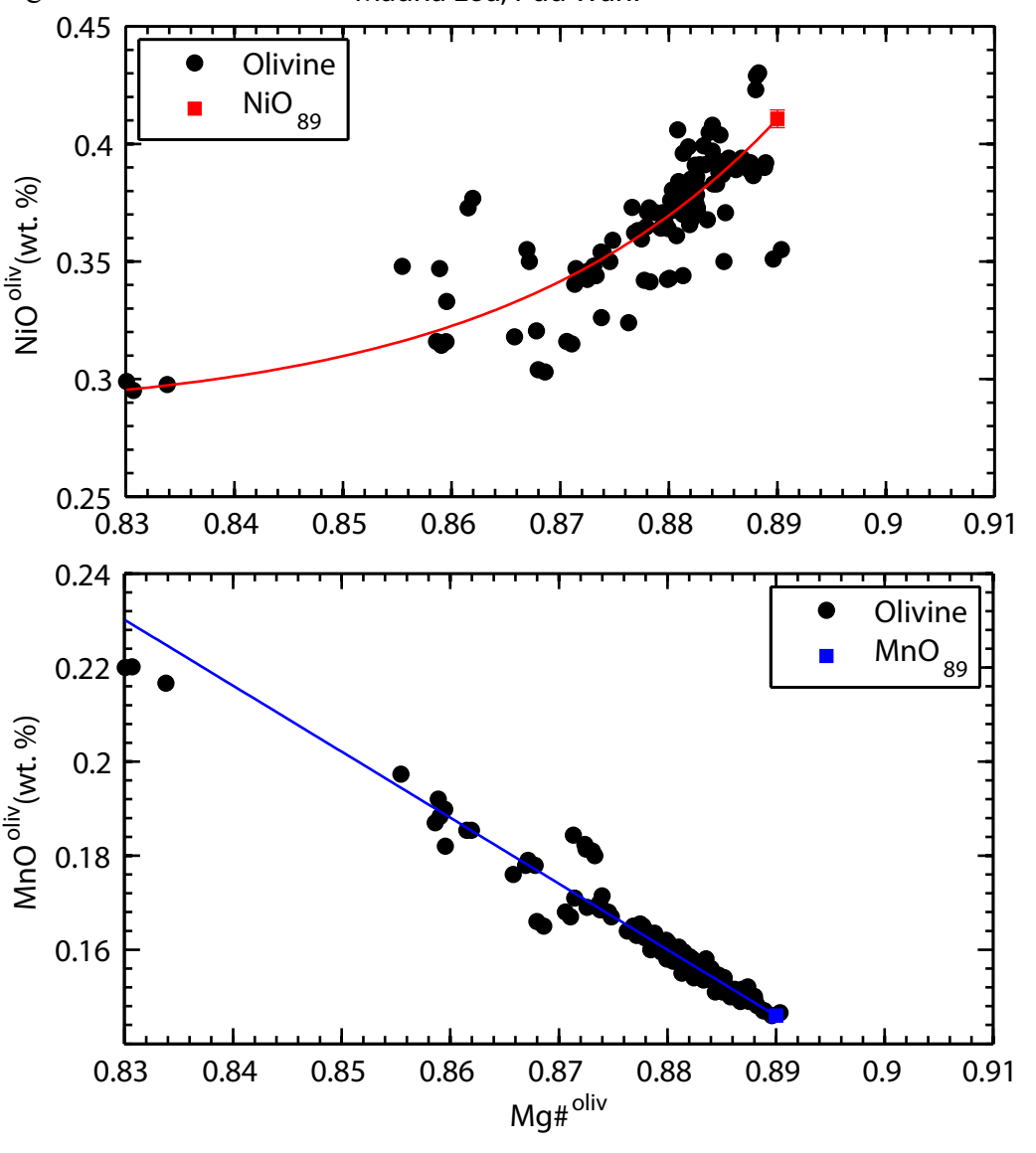
Mauna Loa, Puu Wahi
Olivine
NiO 89
NiO oliv (wt. %)
0.45
0.4
0.35
0.3
0.25
0.83
0.84
0.85
0.86
0.87
0.88
0.89
0.9
0.91
Olivine
MnO 89
MnO oliv (wt. %)
0.24
0.22
0.2
0.18
0.16
Mg# oliv

Figure S22

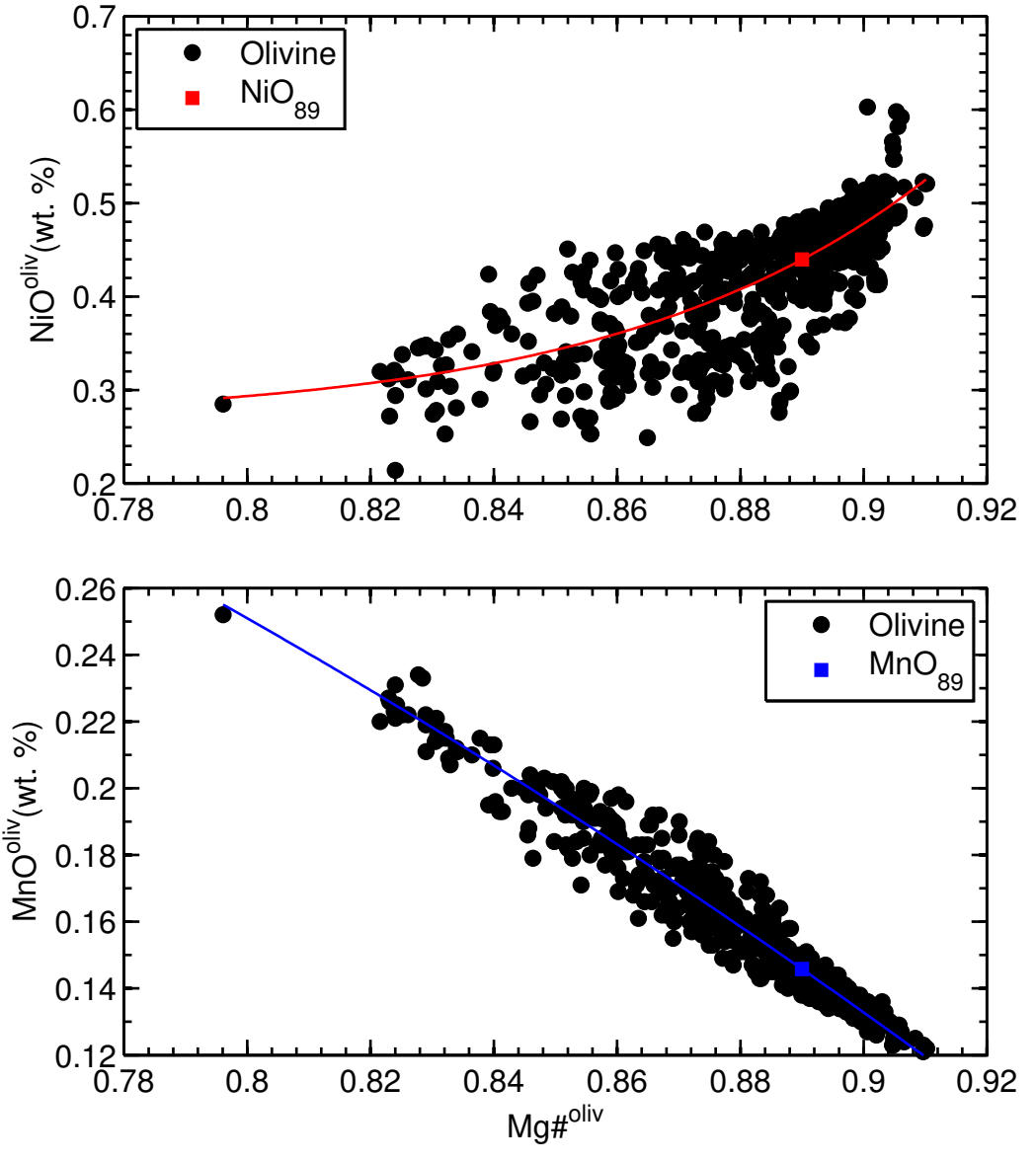
Mauna Loa, HSDP–2
Olivine
NiO89
NiOoliv(wt. %)
0.7
0.6
0.5
0.4
0.3
0.2
0.78
0.8
0.82
0.84
0.86
0.88
0.9
0.92
Olivine
MnO89
MnOoliv(wt. %)
0.26
0.24
0.22
0.2
0.18
0.16
0.14
0.12
0.78
0.8
0.82
0.84
0.86
0.88
0.9
0.92
Mg#oliv

Figure S23

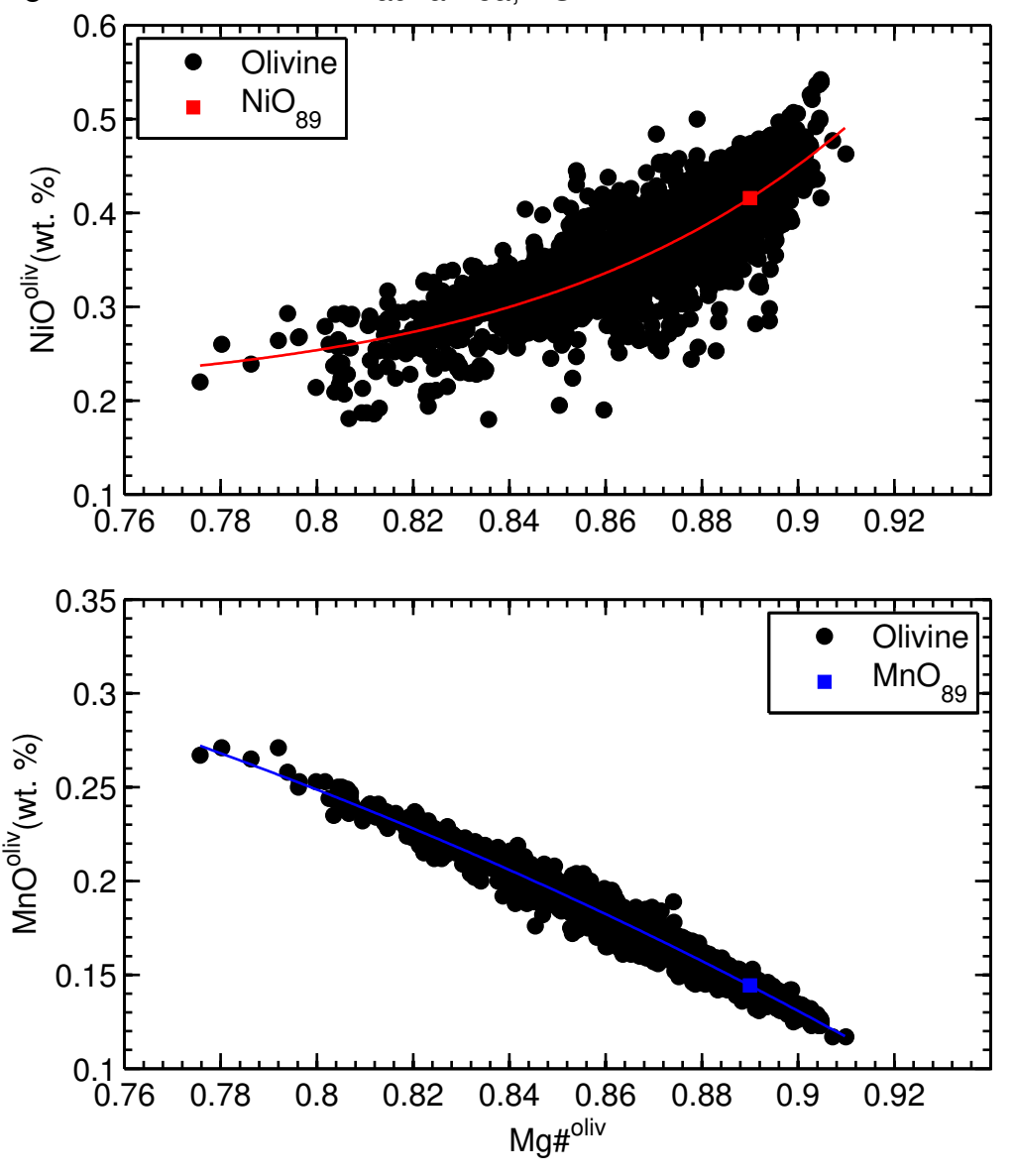
Mauna Kea, HSDP–2
Olivine
NiO89
NiOoliv(wt. %)
0.6
0.5
0.4
0.3
0.2
0.1
0.76
0.78
0.8
0.82
0.84
0.86
0.88
0.9
0.92
Olivine
MnO89
MnOoliv(wt. %)
0.35
0.3
0.25
0.2
0.15
0.1
Mg#oliv

Figure S24

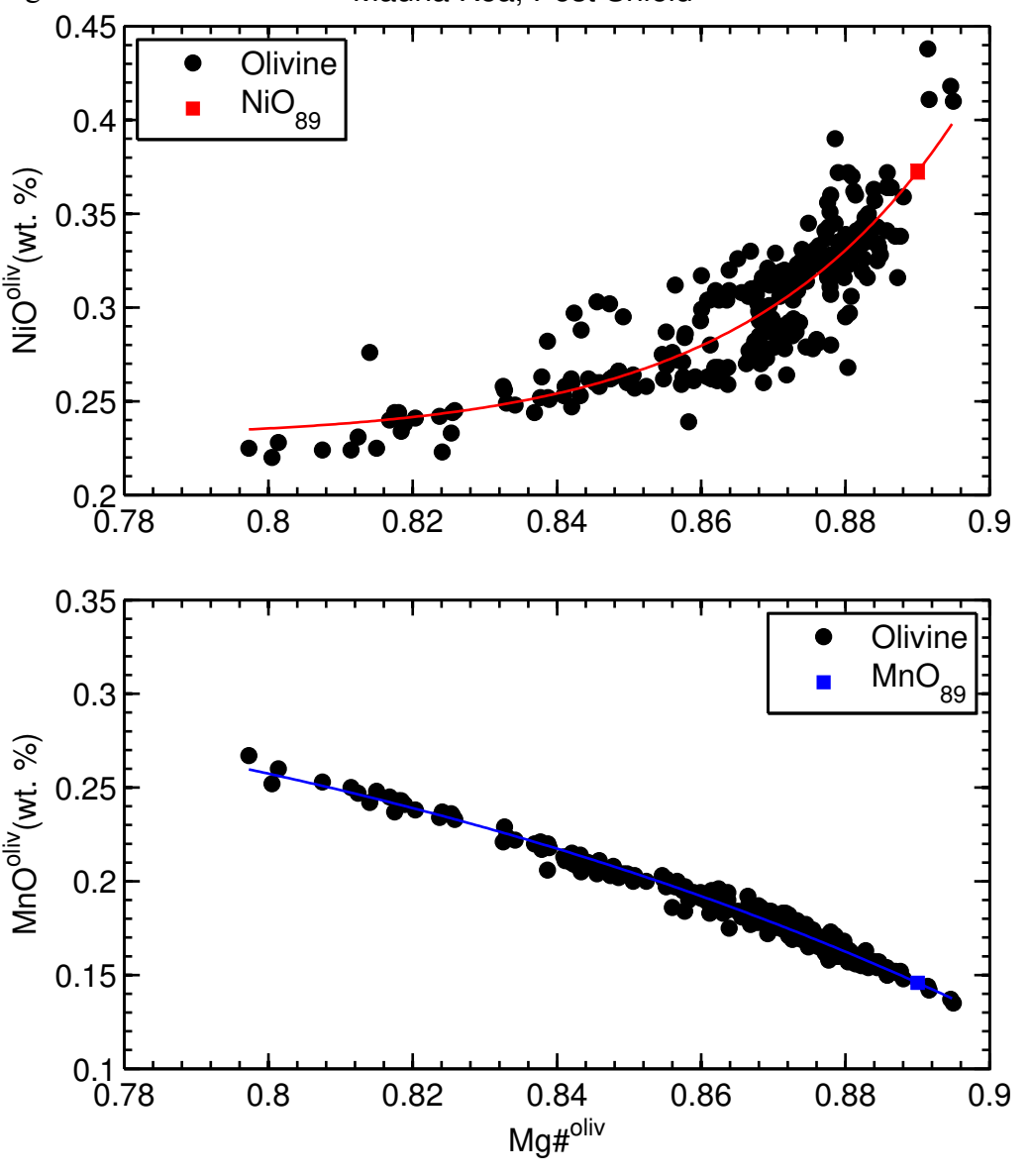
Mauna Kea, Post Shield
Olivine
NiO89
NiOoliv(wt. %)
0.45
0.4
0.35
0.3
0.25
0.2
0.78
0.8
0.82
0.84
0.86
0.88
0.9
Olivine
MnO89
MnOoliv(wt. %)
0.35
0.3
0.25
0.2
0.15
0.1
Mg#oliv

Figure S25

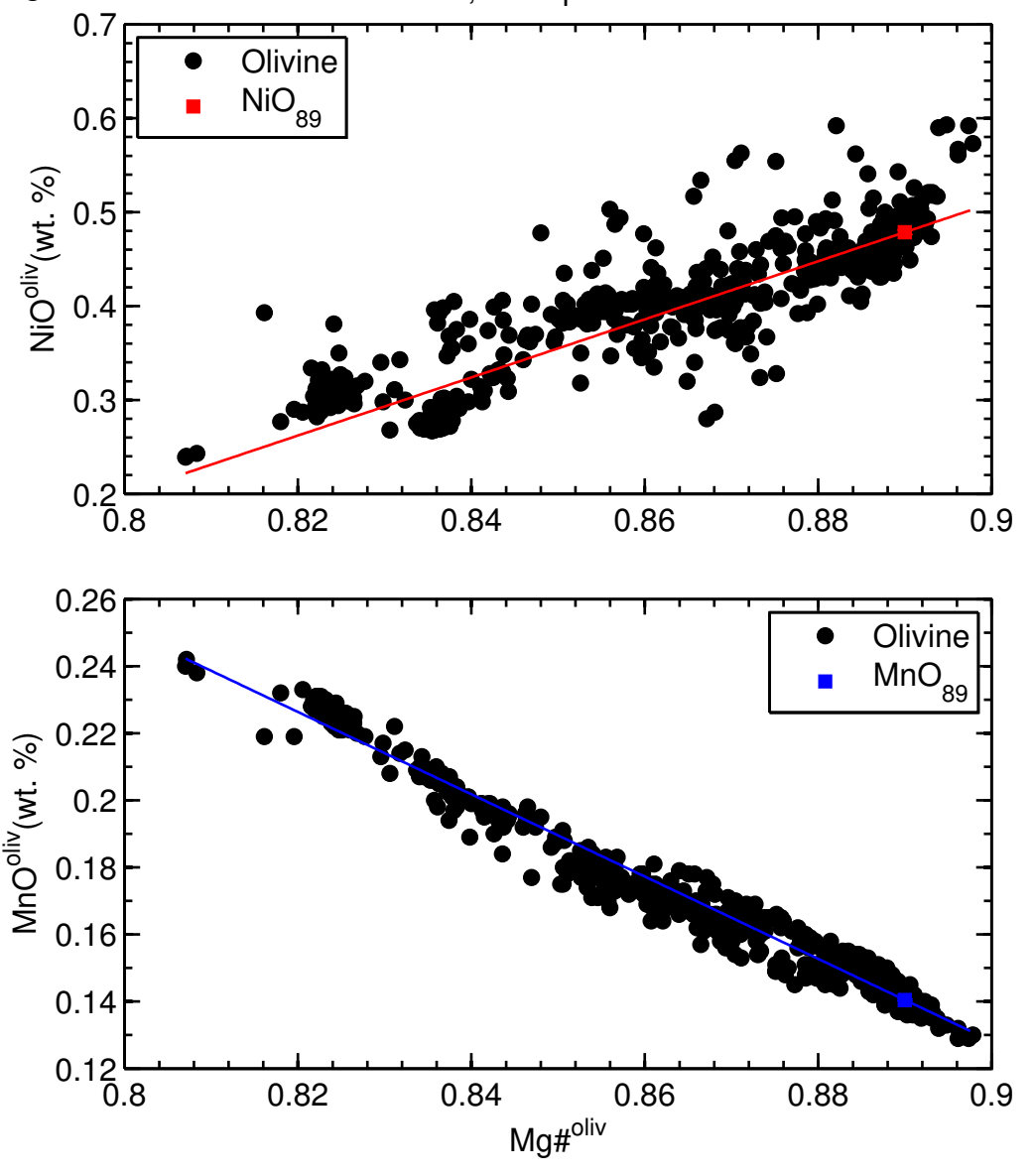
Koolau, Makapuu
Olivine
NiO89
NiOoliv(wt. %)
0.7
0.6
0.5
0.4
0.3
0.2
0.8
0.82
0.84
0.86
0.88
0.9
Olivine
MnO89
MnOoliv(wt. %)
0.26
0.24
0.22
0.2
0.18
0.16
0.14
0.12
Mg#oliv

Figure S26

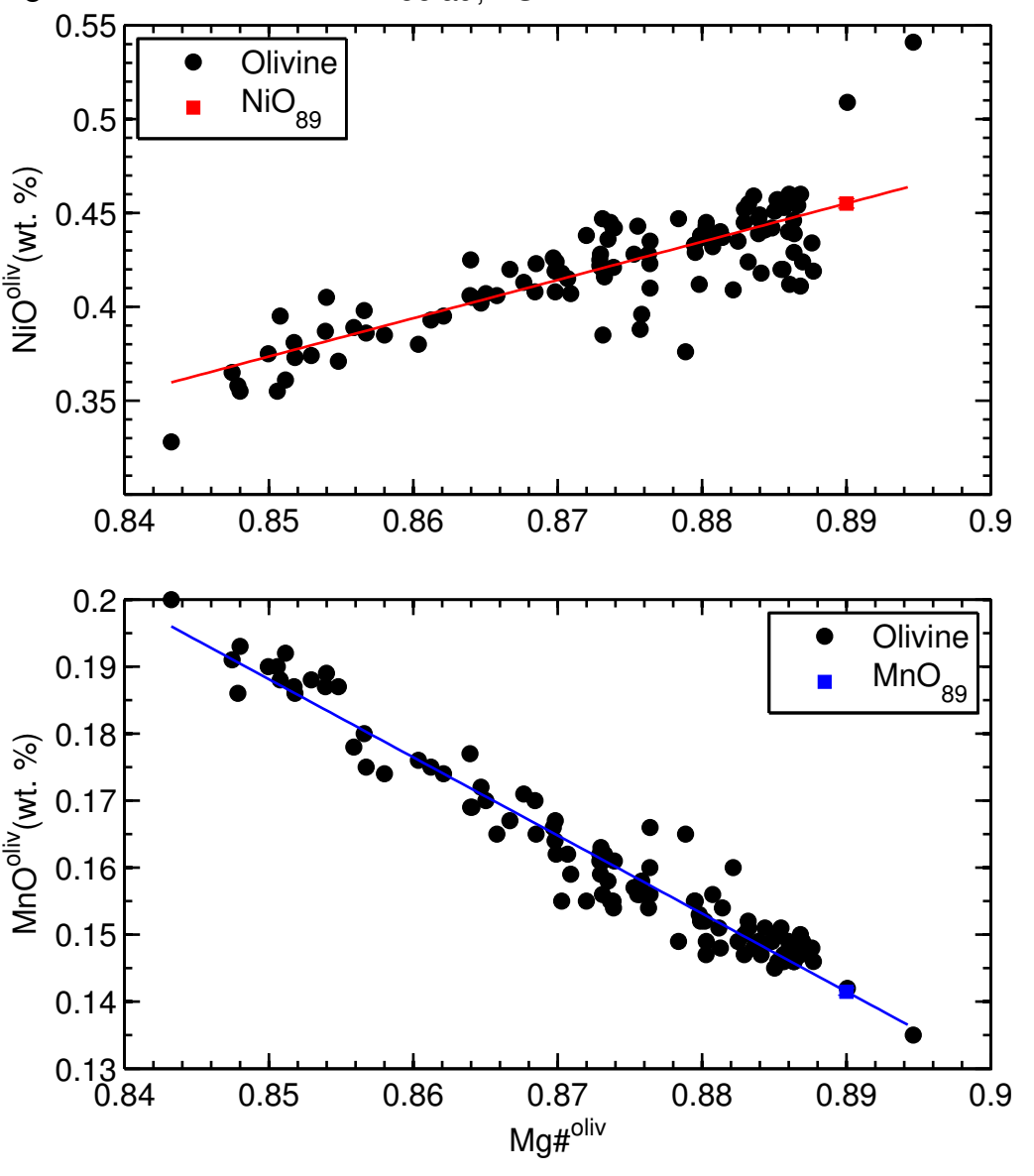
Koolau, KSDP
Olivine
NiO89
NiOoliv(wt. %)
0.55
0.5
0.45
0.4
0.35
0.84
0.85
0.86
0.87
0.88
0.89
0.9
Olivine
MnO89
MnOoliv(wt. %)
0.2
0.19
0.18
0.17
0.16
0.15
0.14
0.13
Mg#oliv

Figure S27

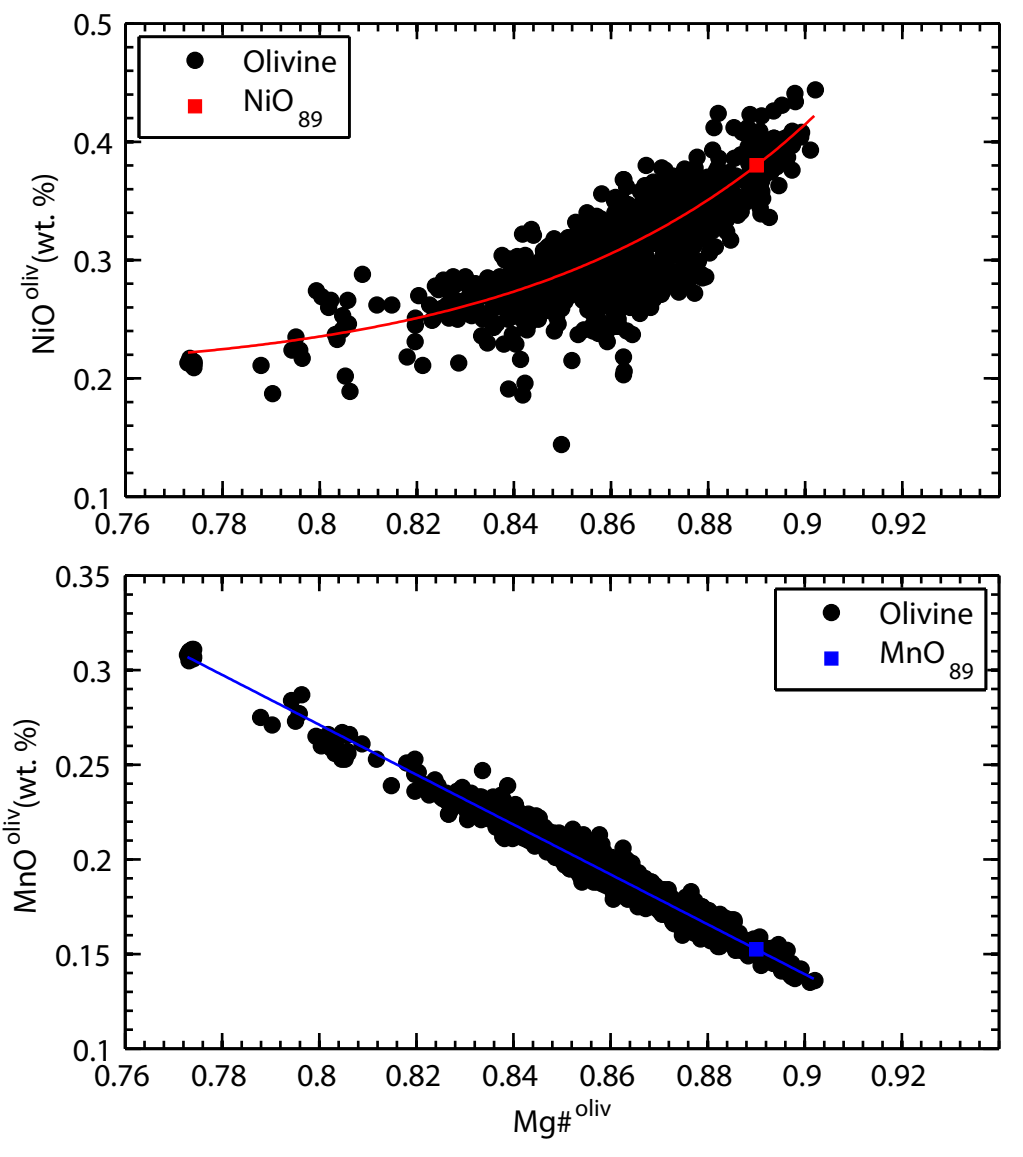
Loihi Seamount
Olivine
NiO 89
NiO oliv (wt. %)
0.5
0.4
0.3
0.2
0.1
0.76
0.78
0.8
0.82
0.84
0.86
0.88
0.9
0.92
Olivine
MnO 89
MnO oliv (wt. %)
0.35
0.3
0.25
0.2
0.15
0.1
Mg# oliv

Figure S28

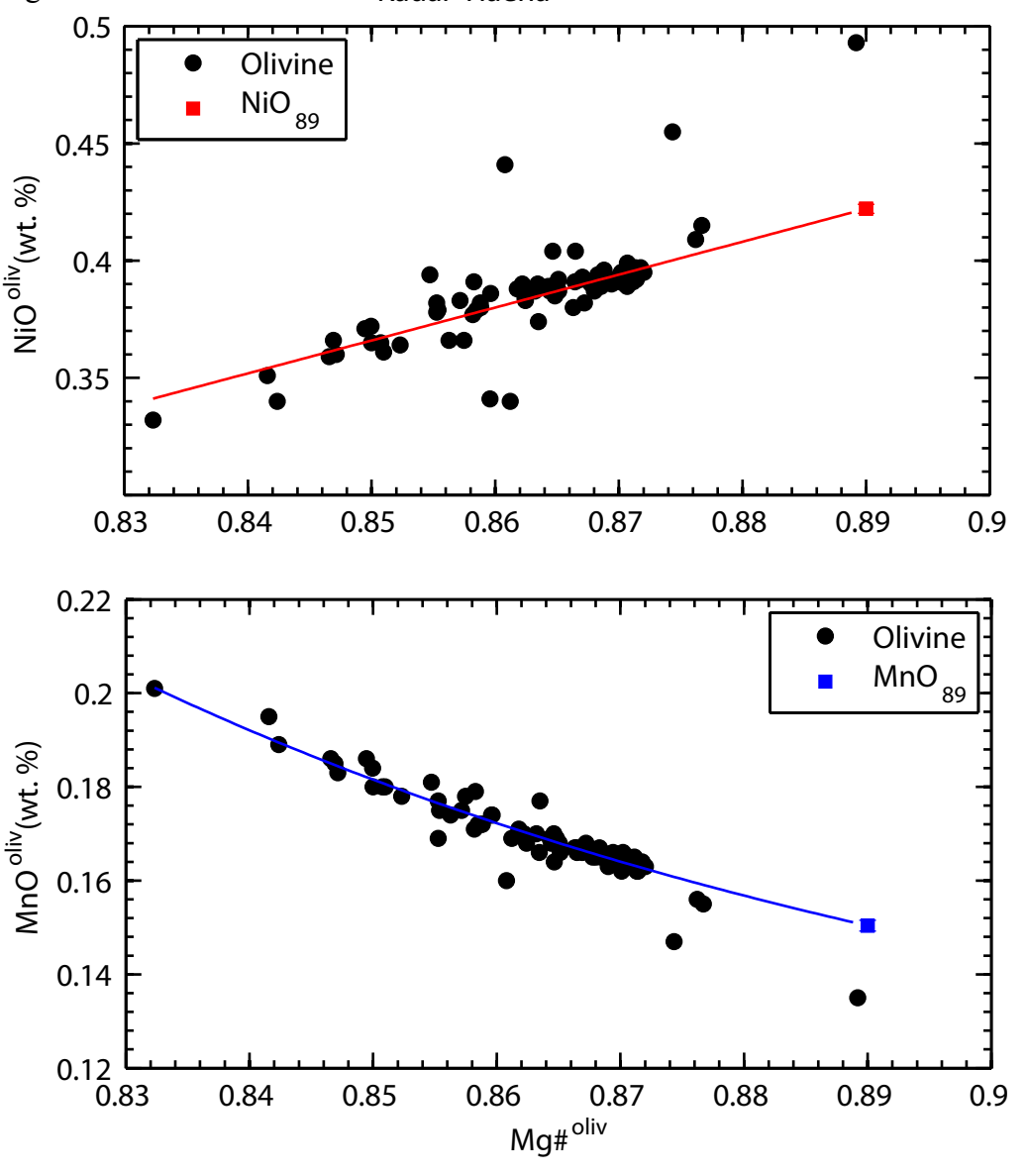
Kauai–Haena
Olivine
NiO 89
NiO oliv (wt. %)
0.5
0.45
0.4
0.35
0.83
0.84
0.85
0.86
0.87
0.88
0.89
0.9
Olivine
MnO 89
MnO oliv (wt. %)
0.22
0.2
0.18
0.16
0.14
0.12
Mg# oliv

Figure S29

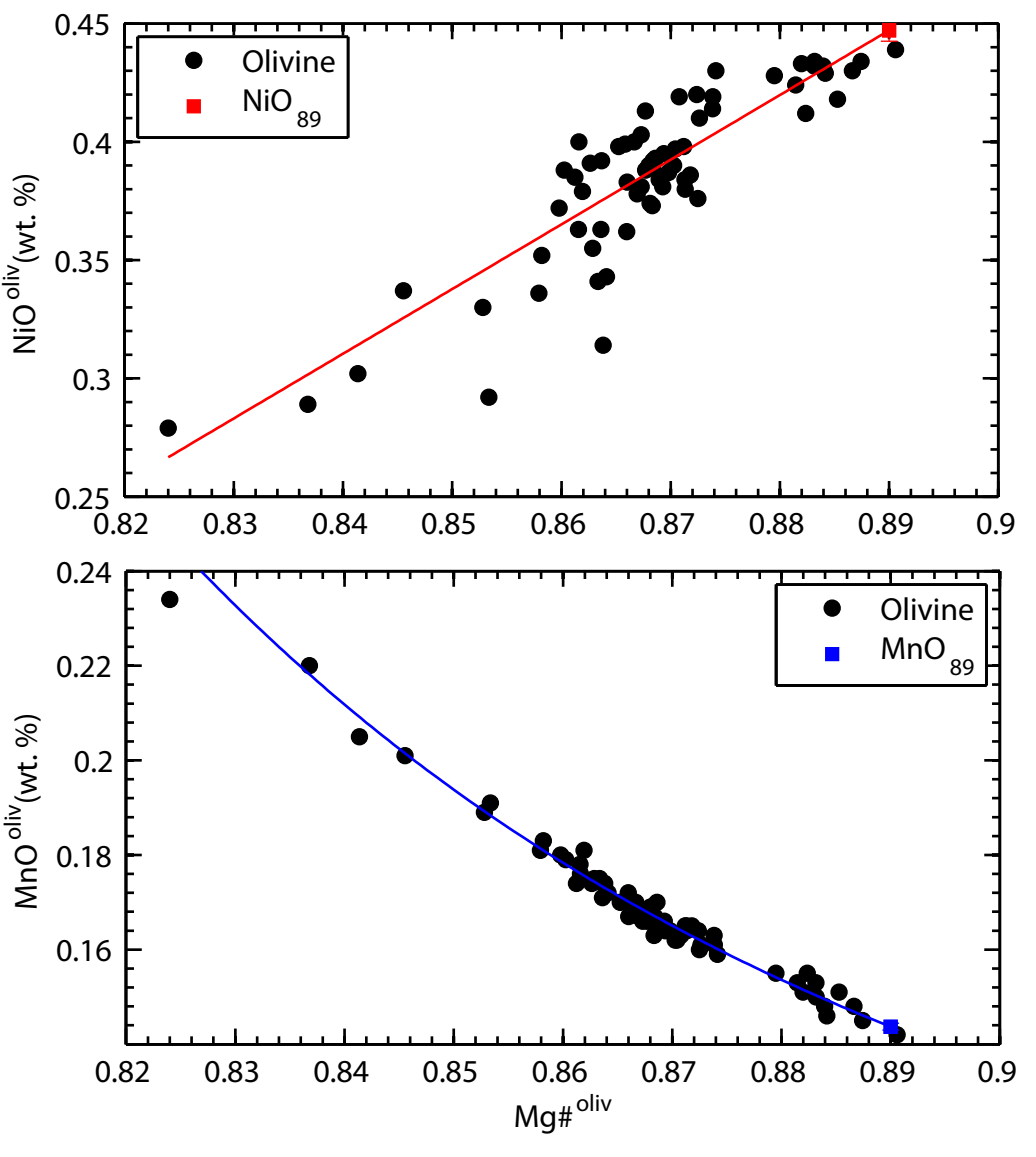
Suiko Seamount
Olivine
NiO 89
NiO oliv (wt. %)
0.45
0.4
0.35
0.3
0.25
0.82
0.83
0.84
0.85
0.86
0.87
0.88
0.89
0.9
Olivine
MnO 89
MnO oliv (wt. %)
0.24
0.22
0.2
0.18
0.16
Mg# oliv

Figure S30

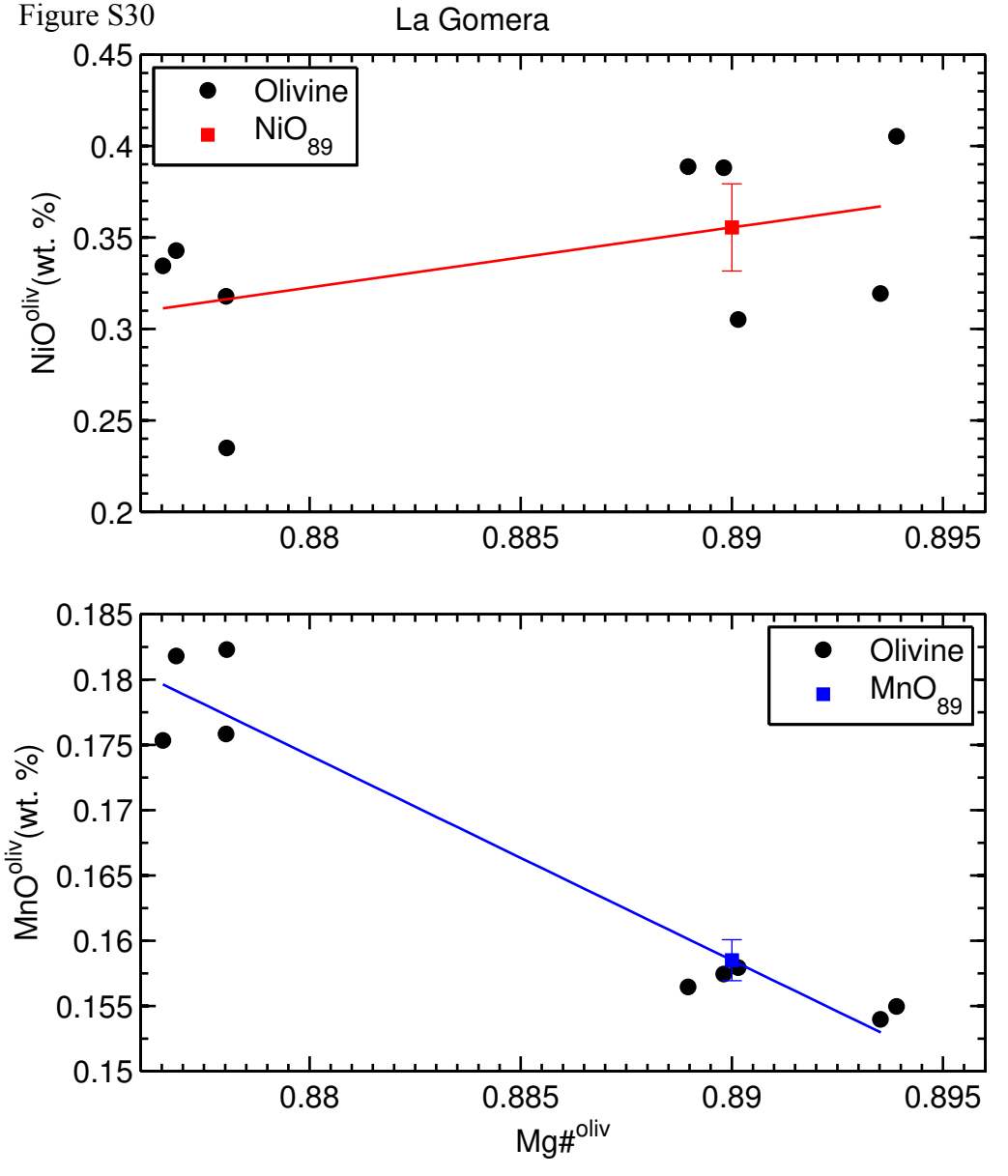
La Gomera
Olivine
NiO89
NiOoliv(wt. %)
0.45
0.4
0.35
0.3
0.25
0.2
0.88
0.885
0.89
0.895
Olivine
MnO89
MnOoliv(wt. %)
0.185
0.18
0.175
0.17
0.165
0.16
0.155
0.15
0.88
0.885
0.89
0.895
Mg#oliv

Figure S31

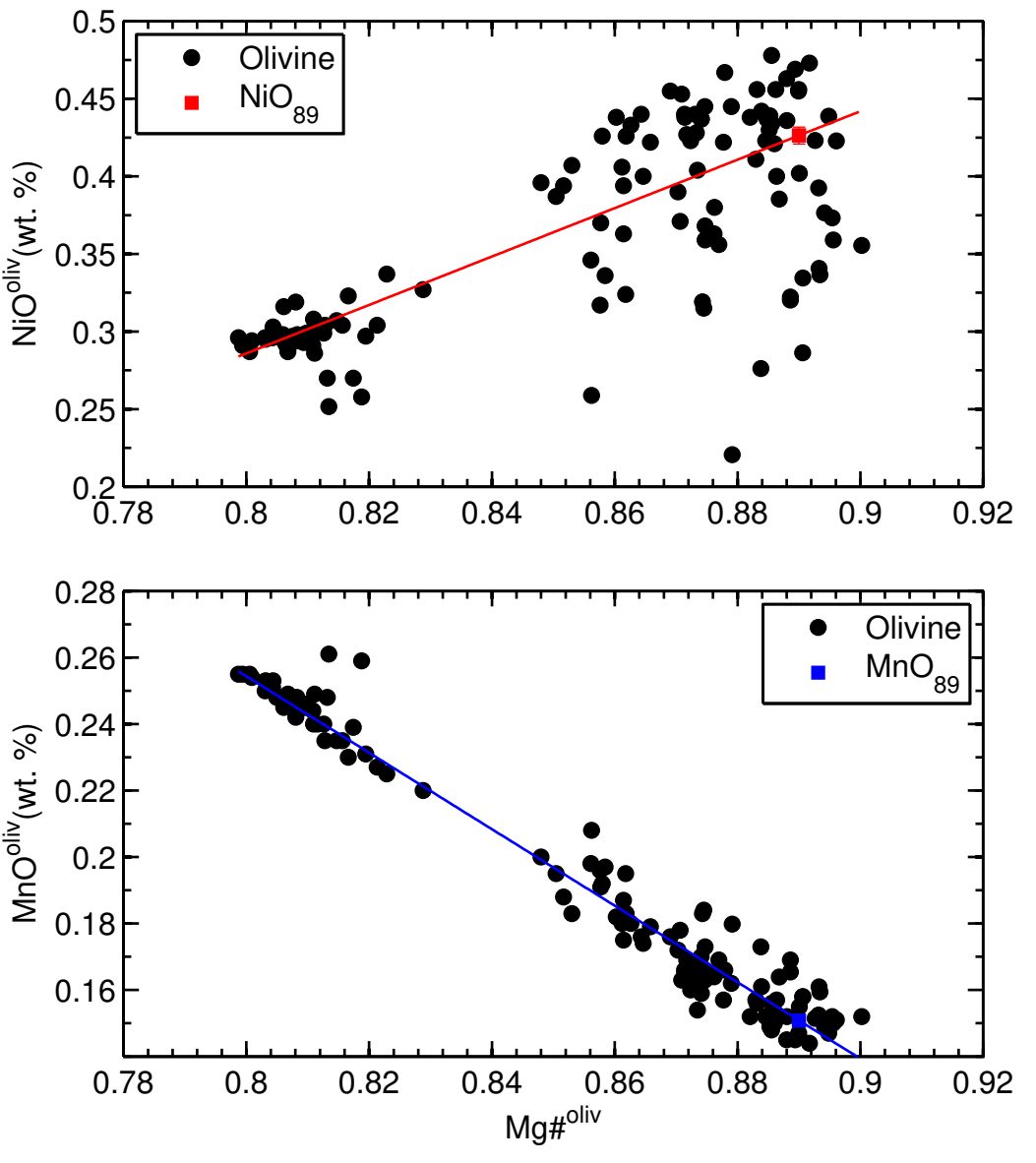
Gran Canaria
Olivine
NiO89
NiOoliv(wt. %)
0.5
0.45
0.4
0.35
0.3
0.25
0.2
0.78
0.8
0.82
0.84
0.86
0.88
0.9
0.92
Olivine
MnO89
MnOoliv(wt. %)
0.28
0.26
0.24
0.22
0.2
0.18
0.16
0.78
0.8
0.82
0.84
0.86
0.88
0.9
0.92
Mg#oliv

Figure S32

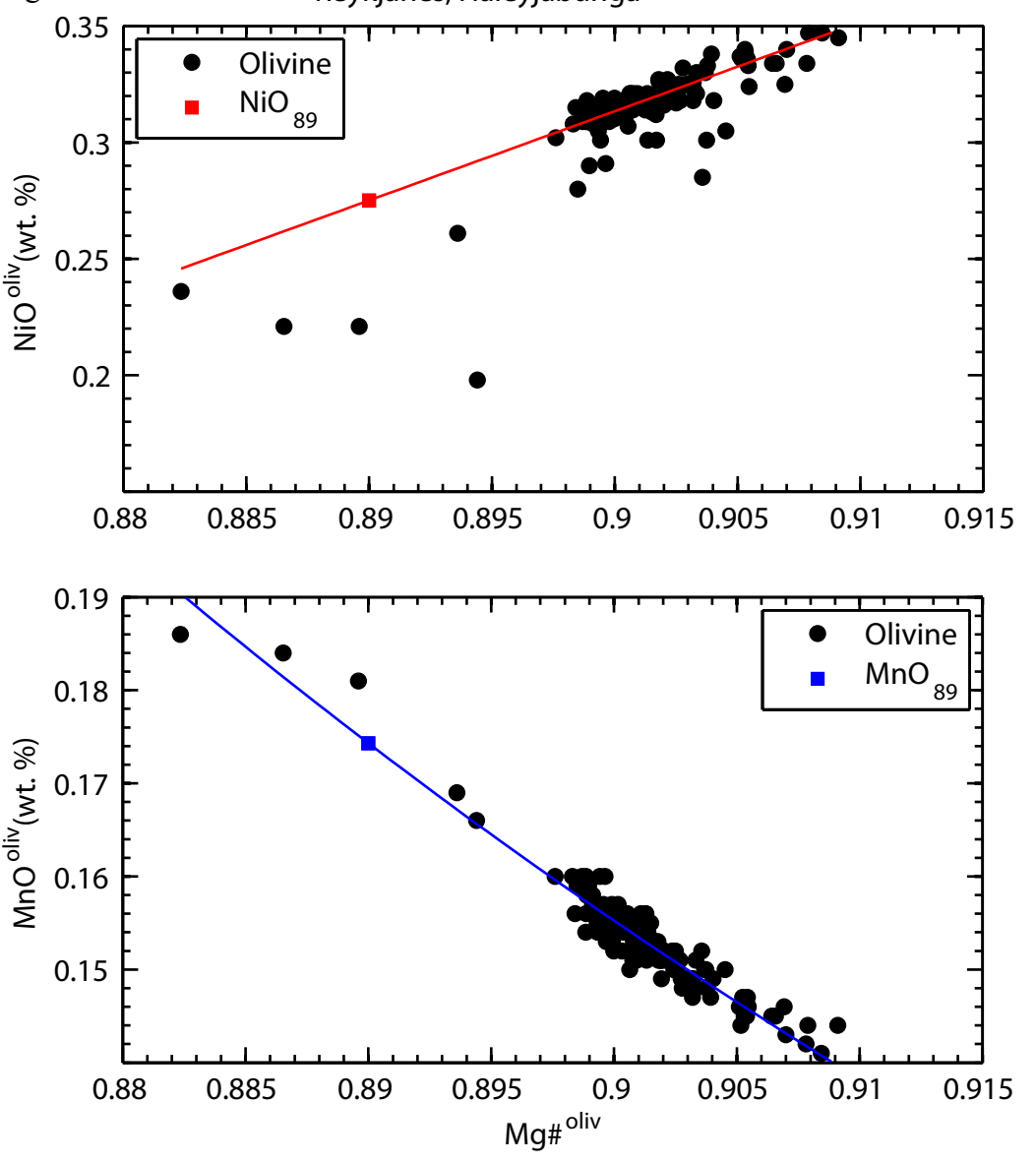
Reykjanes, Haleyjabunga
Olivine
NiO 89
NiO oliv (wt. %)
0.35
0.3
0.25
0.2
0.88
0.885
0.89
0.895
0.9
0.905
0.91
0.915
Olivine
MnO 89
MnO oliv (wt. %)
0.19
0.18
0.17
0.16
0.15
Mg# oliv

Figure S33

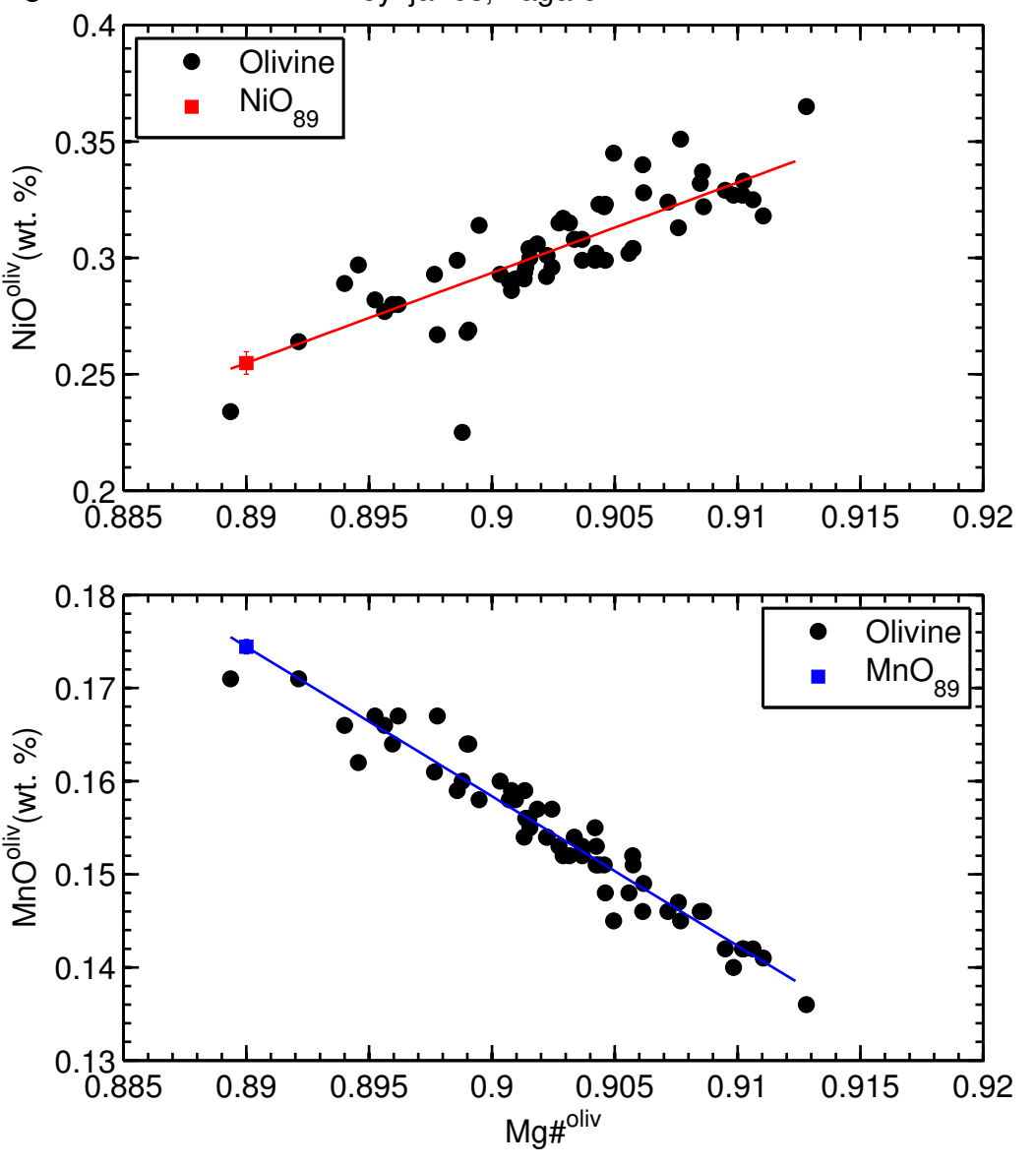
Reykjanes, Lagafell
Olivine
NiO89
NiOoliv(wt. %)
0.4
0.35
0.3
0.25
0.2
0.885
0.89
0.895
0.9
0.905
0.91
0.915
0.92
Olivine
MnO89
MnOoliv(wt. %)
0.18
0.17
0.16
0.15
0.14
0.13
Mg#oliv

Figure S34

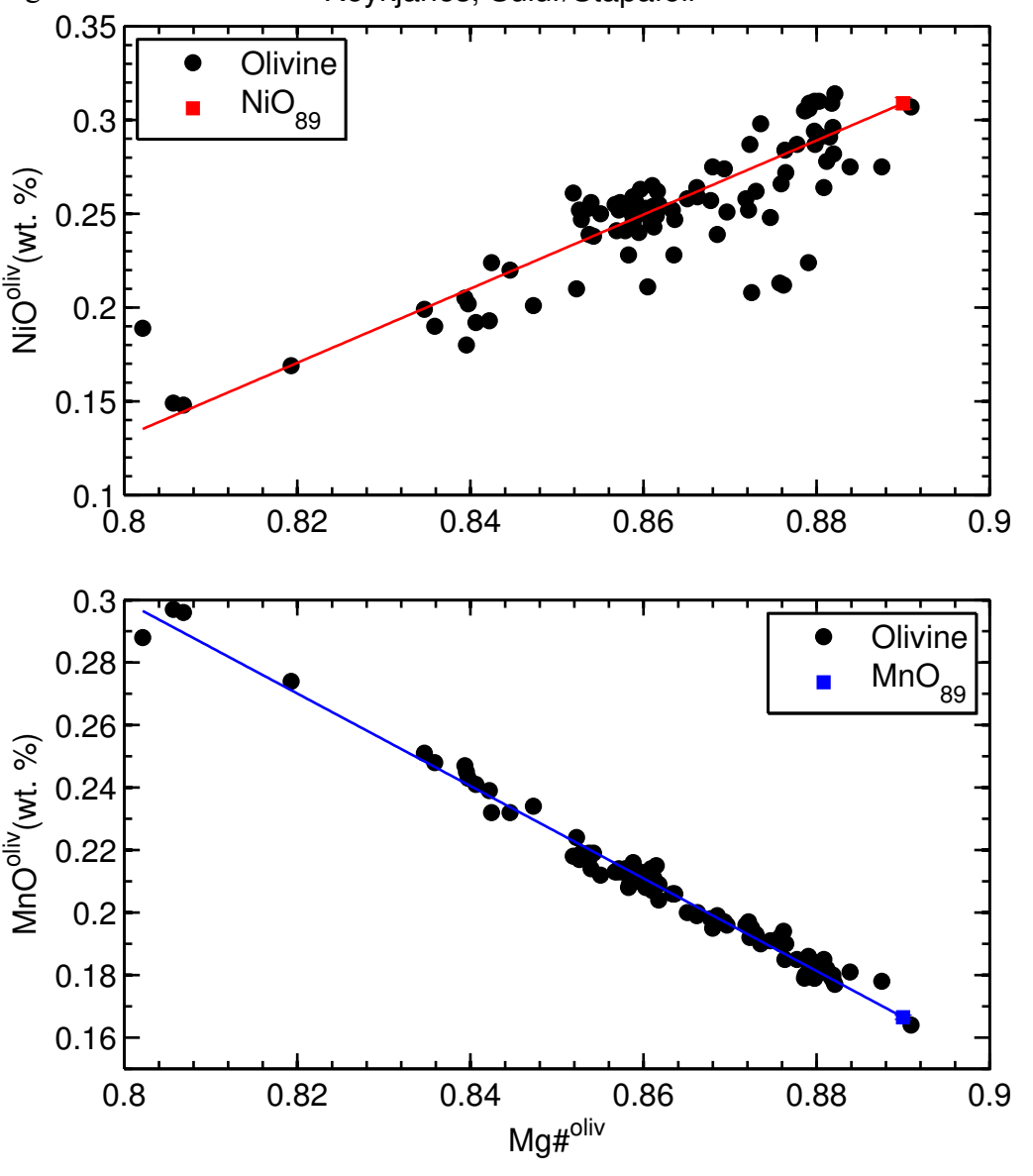
Reykjanes, Sulur/Stapafell
Olivine
NiO89
NiOoliv(wt. %)
0.35
0.3
0.25
0.2
0.15
0.1
0.8
0.82
0.84
0.86
0.88
0.9
Olivine
MnO89
MnOoliv(wt. %)
0.3
0.28
0.26
0.24
0.22
0.2
0.18
0.16
0.8
0.82
0.84
0.86
0.88
0.9
Mg#oliv

Figure S35

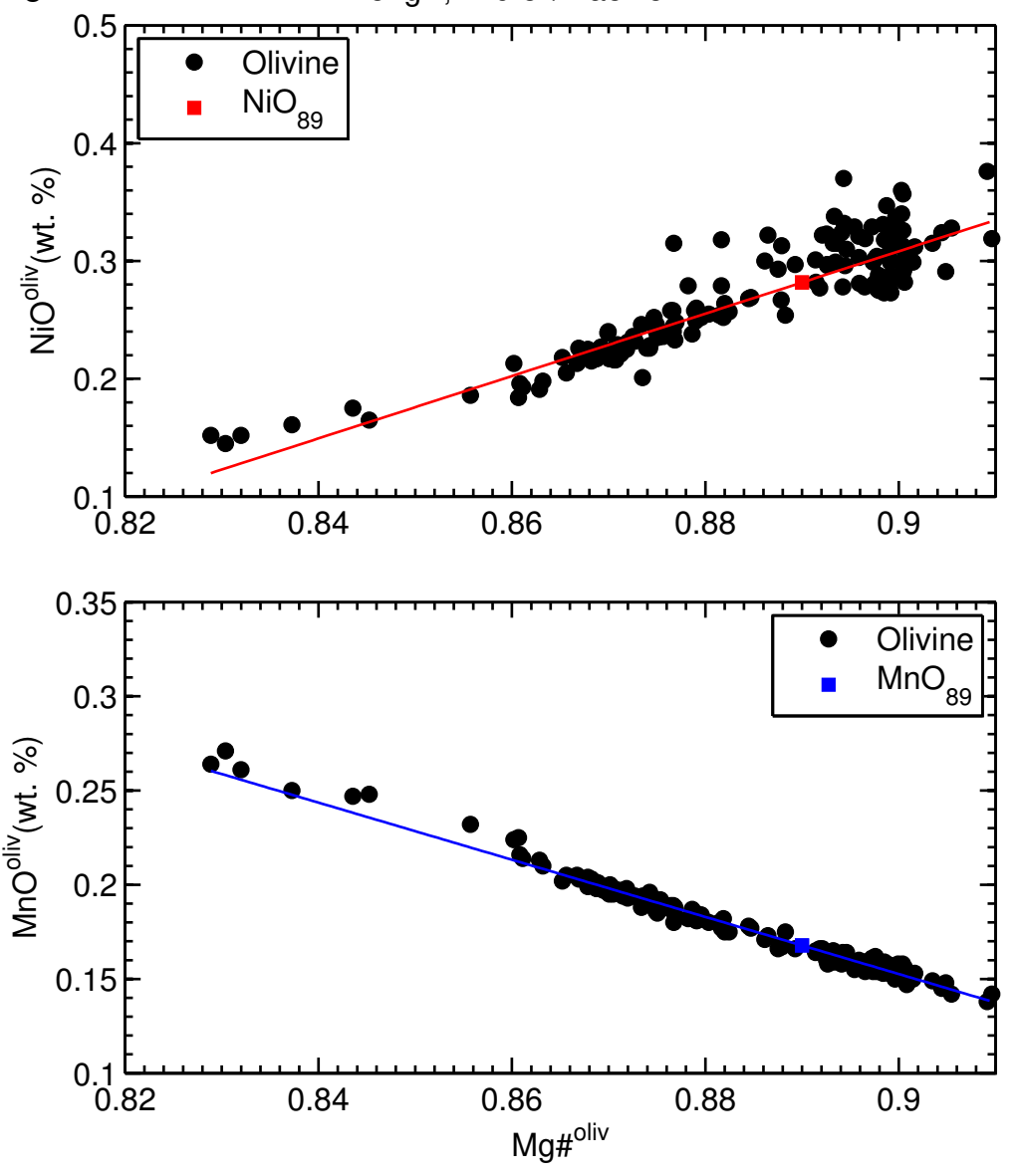
Hengill, Midfell/Maelifell
Olivine
NiO89
NiOoliv(wt. %)
0.5
0.4
0.3
0.2
0.1
0.82
0.84
0.86
0.88
0.9
Olivine
MnO89
MnOoliv(wt. %)
0.35
0.3
0.25
0.2
0.15
0.1
0.82
0.84
0.86
0.88
0.9
Mg#oliv

Figure S36

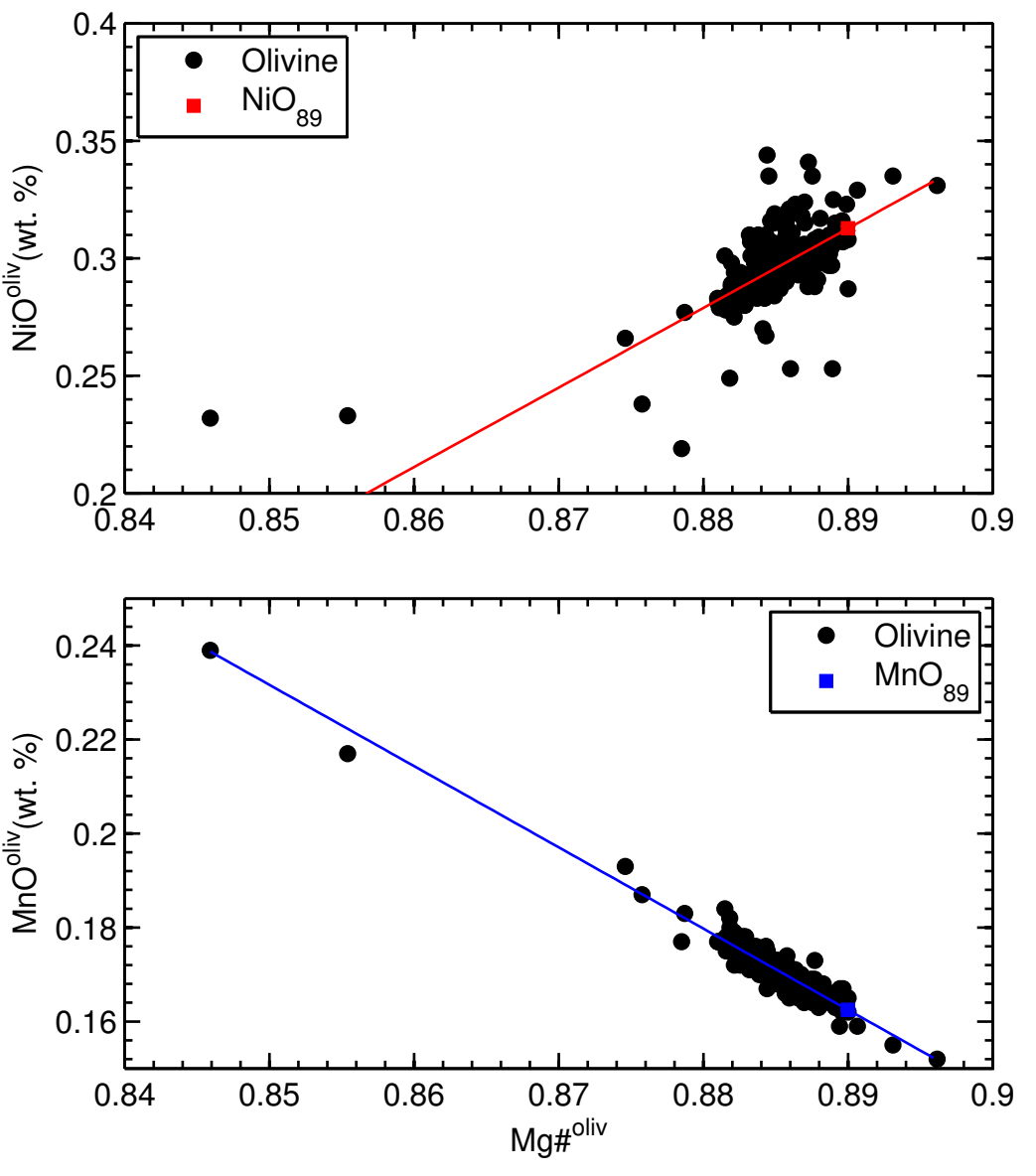
Kistufell
Olivine
NiO89
NiOoliv(wt. %)
0.4
0.35
0.3
0.25
0.2
0.84
0.85
0.86
0.87
0.88
0.89
0.9
Olivine
MnO89
MnOoliv(wt. %)
0.24
0.22
0.2
0.18
0.16
Mg#oliv

Figure S37

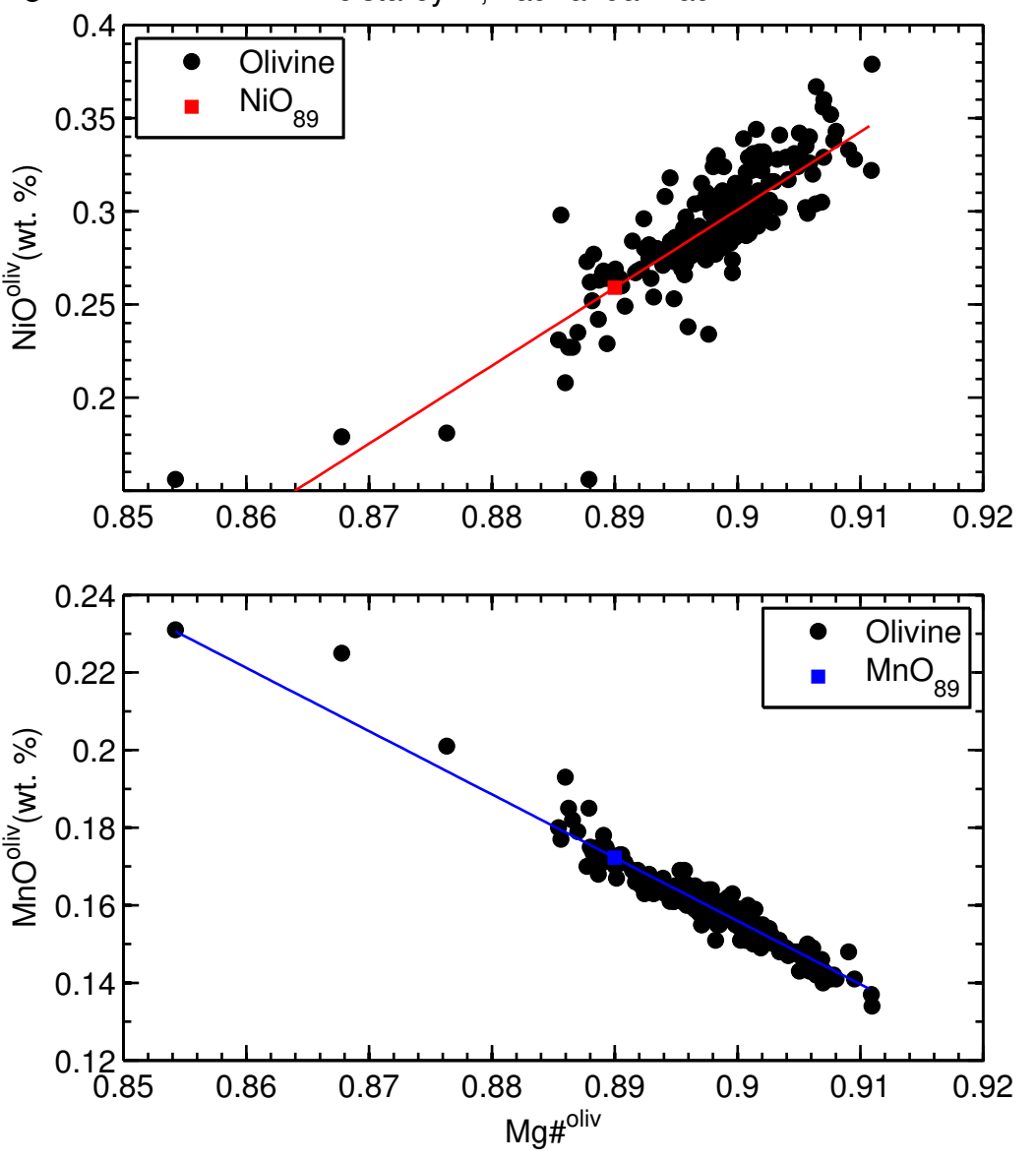
Theistareykir, Laufrandarhraun–1
Olivine
NiO89
NiOoliv(wt. %)
0.4
0.35
0.3
0.25
0.2
0.85
0.86
0.87
0.88
0.89
0.9
0.91
0.92
Olivine
MnO89
MnOoliv(wt. %)
0.24
0.22
0.2
0.18
0.16
0.14
0.12
Mg#oliv

Figure S38

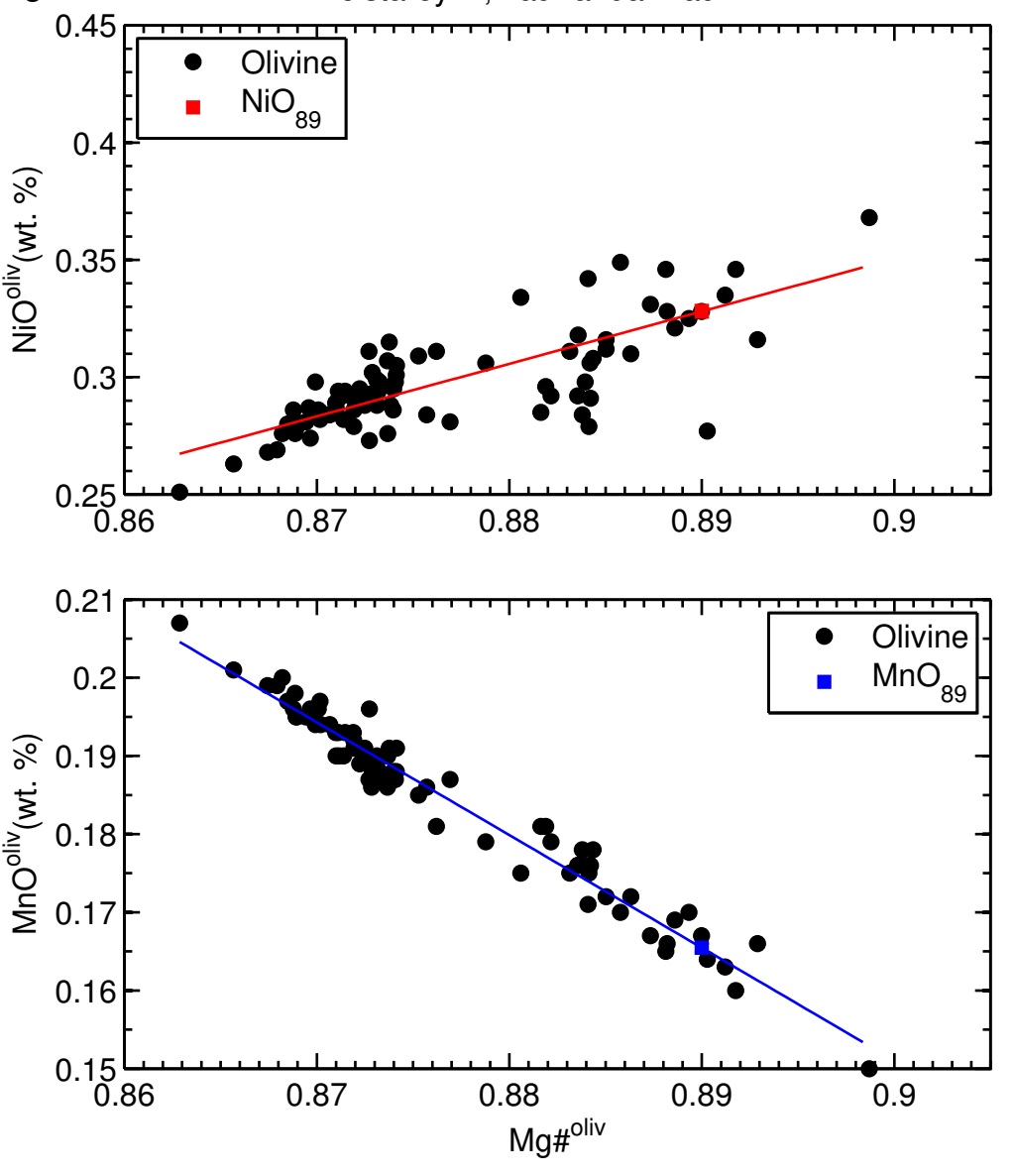
Theistareykir, Laufrandarhraun–2
Olivine
NiO89
NiOoliv(wt. %)
0.45
0.4
0.35
0.3
0.25
0.86
0.87
0.88
0.89
0.9
Olivine
MnO89
MnOoliv(wt. %)
0.21
0.2
0.19
0.18
0.17
0.16
0.15
Mg#oliv

Figure S39

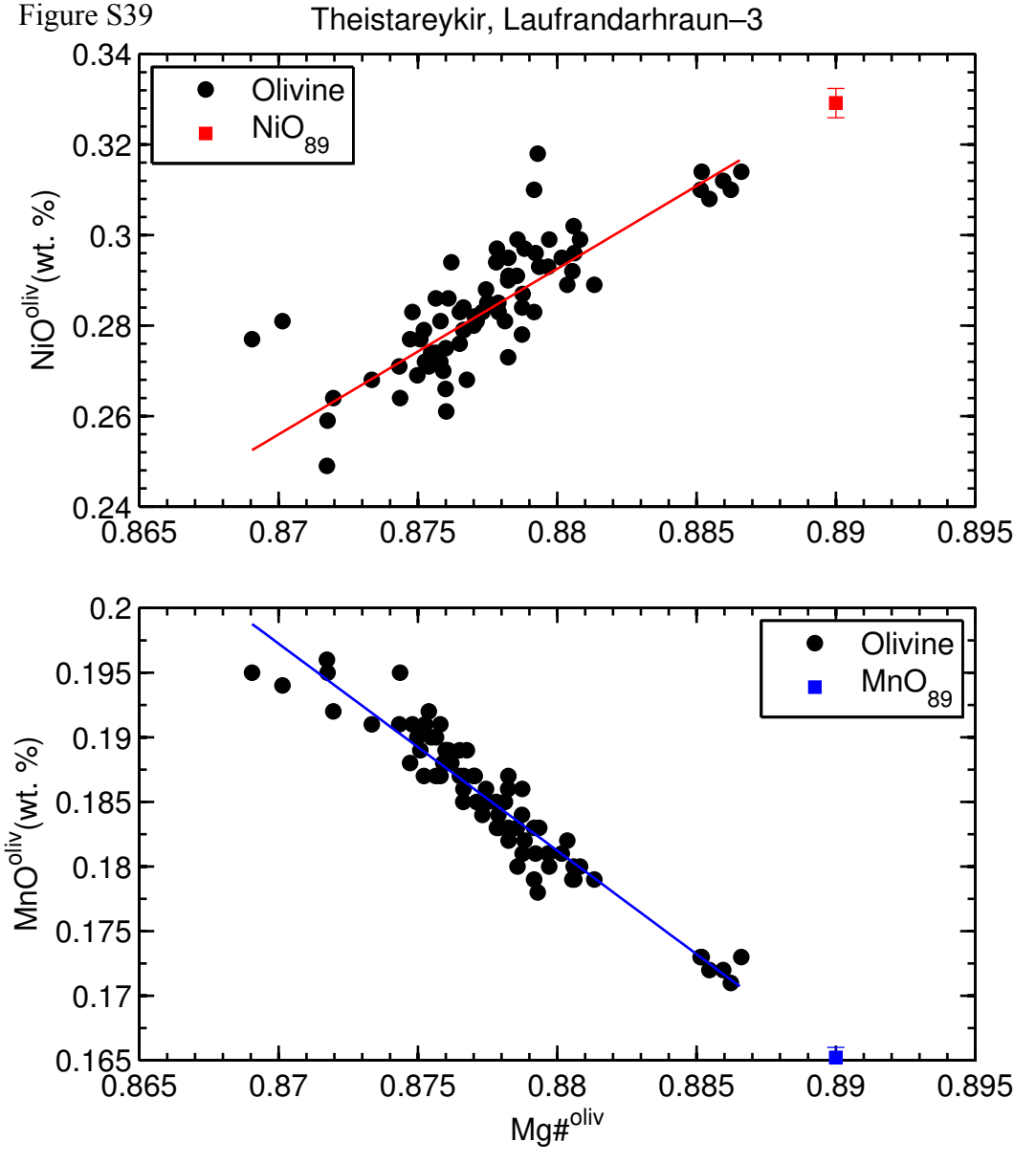
Theistareykir, Laufrandarhraun–3
Olivine
NiO89
NiOoliv(wt. %)
0.34
0.32
0.3
0.28
0.26
0.24
0.865
0.87
0.875
0.88
0.885
0.89
0.895
Olivine
MnO89
MnOoliv(wt. %)
0.2
0.195
0.19
0.185
0.18
0.175
0.17
0.165
Mg#oliv

Figure S40

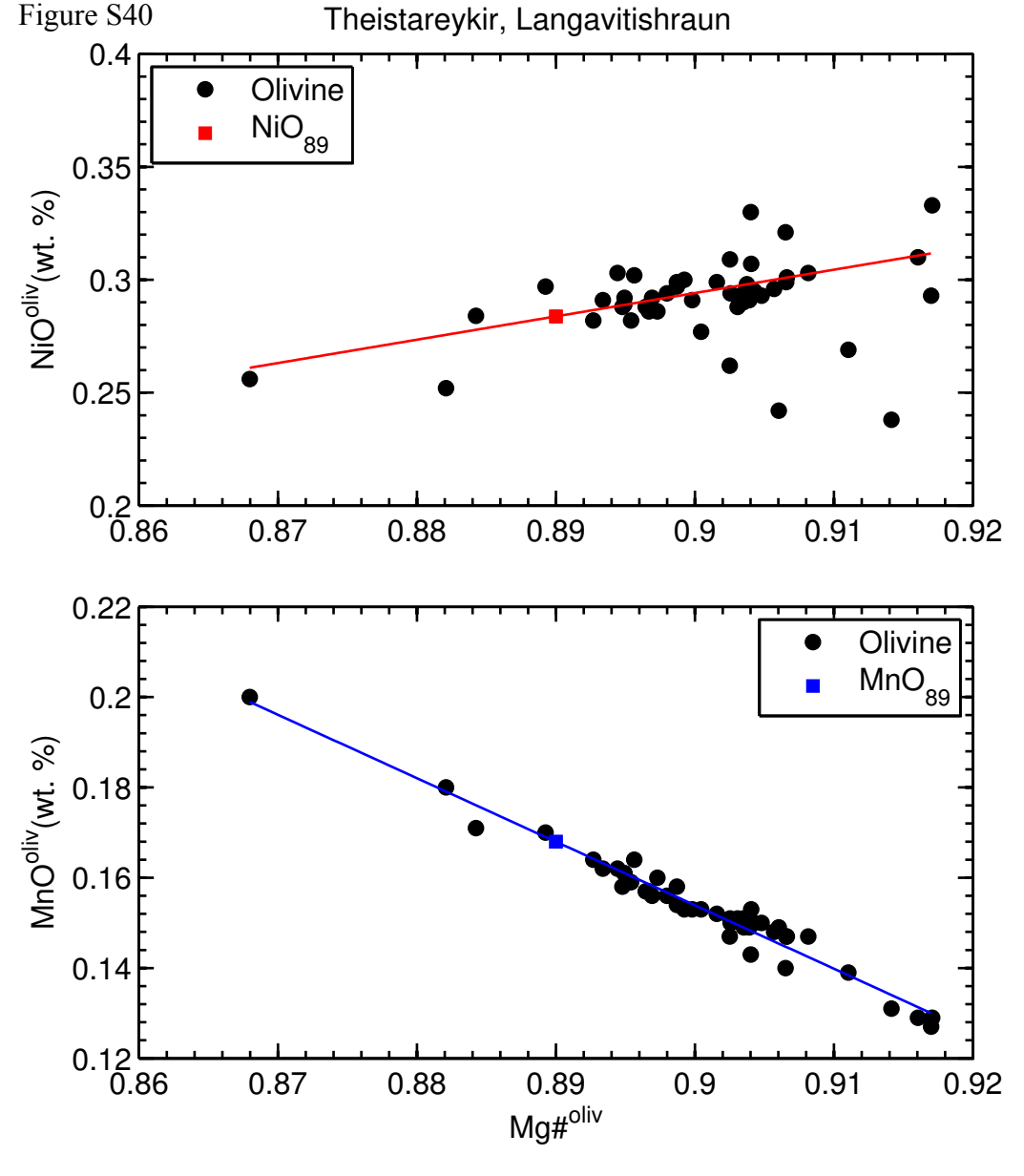
Theistareykir, Langavitishraun
Olivine
NiO89
NiOoliv(wt. %)
0.4
0.35
0.3
0.25
0.2
0.86
0.87
0.88
0.89
0.9
0.91
0.92
Olivine
MnO89
MnOoliv(wt. %)
0.22
0.2
0.18
0.16
0.14
0.12
Mg#oliv

Figure S41

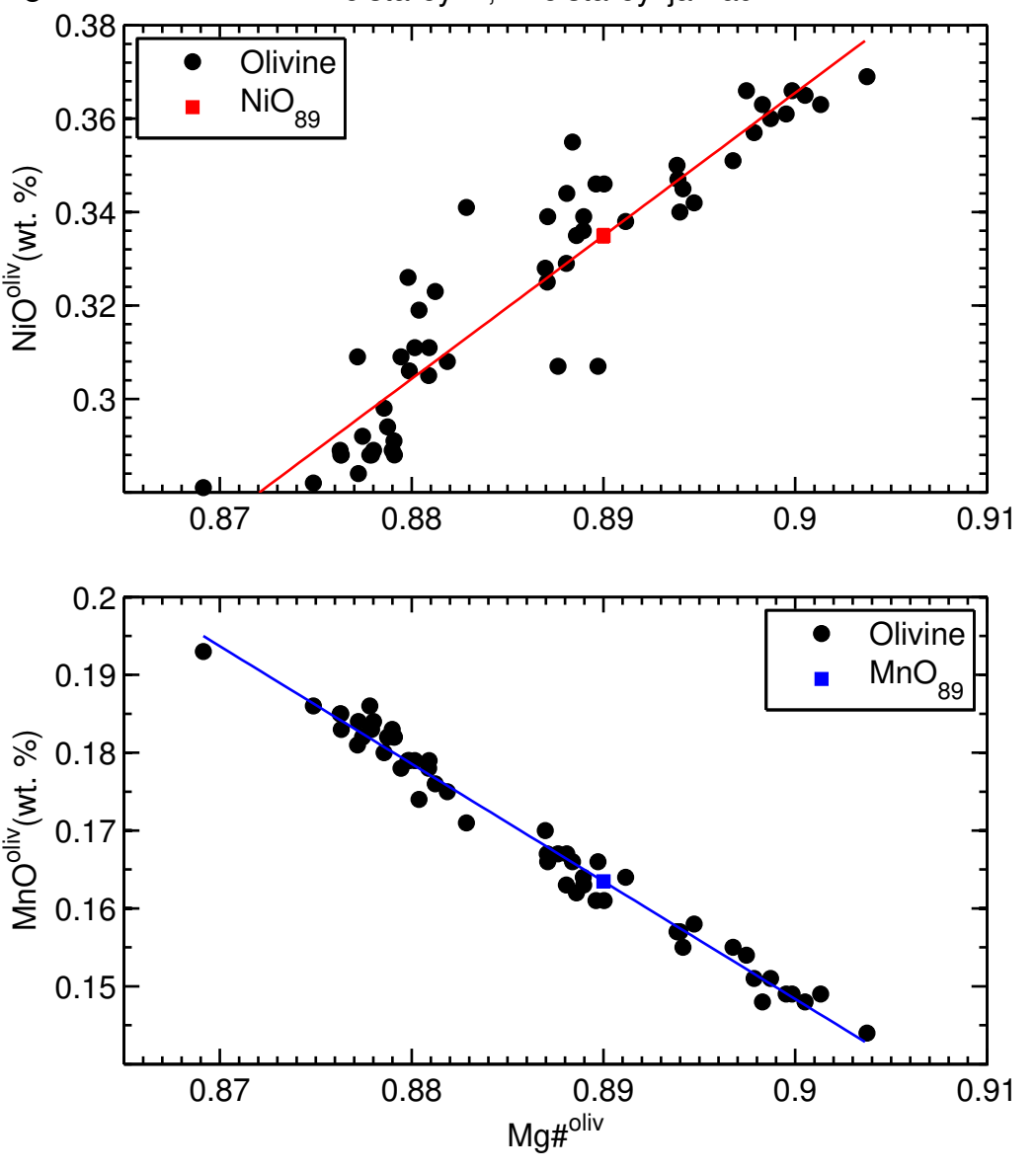
Theistareykir, Theistareykjahraun
Olivine
NiO89
NiOoliv(wt. %)
0.38
0.36
0.34
0.32
0.3
0.87
0.88
0.89
0.9
0.91
Olivine
MnO89
MnOoliv(wt. %)
0.2
0.19
0.18
0.17
0.16
0.15
0.87
0.88
0.89
0.9
0.91
Mg#oliv

Figure S42

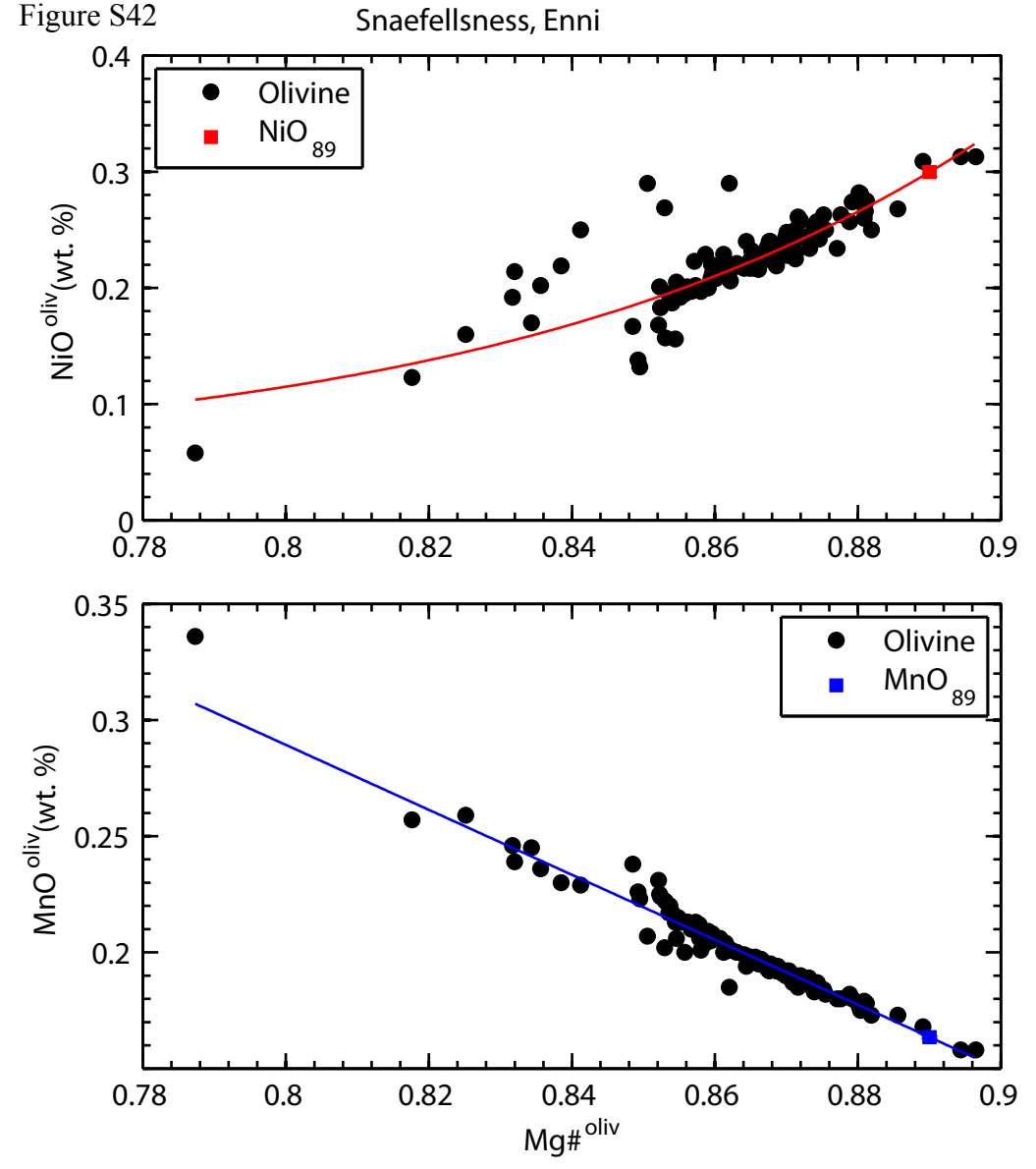
Snaefellsness, Enni
Olivine
NiO 89
NiO oliv (wt. %)
0.4
0.3
0.2
0.1
0
0.78
0.8
0.82
0.84
0.86
0.88
0.9
Olivine
MnO 89
MnO oliv (wt. %)
0.35
0.3
0.25
0.2
0.78
0.8
0.82
0.84
0.86
0.88
0.9
Mg# oliv

Figure S43

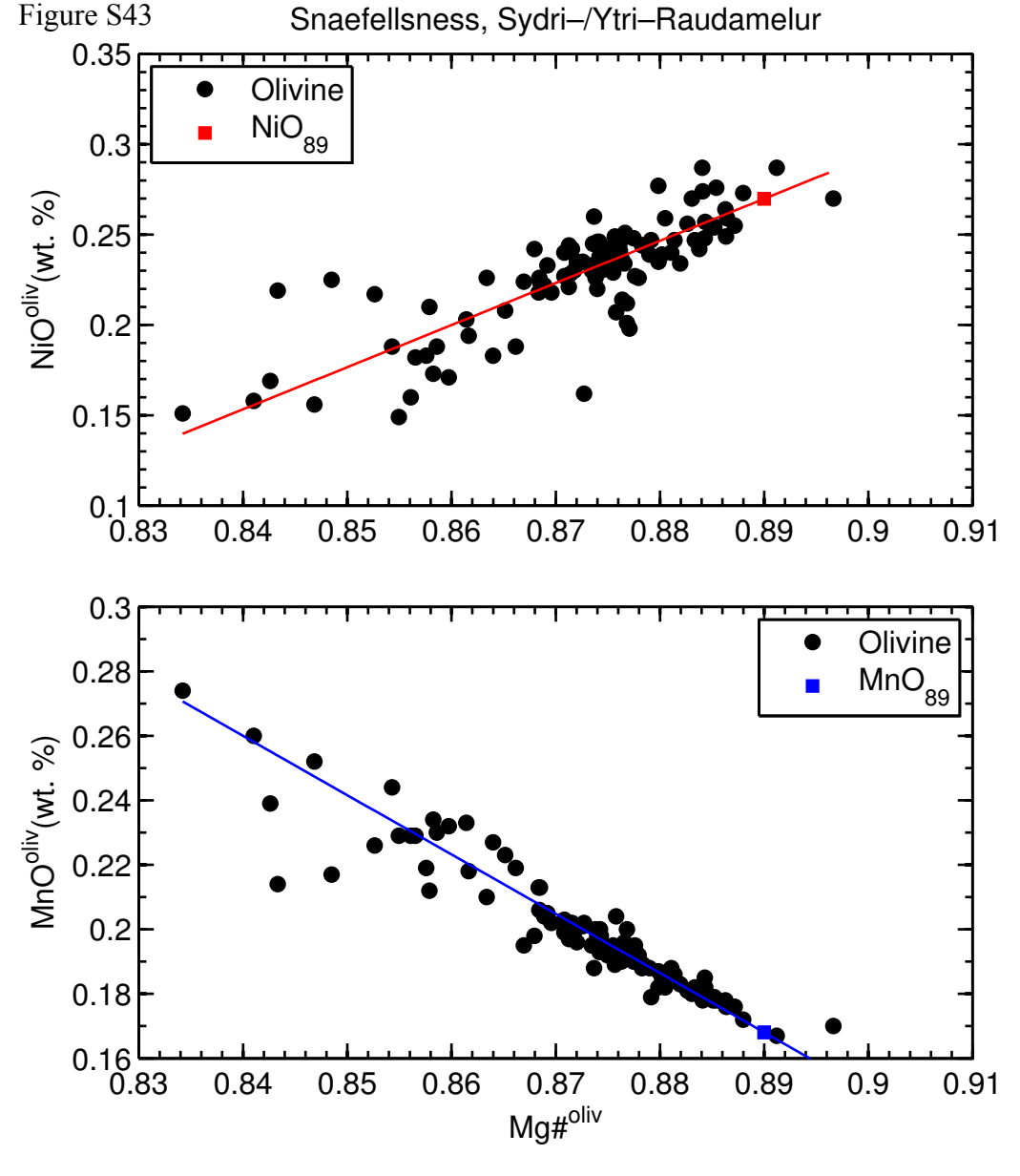
Snaefellsness, Sydri–/Ytri–Raudamelur
Olivine
NiO89
NiOoliv(wt. %)
0.35
0.3
0.25
0.2
0.15
0.1
0.83
0.84
0.85
0.86
0.87
0.88
0.89
0.9
0.91
Olivine
MnO89
MnOoliv(wt. %)
0.3
0.28
0.26
0.24
0.22
0.2
0.18
0.16
Mg#oliv

Figure S44

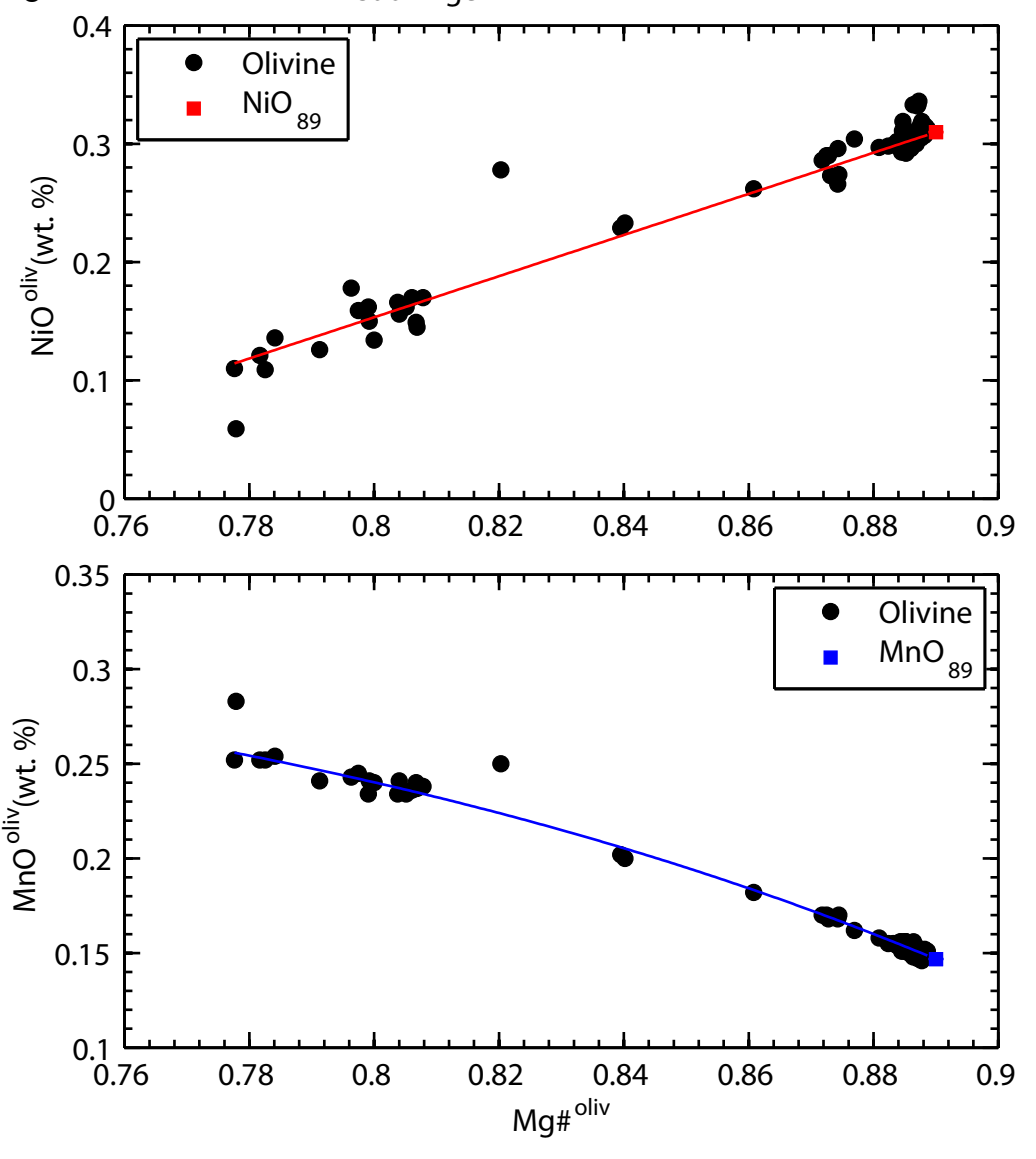
Sao Migel–1
Olivine
NiO 89
NiO oliv (wt. %)
0.4
0.3
0.2
0.1
0
0.76
0.78
0.8
0.82
0.84
0.86
0.88
0.9
Olivine
MnO 89
MnO oliv (wt. %)
0.35
0.3
0.25
0.2
0.15
0.1
Mg# oliv

Figure S45

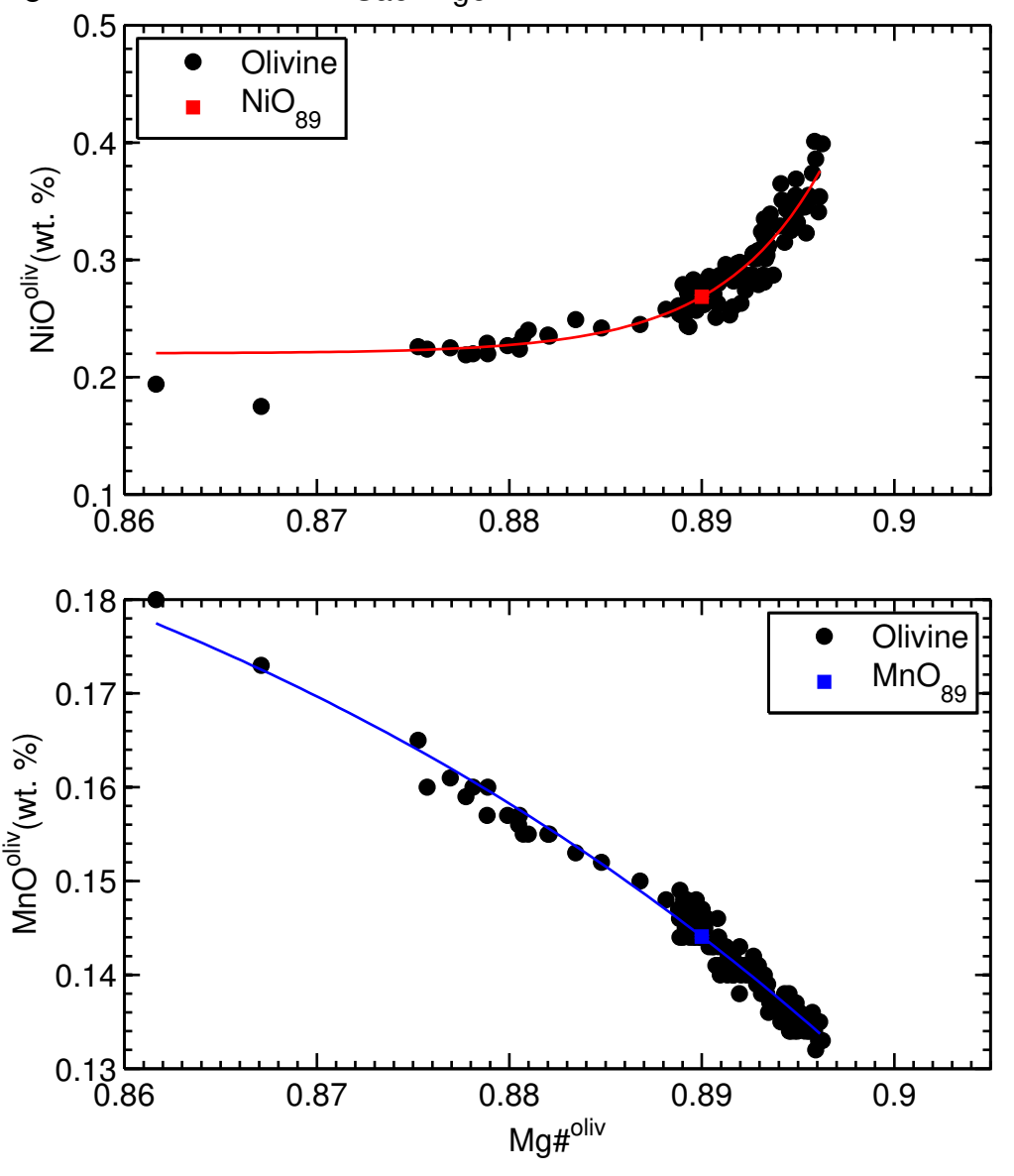
Sao Migel–2
Olivine
NiO89
NiOoliv(wt. %)
0.5
0.4
0.3
0.2
0.1
0.86
0.87
0.88
0.89
0.9
Olivine
MnO89
MnOoliv(wt. %)
0.18
0.17
0.16
0.15
0.14
0.13
Mg#oliv

Figure S46

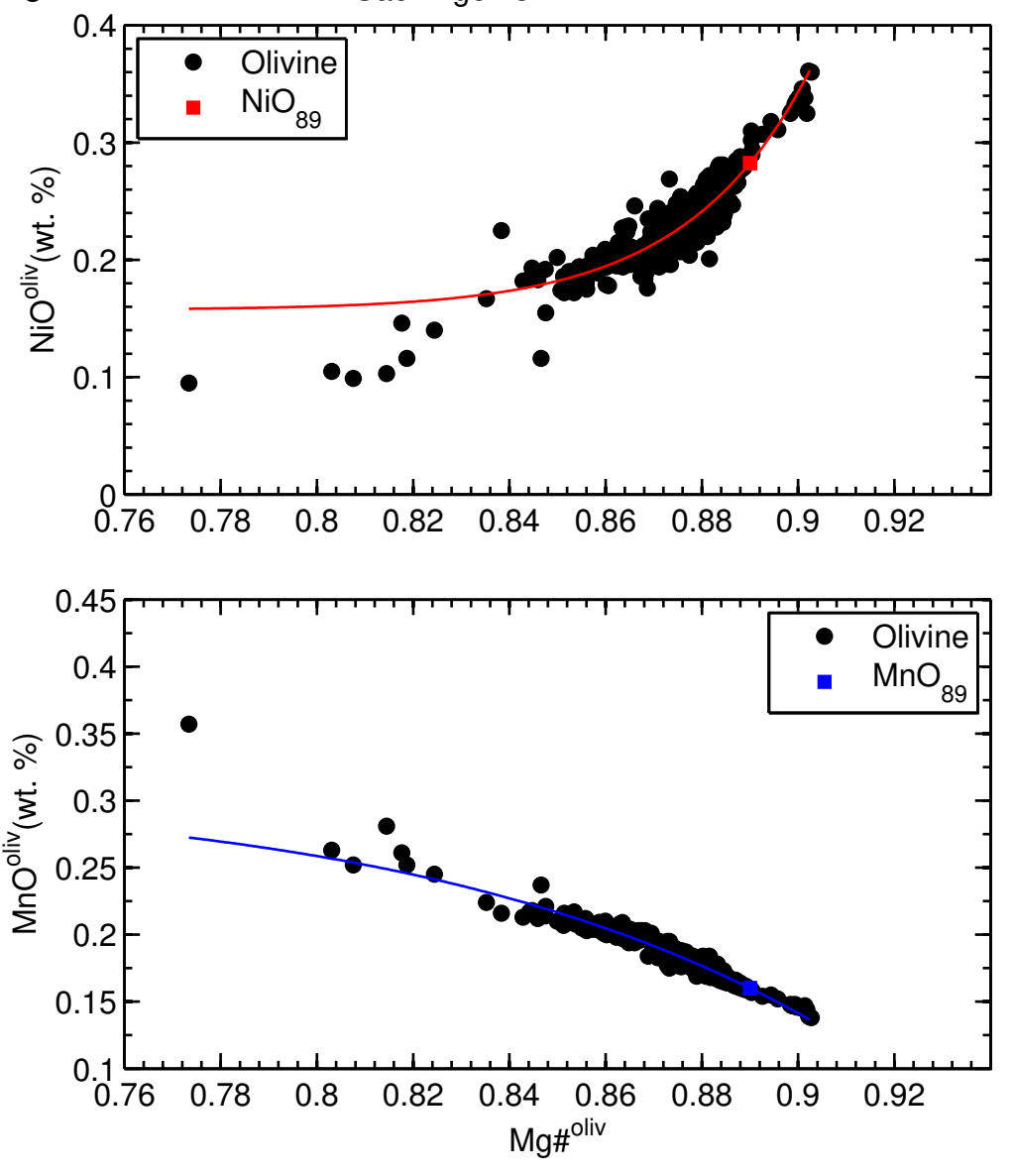
Sao Migel–3
Olivine
NiO89
NiOoliv(wt. %)
0.4
0.3
0.2
0.1
0
0.76
0.78
0.8
0.82
0.84
0.86
0.88
0.9
0.92
Olivine
MnO89
MnOoliv(wt. %)
0.45
0.4
0.35
0.3
0.25
0.2
0.15
0.1
Mg#oliv

Figure S47

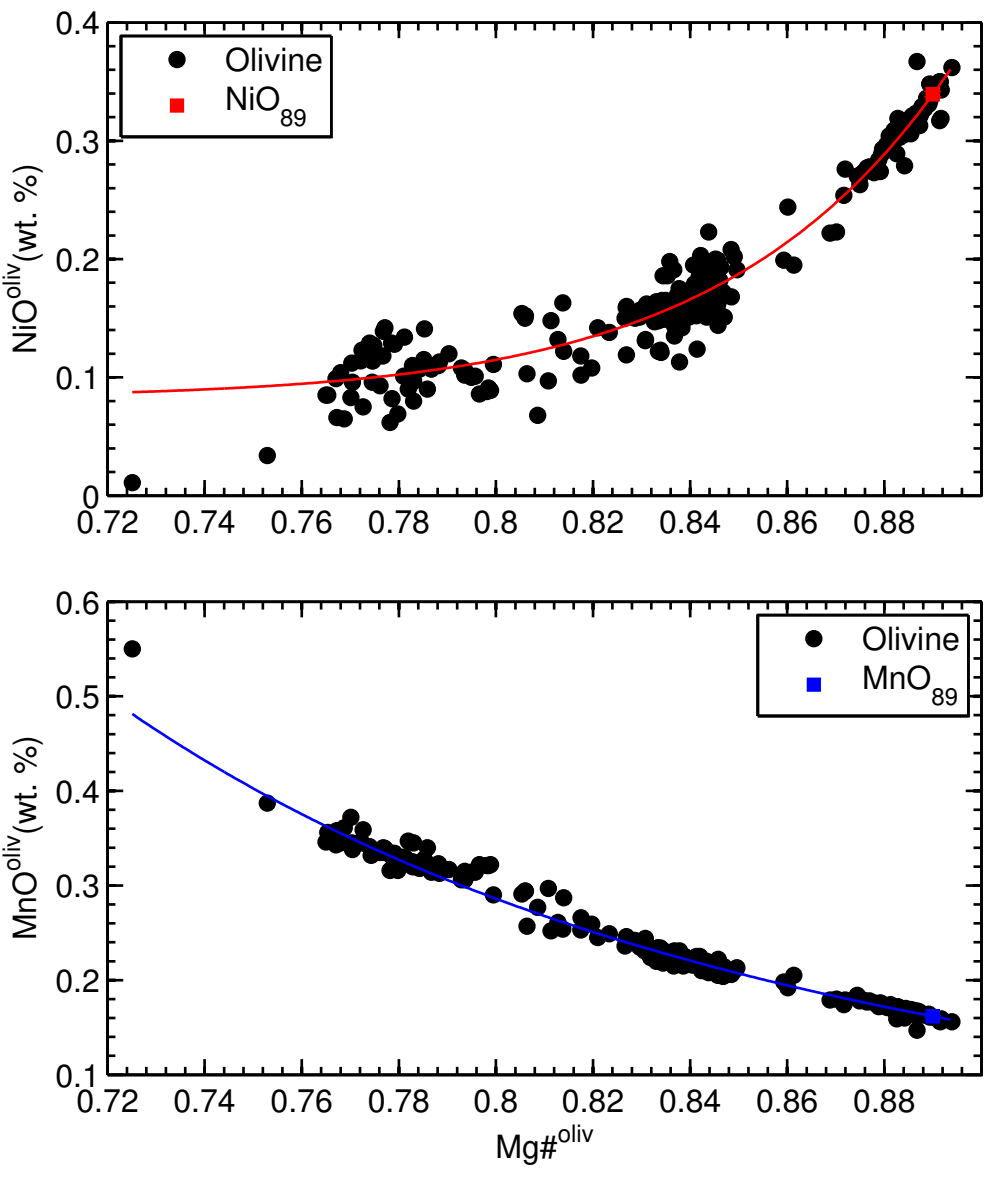
Treceria
Olivine
NiO89
NiOoliv(wt. %)
0.4
0.3
0.2
0.1
0
0.72
0.74
0.76
0.78
0.8
0.82
0.84
0.86
0.88
Olivine
MnO89
MnOoliv(wt. %)
0.6
0.5
0.4
0.3
0.2
0.1
Mg#oliv

Figure S48

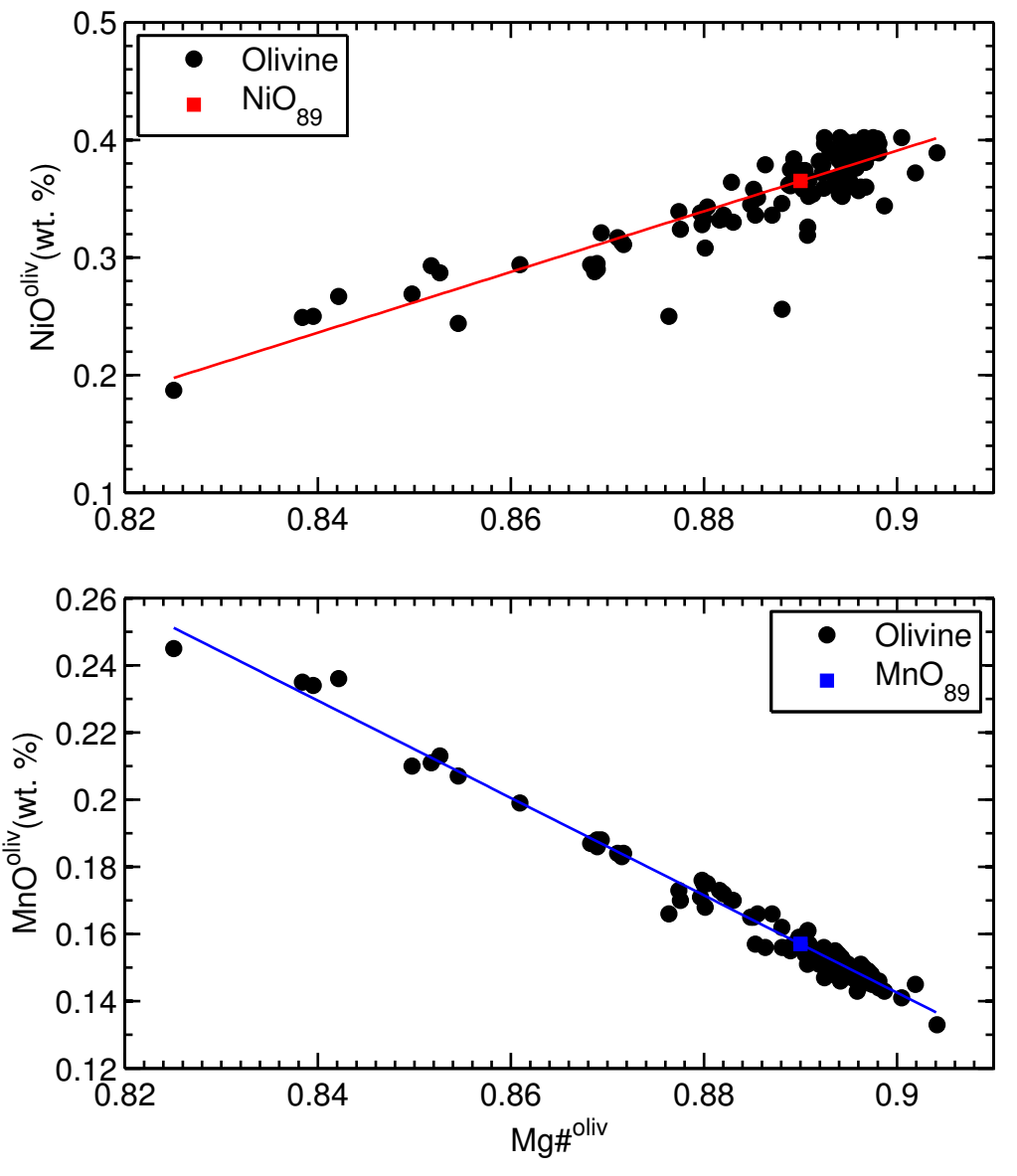
Detroit Seamount
Olivine
NiO89
NiOoliv(wt. %)
0.5
0.4
0.3
0.2
0.1
0.82
0.84
0.86
0.88
0.9
Olivine
MnO89
MnOoliv(wt. %)
0.26
0.24
0.22
0.2
0.18
0.16
0.14
0.12
0.82
0.84
0.86
0.88
0.9
Mg#oliv

Figure S49

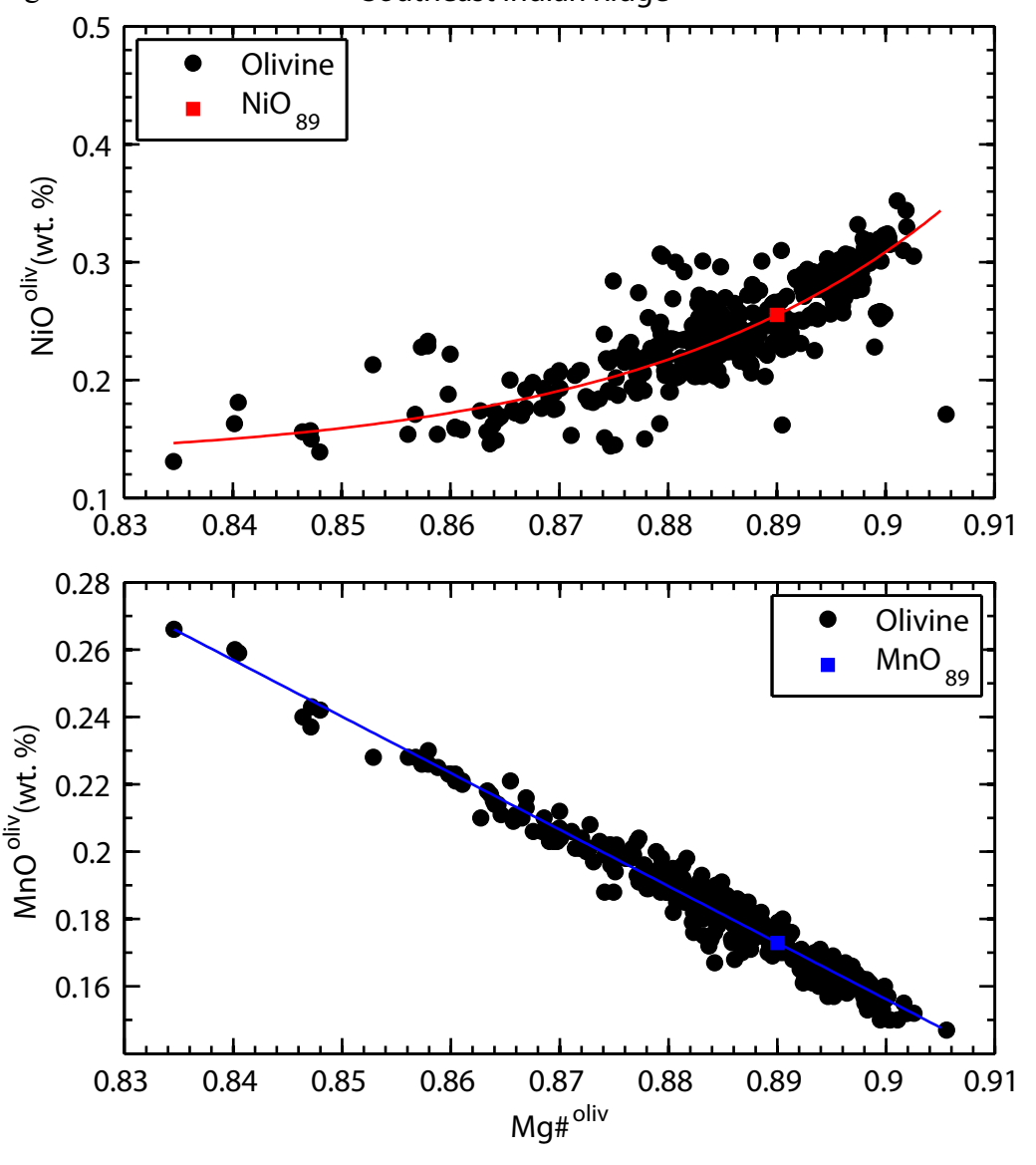
Southeast Indian Ridge
Olivine
NiO 89
NiO oliv (wt. %)
0.5
0.4
0.3
0.2
0.1
0.83
0.84
0.85
0.86
0.87
0.88
0.89
0.9
0.91
Olivine
MnO 89
MnO oliv (wt. %)
0.28
0.26
0.24
0.22
0.2
0.18
0.16
Mg# oliv

Figure S50

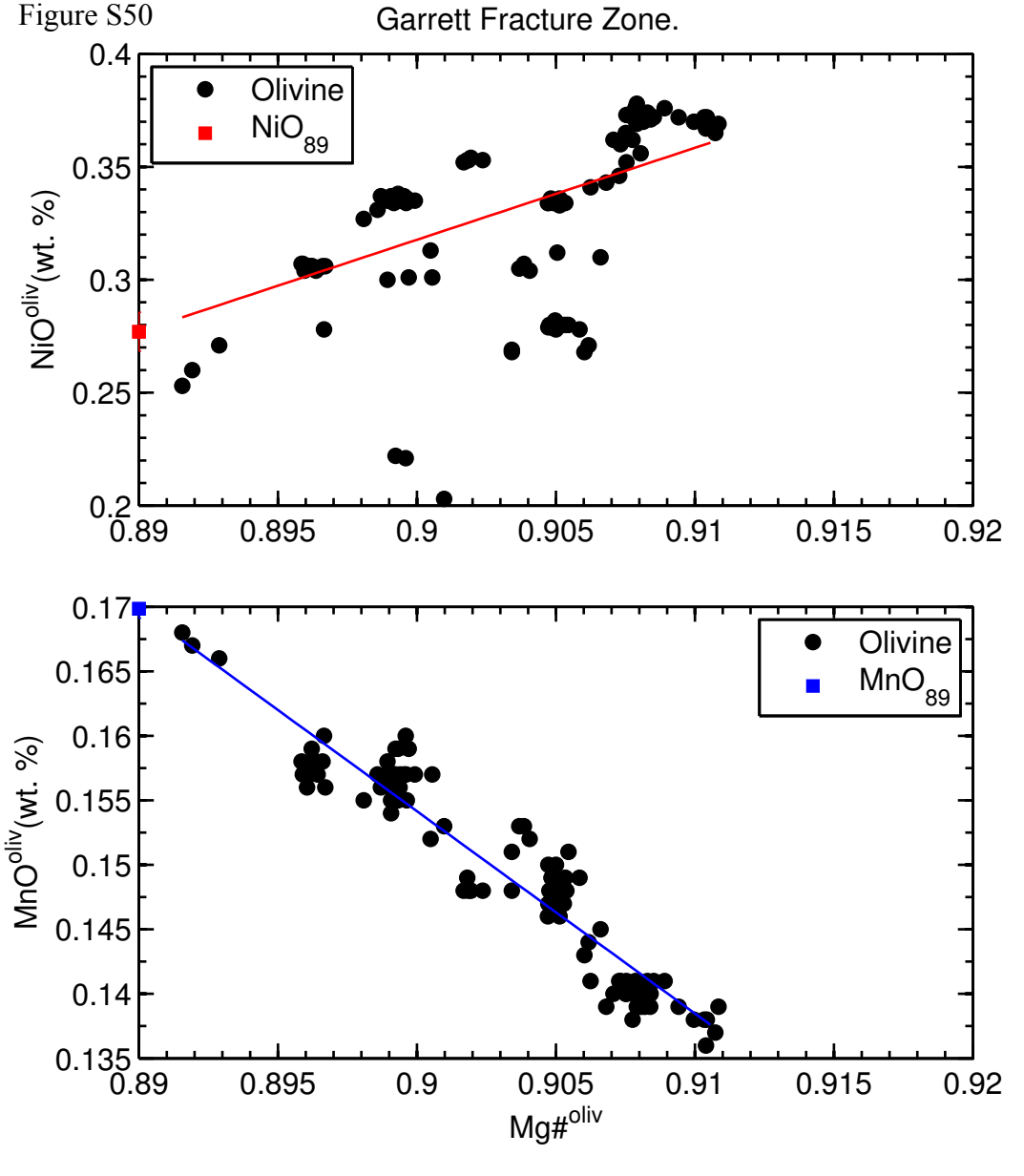
Garrett Fracture Zone.
Olivine
NiO89
NiOoliv(wt. %)
0.4
0.35
0.3
0.25
0.2
0.89
0.895
0.9
0.905
0.91
0.915
0.92
Olivine
MnO89
MnOoliv(wt. %)
0.17
0.165
0.16
0.155
0.15
0.145
0.14
0.135
Mg#oliv

Figure S51

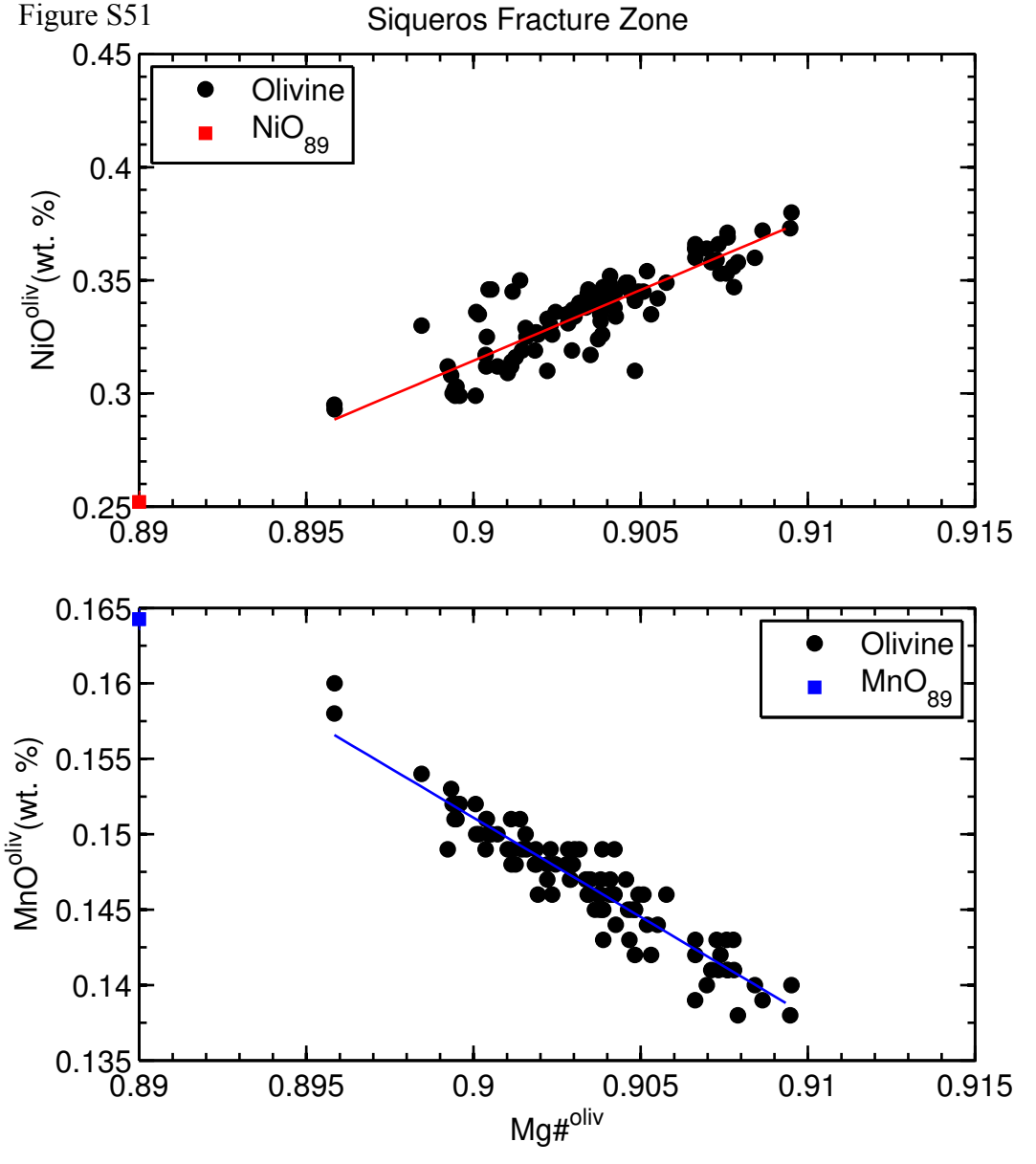
Siqueros Fracture Zone
Olivine
NiO89
NiOoliv(wt. %)
0.45
0.4
0.35
0.3
0.25
0.89
0.895
0.9
0.905
0.91
0.915
Olivine
MnO89
MnOoliv(wt. %)
0.165
0.16
0.155
0.15
0.145
0.14
0.135
Mg#oliv

Figure S52

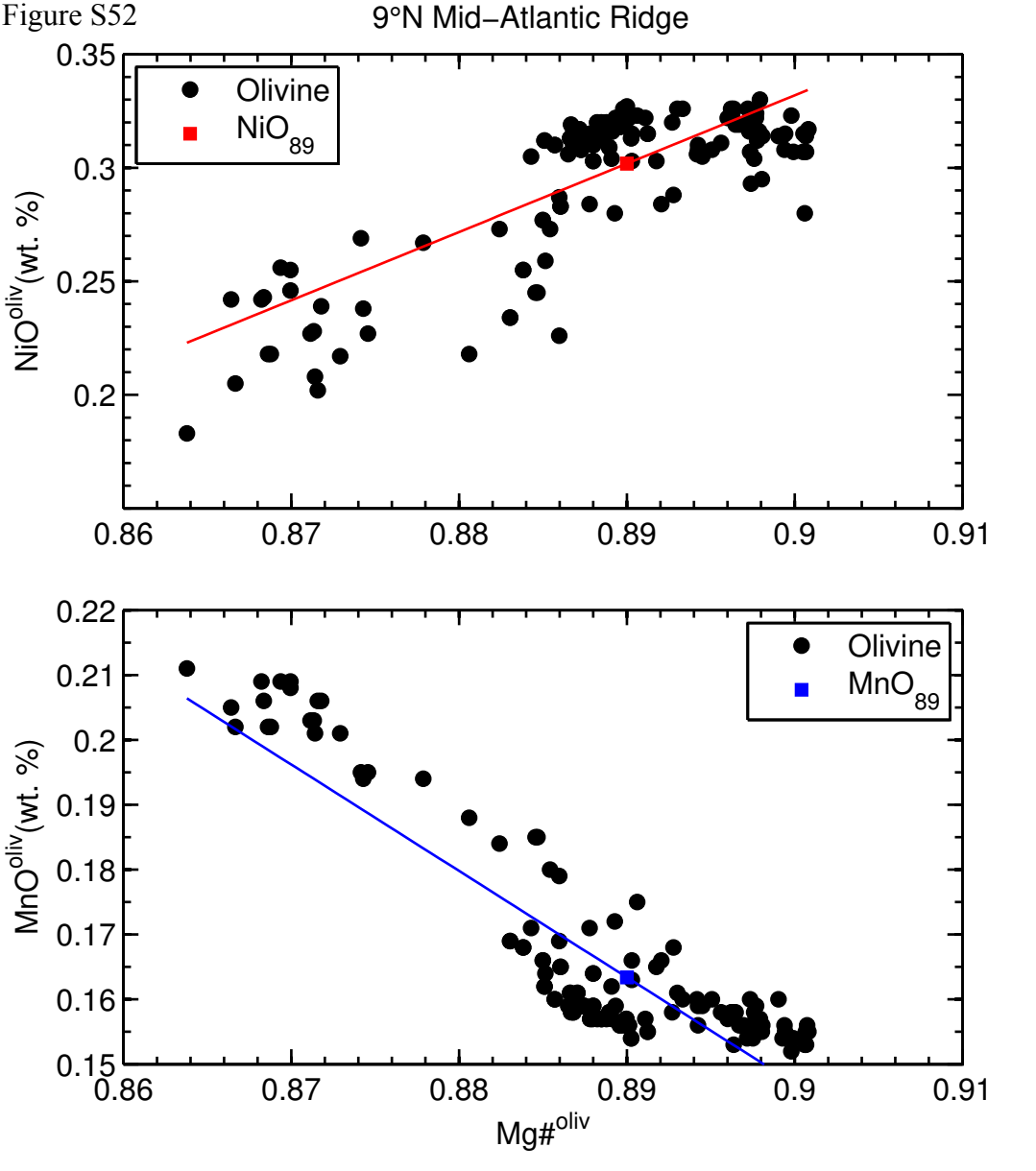
9°N Mid–Atlantic Ridge
Olivine
NiO89
NiOoliv(wt. %)
0.35
0.3
0.25
0.2
0.86
0.87
0.88
0.89
0.9
0.91
Olivine
MnO89
MnOoliv(wt. %)
0.22
0.21
0.2
0.19
0.18
0.17
0.16
0.15
Mg#oliv

Figure S53

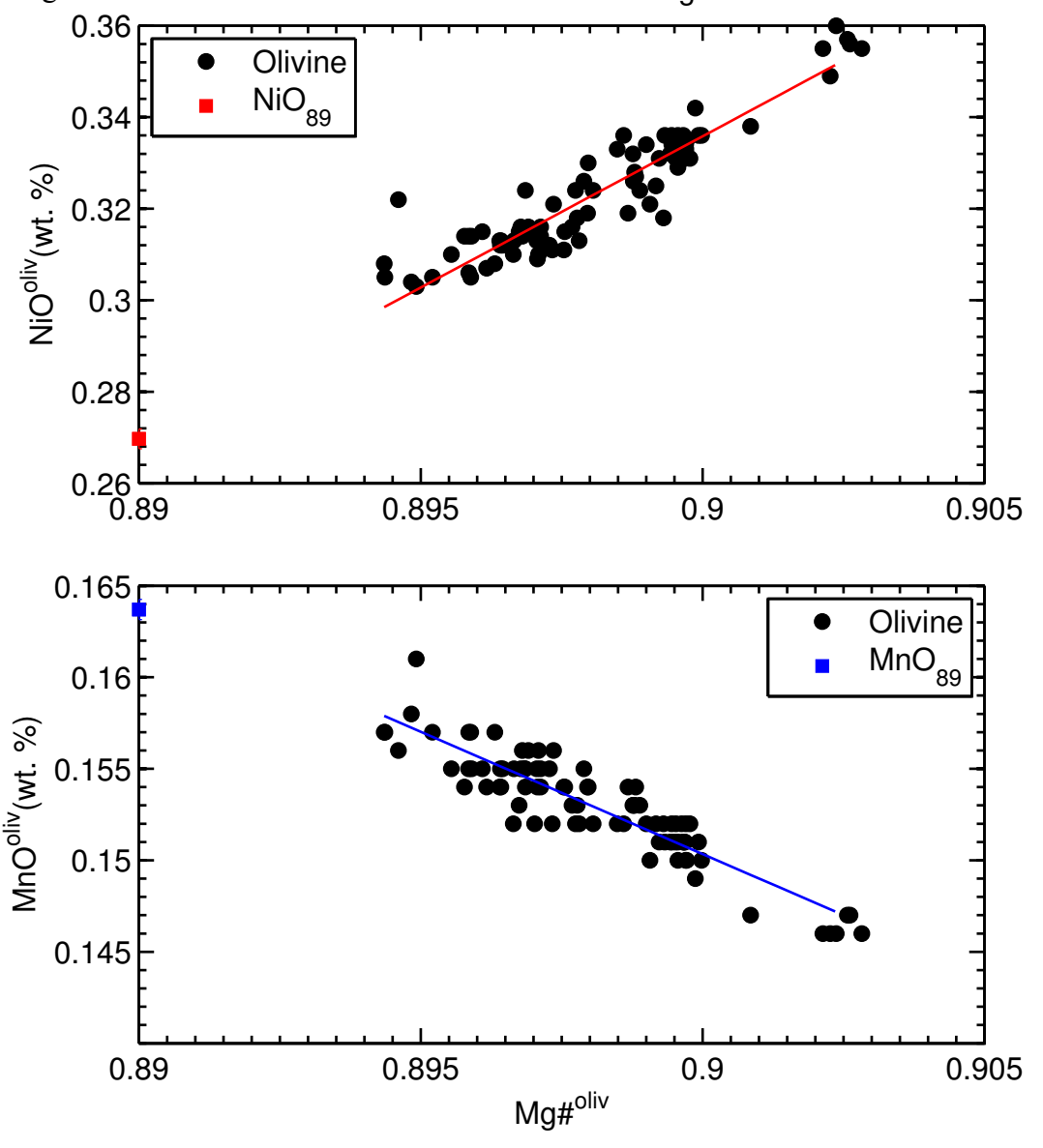
43°N Mid−Atlantic Ridge−1
Olivine
NiO89
NiOoliv(wt. %)
0.36
0.34
0.32
0.3
0.28
0.26
0.89
0.895
0.9
0.905
Olivine
MnO89
MnOoliv(wt. %)
0.165
0.16
0.155
0.15
0.145
0.89
0.895
0.9
0.905
Mg#oliv

Figure S54

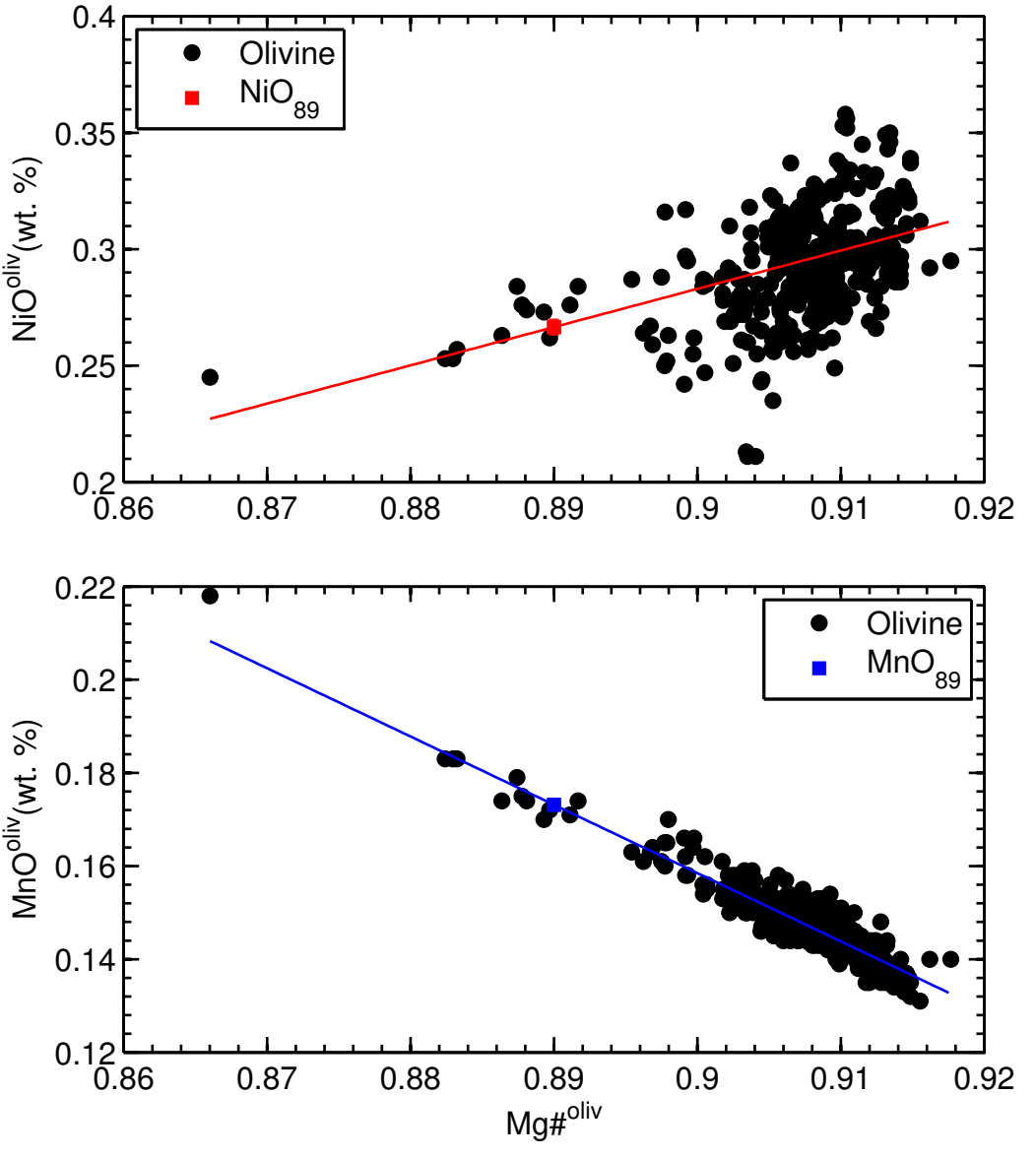
43°N Mid−Atlantic Ridge−2
Olivine
NiO89
NiOoliv(wt. %)
0.4
0.35
0.3
0.25
0.2
0.86
0.87
0.88
0.89
0.9
0.91
0.92
Olivine
MnO89
MnOoliv(wt. %)
0.22
0.2
0.18
0.16
0.14
0.12
Mg#oliv

Figure S55

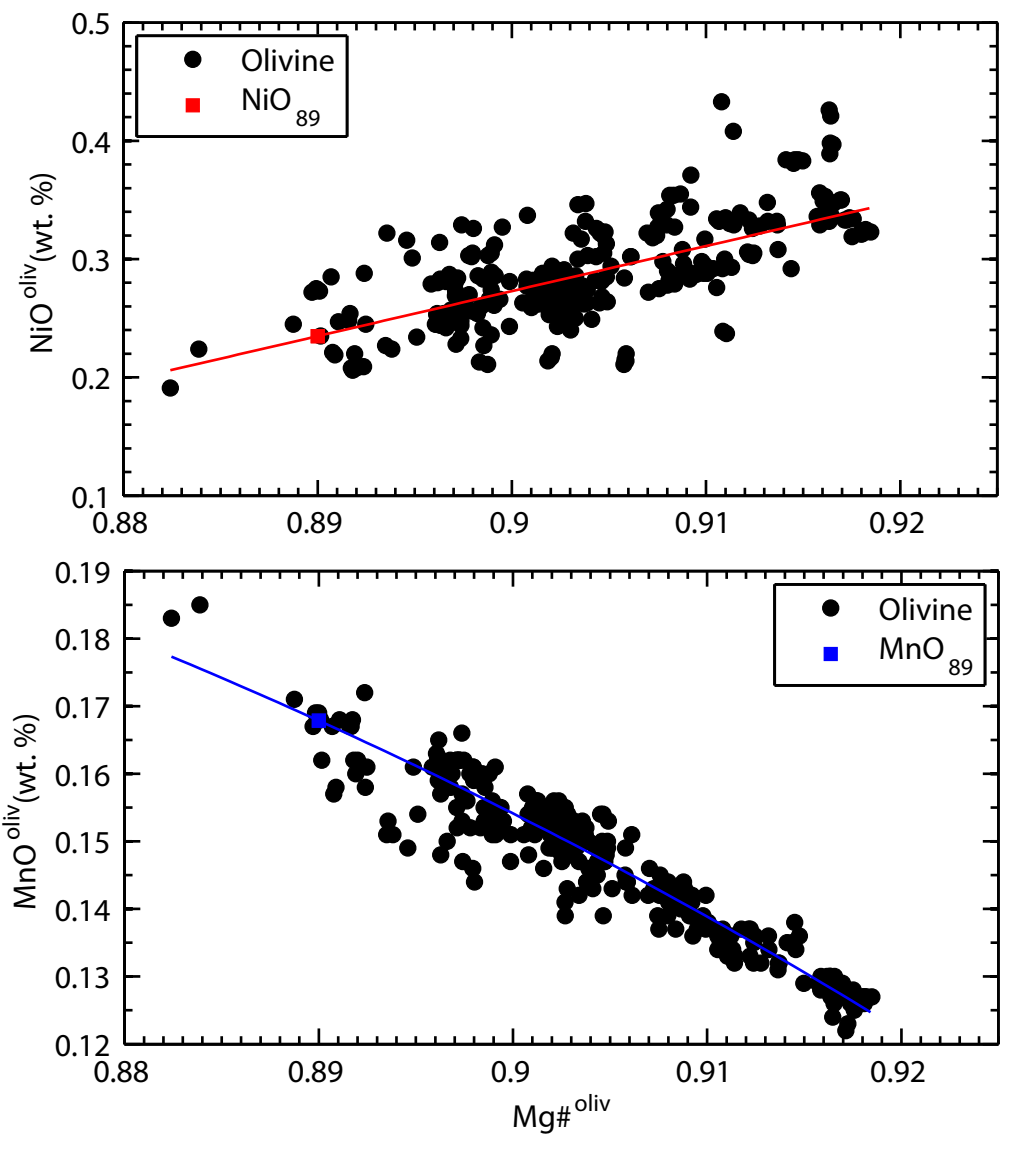
Famous
Olivine
NiO 89
NiO oliv (wt. %)
0.5
0.4
0.3
0.2
0.1
0.88
0.89
0.9
0.91
0.92
Olivine
MnO 89
MnO oliv (wt. %)
0.19
0.18
0.17
0.16
0.15
0.14
0.13
0.12
Mg# oliv

Figure S56

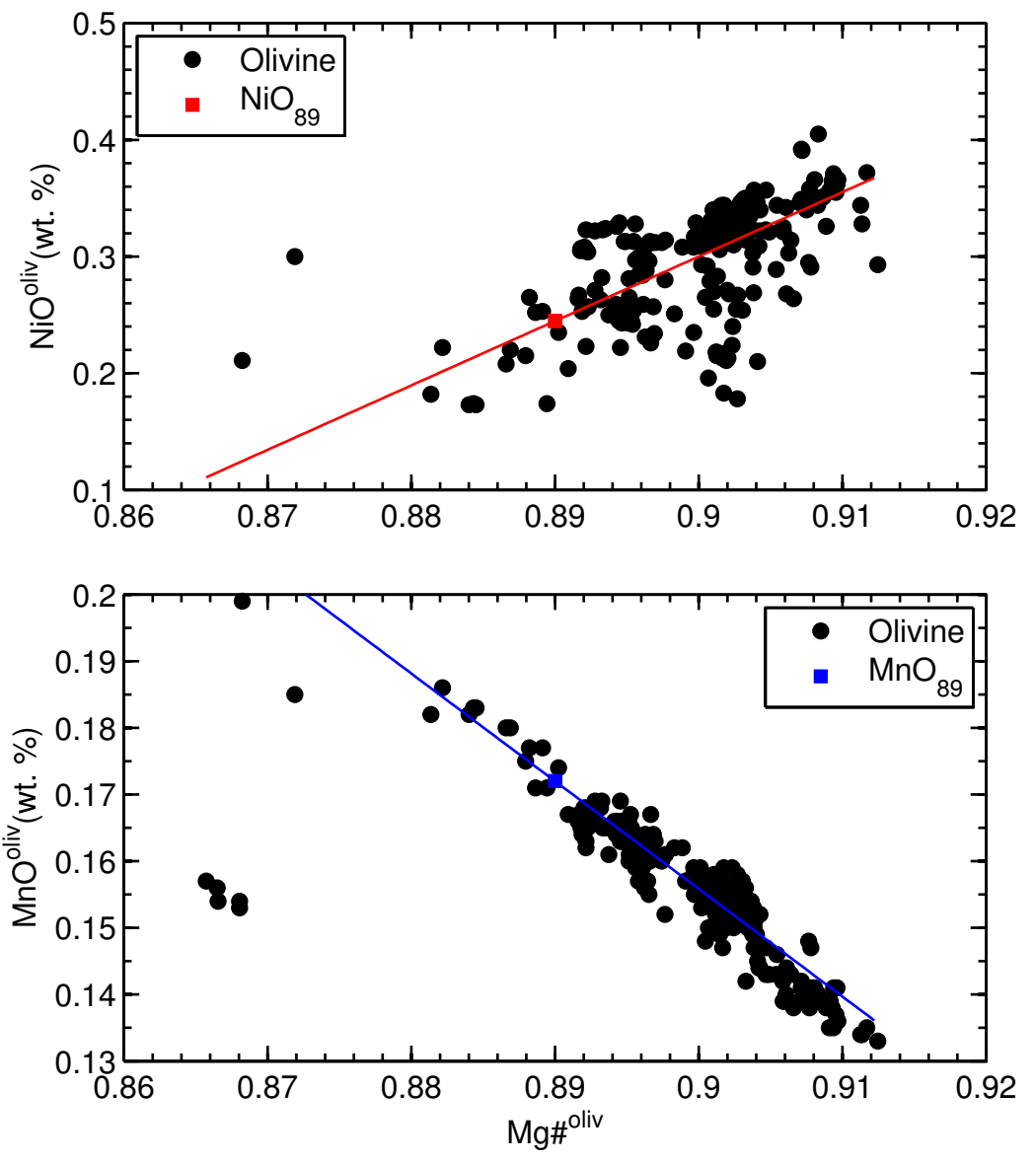
Bouvet
Olivine
NiO89
NiOoliv(wt. %)
0.5
0.4
0.3
0.2
0.1
0.86
0.87
0.88
0.89
0.9
0.91
0.92
Olivine
MnO89
MnOoliv(wt. %)
0.2
0.19
0.18
0.17
0.16
0.15
0.14
0.13
Mg#oliv

Figure S57

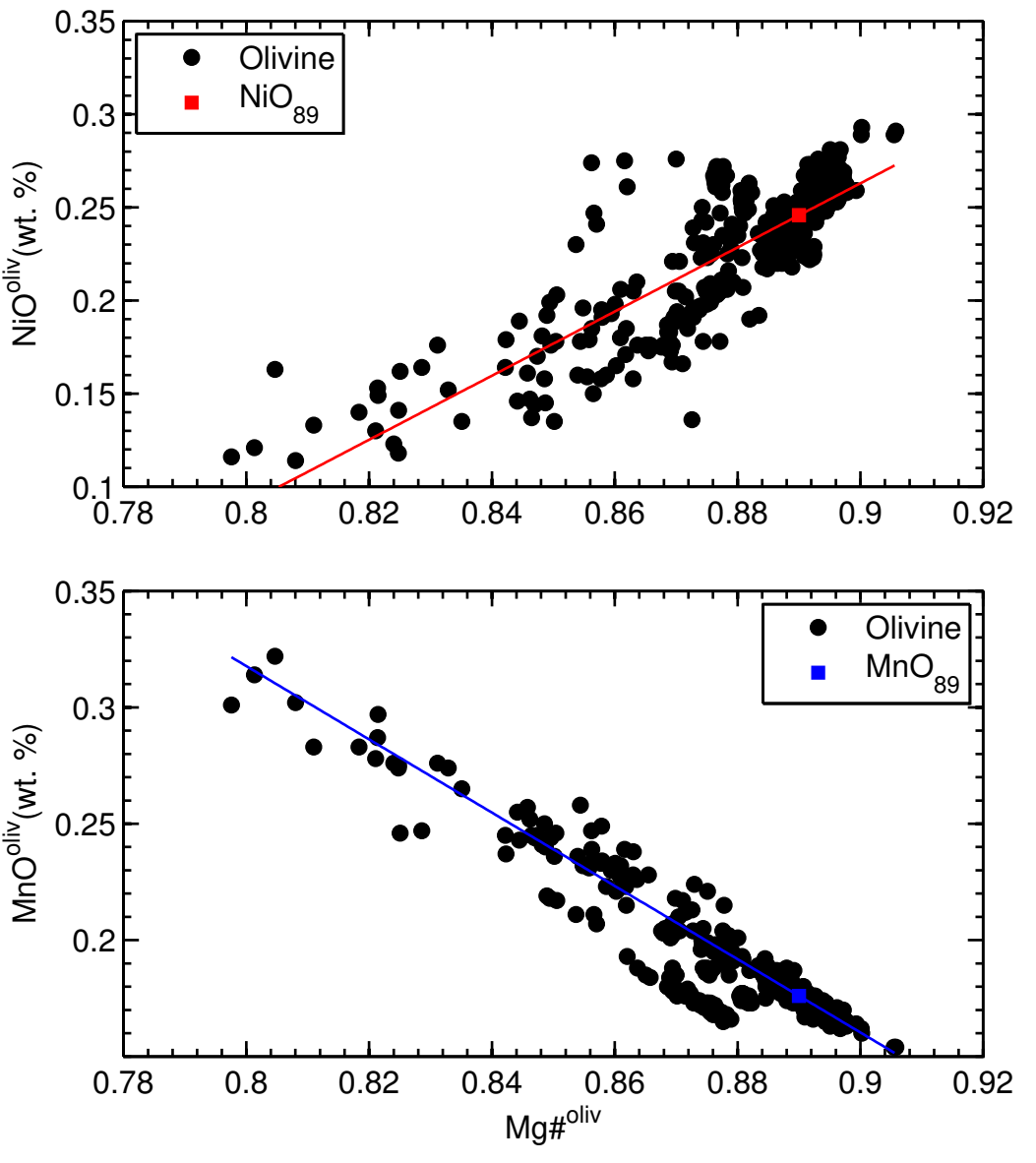
Romanche Fracture Zone
Olivine
NiO89
NiOoliv(wt. %)
0.35
0.3
0.25
0.2
0.15
0.1
0.78
0.8
0.82
0.84
0.86
0.88
0.9
0.92
Olivine
MnO89
MnOoliv(wt. %)
0.35
0.3
0.25
0.2
0.78
0.8
0.82
0.84
0.86
0.88
0.9
0.92
Mg#oliv

Figure S58

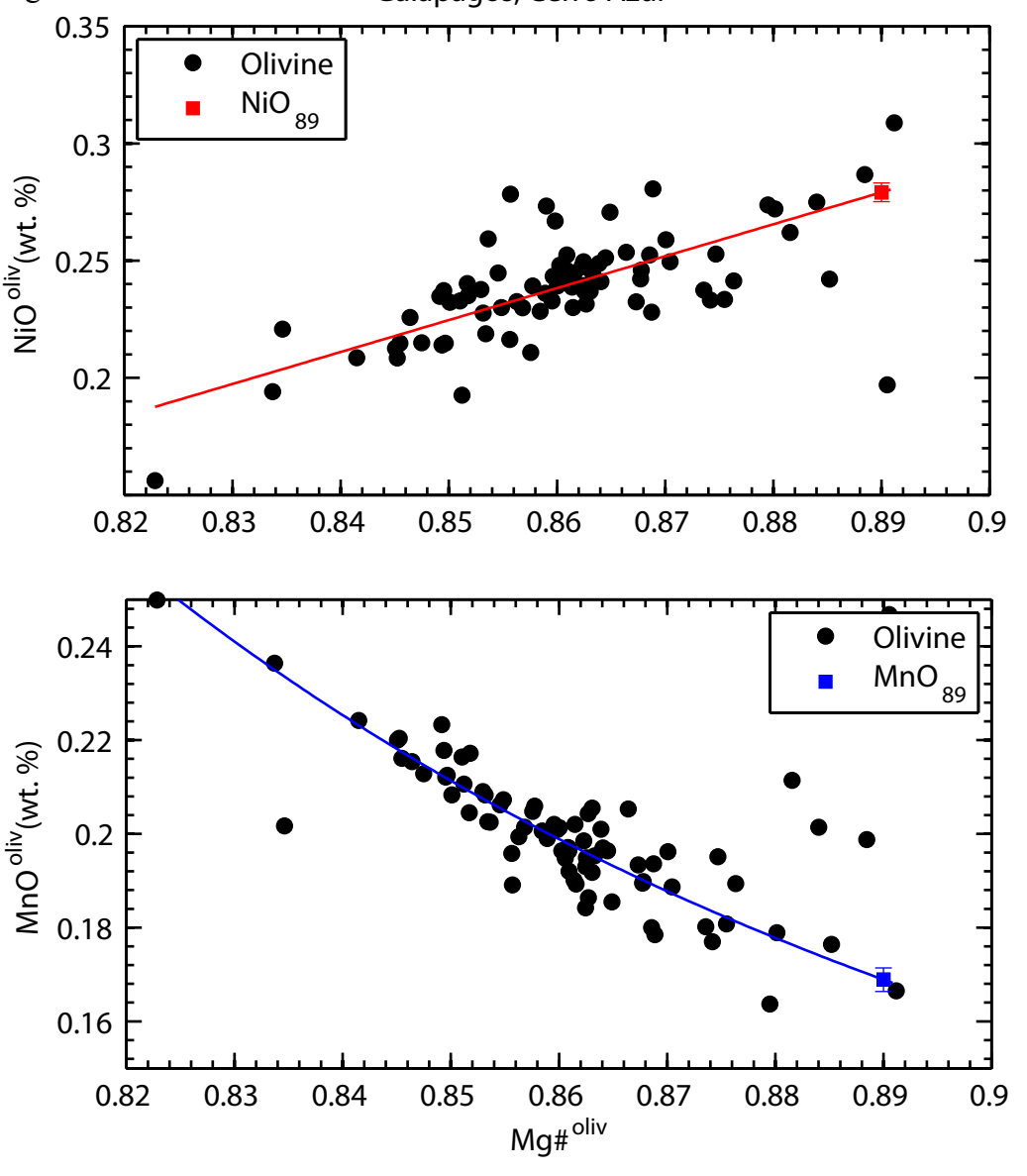
Galapagos, Cerro Azul
Olivine
NiO 89
NiO oliv (wt. %)
0.35
0.3
0.25
0.2
0.82
0.83
0.84
0.85
0.86
0.87
0.88
0.89
0.9
Olivine
MnO 89
MnO oliv (wt. %)
0.24
0.22
0.2
0.18
0.16
Mg# oliv

Figure S59

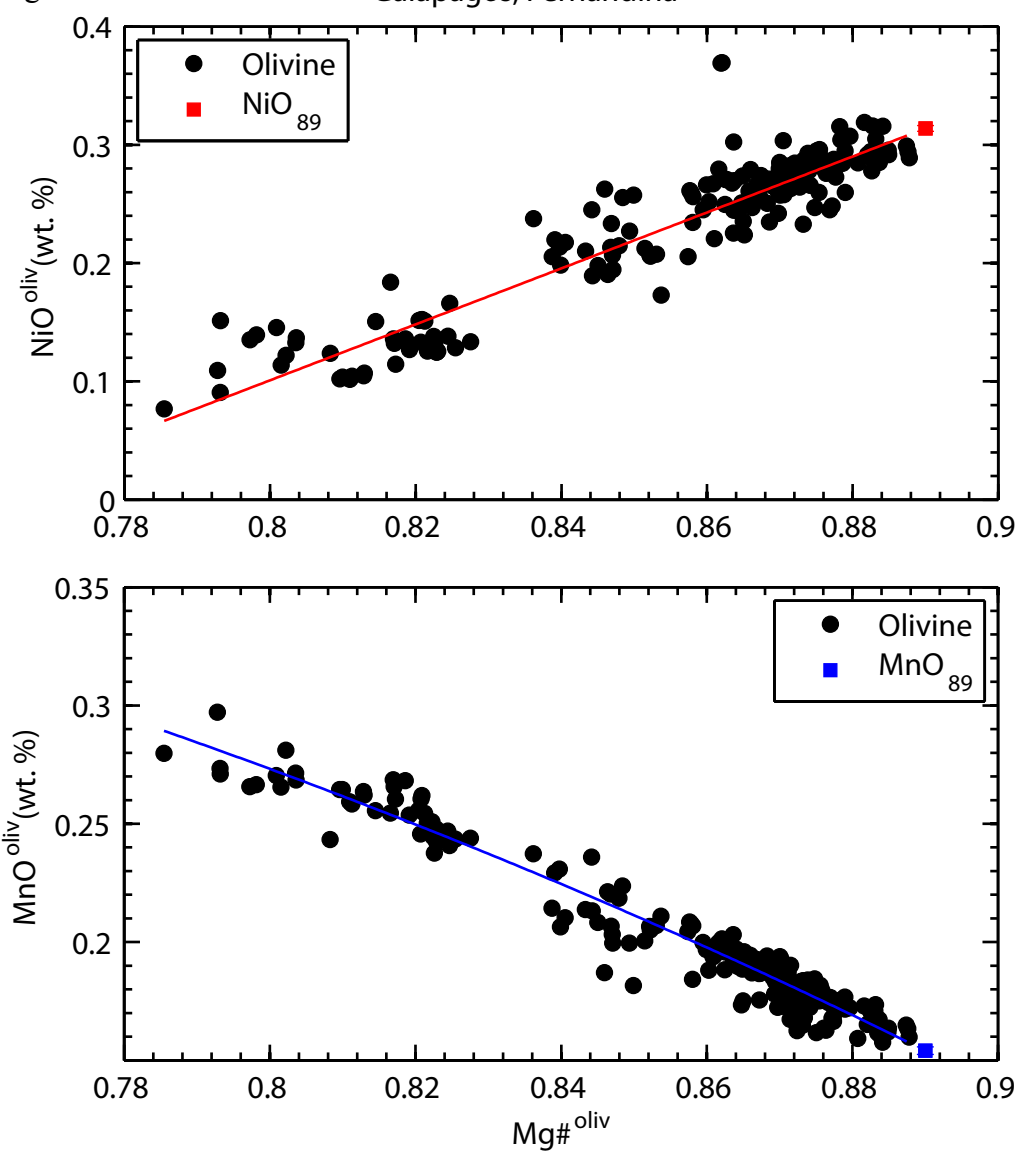
Galapagos, Fernandina
Olivine
NiO 89
NiO oliv (wt. %)
0.4
0.3
0.2
0.1
0
0.78
0.8
0.82
0.84
0.86
0.88
0.9
Olivine
MnO 89
MnO oliv (wt. %)
0.35
0.3
0.25
0.2
0.78
0.8
0.82
0.84
0.86
0.88
0.9
Mg# oliv

Figure S60

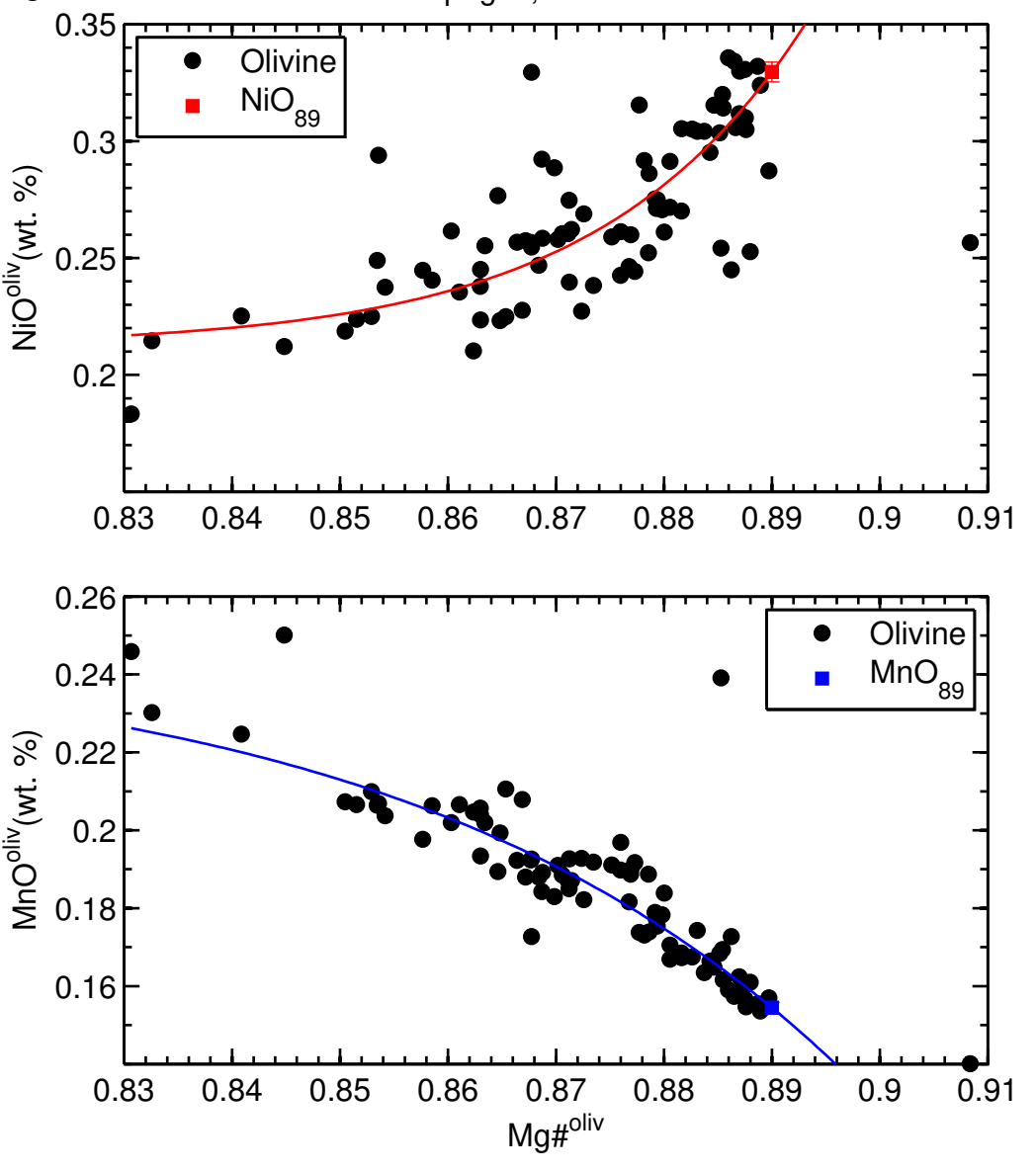
Galapagos, Floreana
Olivine
NiO89
NiOoliv(wt. %)
0.35
0.3
0.25
0.2
0.83
0.84
0.85
0.86
0.87
0.88
0.89
0.9
0.91
Olivine
MnO89
MnOoliv(wt. %)
0.26
0.24
0.22
0.2
0.18
0.16
Mg#oliv

Figure S61

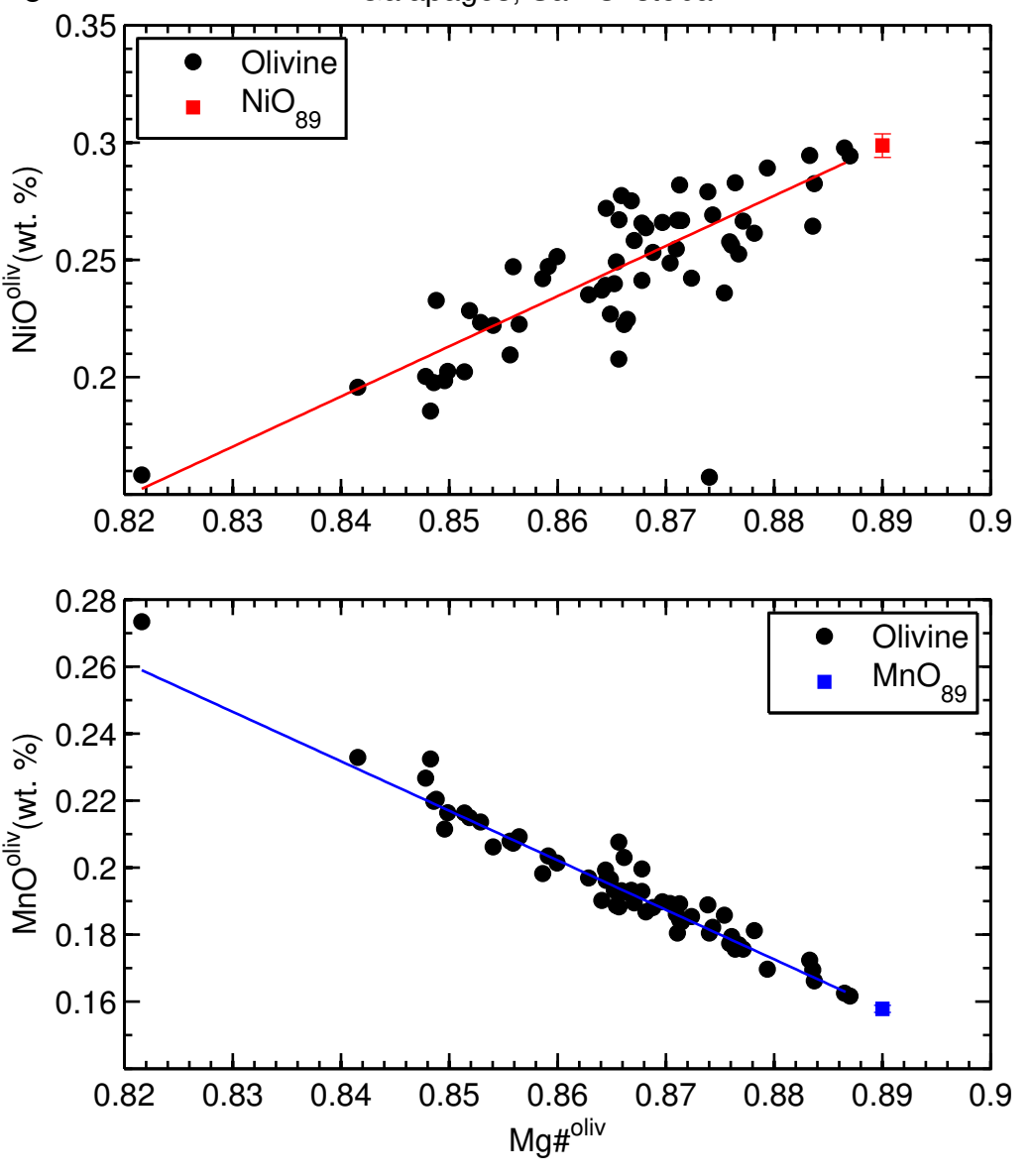
Galapagos, San Cristobal–1
Olivine
NiO89
NiOoliv(wt. %)
0.35
0.3
0.25
0.2
0.82
0.83
0.84
0.85
0.86
0.87
0.88
0.89
0.9
Olivine
MnO89
MnOoliv(wt. %)
0.28
0.26
0.24
0.22
0.2
0.18
0.16
Mg#oliv

Figure S62

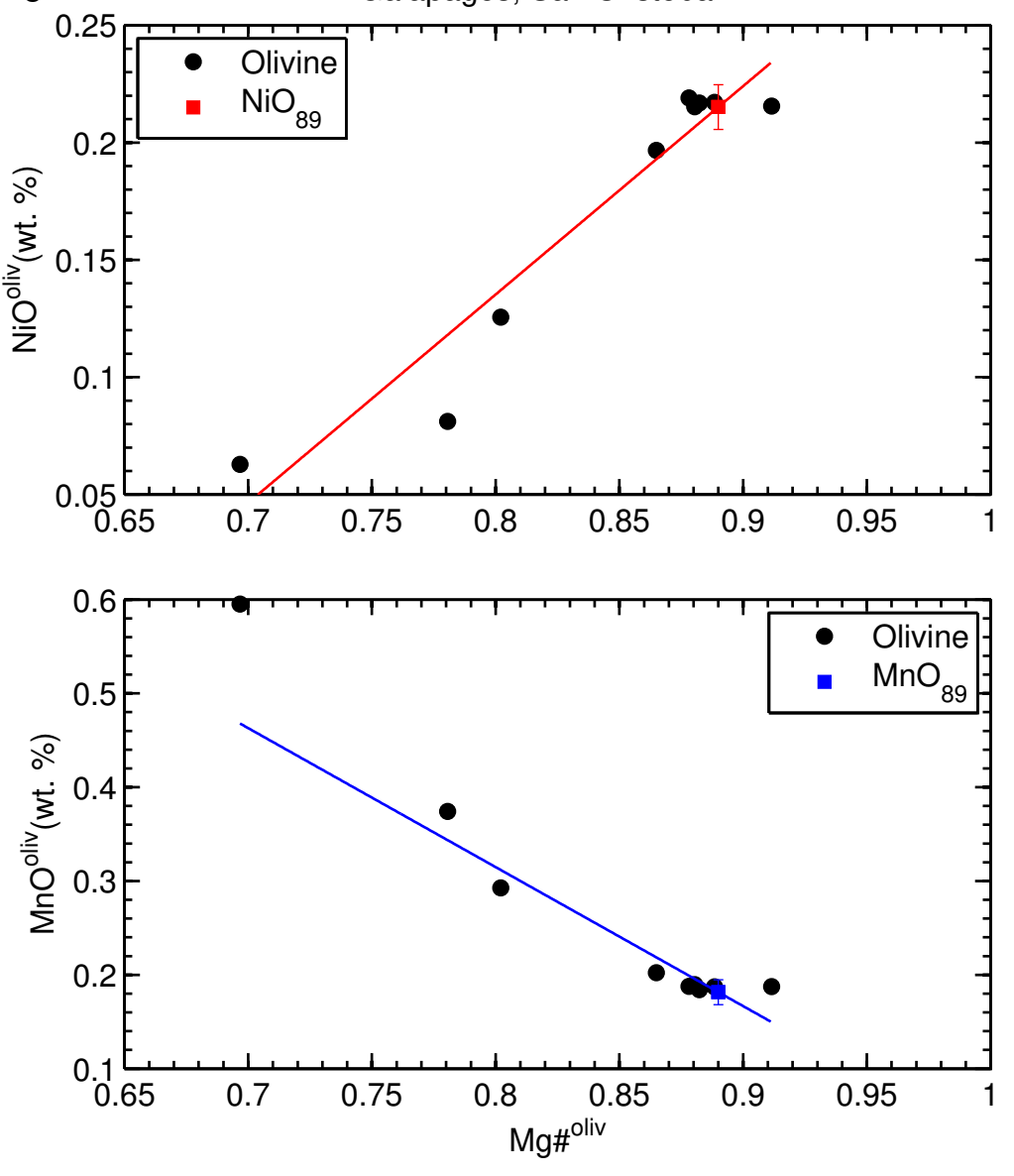
Galapagos, San Cristobal–2
Olivine
NiO89
NiOoliv(wt. %)
0.25
0.2
0.15
0.1
0.05
0.65
0.7
0.75
0.8
0.85
0.9
0.95
1
Olivine
MnO89
MnOoliv(wt. %)
0.6
0.5
0.4
0.3
0.2
0.1
Mg#oliv

Figure S63

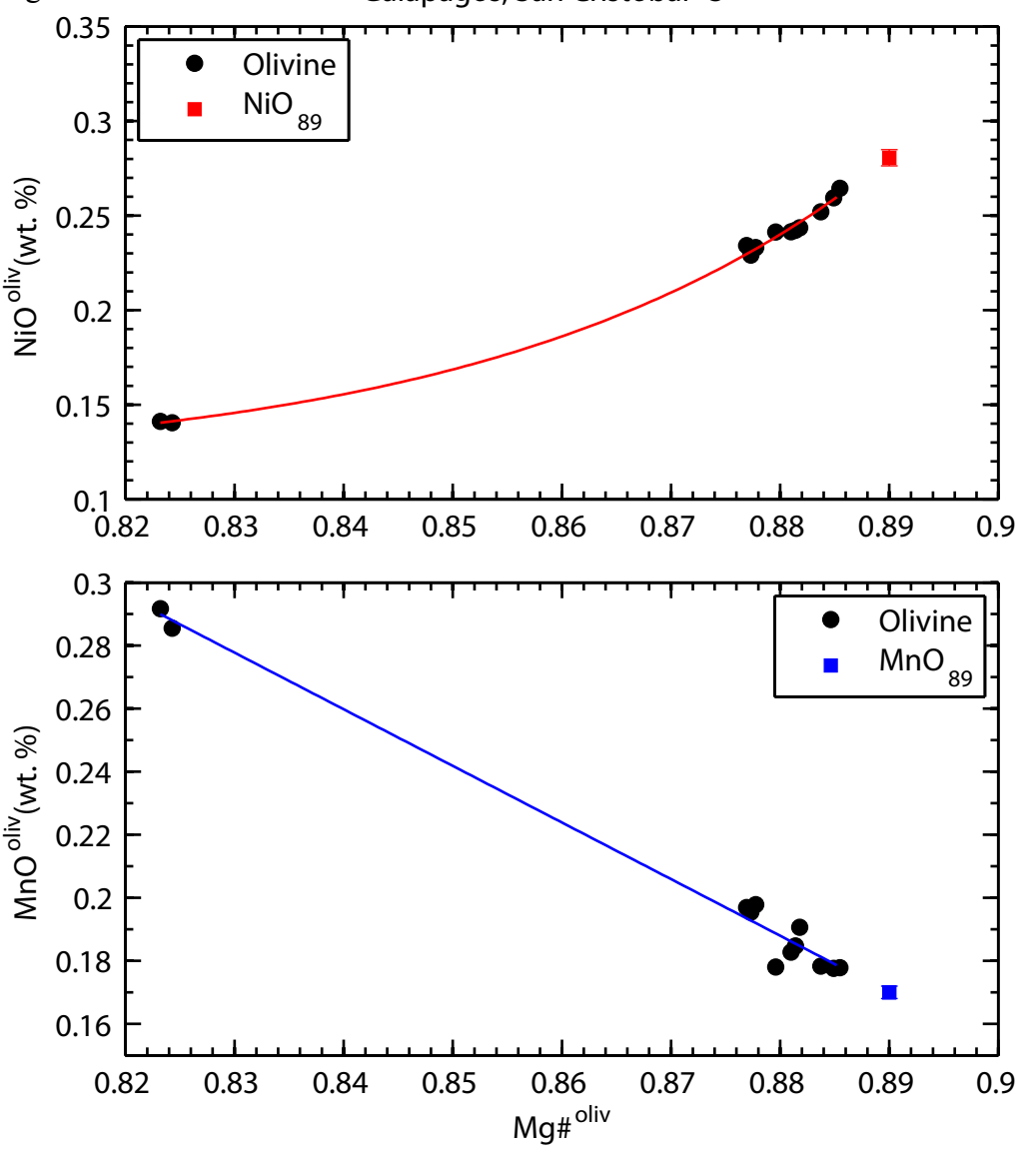
Galapagos, San Cristobal−3
Olivine
NiO 89
NiO oliv (wt. %)
0.35
0.3
0.25
0.2
0.15
0.1
0.82
0.83
0.84
0.85
0.86
0.87
0.88
0.89
0.9
Olivine
MnO 89
MnO oliv (wt. %)
0.3
0.28
0.26
0.24
0.22
0.2
0.18
0.16
Mg# oliv

Table S1: MnO_{89}, NiO_{89} and depths to the lithosphere-asthenosphere boundary

Location	Max Fo	Min Fo	MnO_{89} (wt.%)	error	NiO_{89} (wt.%)	error	MnO-Mg# slope (wt.%/Mg#)	NiO-Mg# slope (wt.%/Mg#)	a (Mn)	b (Mn)	c (Mn)	a (Ni)	b (Ni)	c (Ni)	LAB (km)
Mull Island-1	88.6	76.4	0.1496	0.0013	0.3829	0.0029	–1.325	1.314	0.29697	–2.80760	–0.26231	1.31423	–0.78678	0	-
Mull Island-2	88.9	80.9	0.1602	0.0005	0.3343	0.0032	–1.268	3.517	–1.26850	1.28914	0	1.31620	16.35744	0.13868	-
Mull Island-3	89.7	69.3	0.1566	0.0006	0.3643	0.0016	–1.159	2.162	0.40622	–2.02939	–0.35803	0.59457	7.96709	0.12936	-
Baffin Bay	92.6	84.9	0.1633	0.0003	0.3693	0.0013	–1.252	3.548	0.20612	–3.81882	–0.15841	3.54843	–2.78883	0	65
Greenland	92.7	83.9	0.1592	0.0004	0.4038	0.0015	–1.248	2.022	–1.24780	1.26979	0	2.02205	–1.39580	0	100
Disko	89.0	86.2	0.1648	0.0002	0.3947	0.0008	–1.351	2.511	–1.35124	1.36742	0	2.51123	–1.84025	0	-
Ontong Java Plateau-1	89.5	80.7	0.1627	0.0003	0.3268	0.0021	–1.549	3.637	–1.54860	1.54095	0	1.15964	14.42523	0.11089	-
Ontong Java Plateau-2	89.4	84.1	0.1406	0.0006	0.4277	0.0052	–1.275	1.590	–1.27486	1.27524	0	1.59018	–0.98760	0	-
Karoo-1	90.1	81.0	0.1517	0.0003	0.3468	0.0025	–1.329	2.178	–1.32946	1.33495	0	2.17841	–1.59196	0	-
Karoo-2	90.9	83.6	0.1362	0.0003	0.5153	0.0018	–1.250	3.306	–1.24976	1.24848	0	3.30595	–2.42701	0	-
Emeishan-1	91.2	82.9	0.1865	0.0004	0.3146	0.0010	–1.295	1.002	0.08154	–6.93995	0.0034856	1.00194	–0.57710	0	-
Emeishan-2	91.7	75.9	0.1552	0.0005	0.4133	0.0018	–1.324	2.052	–1.32378	1.33332	0	0.55231	6.49880	0.15427	-
Zawl-Kelkelti	89.7	65.0	0.1575	0.0007	0.3361	0.0024	–1.348	3.862	–3.78109	0.33054	3.79574	1.10876	11.95915	0.06098	-
Reunion, Piton de Neige	90.1	84.3	0.1551	0.0006	0.3616	0.0013	–1.441	1.851	–1.44099	1.43758	0	1.85079	–1.28560	0	83.4
Kilauea Iki	89.0	83.4	0.1467	0.0003	0.4432	0.0032	–1.362	9.414	–1.36222	1.35904	0	399.12310	69.53426	0.32240	90.1
Mauna Loa, Puu Wahi	89.0	83.0	0.1460	0.0002	0.4107	0.0038	–1.404	4.978	–1.40358	1.39516	0	7.29411	34.79678	0.28424	90.1
Mauna Loa, HSDP–2	91.0	79.6	0.1458	0.0001	0.4396	0.0015	–1.315	4.248	–0.55570	2.88534	0.54284	1.43026	18.25360	0.26918	90.1
Mauna Kea, HSDP–2	91.0	77.6	0.1443	0.0001	0.4157	0.0006	–1.369	3.797	–0.49535	3.65645	0.46776	1.06749	14.00328	0.20690	90.1
Mauna Kea, Post Shield	89.5	79.7	0.1459	0.0006	0.3725	0.0039	–1.753	5.355	–0.48821	7.67351	0.34550	5.17292	30.83390	0.23022	90.1
Koolau, Makapuu	89.8	80.7	0.1404	0.0003	0.4787	0.0024	–1.227	3.093	–1.22698	1.23245	0	3.09335	–2.27439	0	88.8
Koolau, KSDP	89.5	84.3	0.1415	0.0005	0.4551	0.0025	–1.166	2.040	–1.16559	1.17887	0	2.03991	–1.36044	0	88.8
Koolau, KSDP, measured	*89.10*		*0.142*		*0.509*										
Loihi Seamount	90.2	77.3	0.1525	0.0002	0.3802	0.0018	–1.318	3.522	–1.31810	1.32564	0	1.14197	15.99933	0.20325	90.3
Kauai, Haena	88.9	83.2	0.1504	0.0011	0.4221	0.0019	–0.609	1.404	0.017787	–9.72491	0.095159	1.40440	–0.82779	0	88.8
Kauai, Haena, measured	*88.92*		*0.135*		*0.493*										
Suiko Seamount	89.1	82.4	0.1437	0.0007	0.4471	0.0045	–0.915	2.734	0.017141	–11.91140	0.075023	2.73439	–1.98648	0	64.8
Detroit Seamount	90.4	82.5	0.1570	0.0003	0.3652	0.0015	–1.449	2.580	–1.44948	1.44706	0	2.58043	–1.93141	0	49.5
La Gomera	89.4	87.7	0.1585	0.0016	0.3555	0.0238	–1.567	3.282	–1.56734	1.55345	0	3.28245	–2.56588	0	95.9
Gran Canaria	90.0	79.9	0.1508	0.0009	0.4264	0.0054	–1.150	1.560	–1.15006	1.17440	0	1.56035	–0.96235	0	96.1
Reykjanes, Haleyjabunga	90.9	88.2	0.1743	0.0006	0.2751	0.0015	–1.809	3.830	0.067966	–9.11817	–0.022371	3.83009	–3.13366	0	32.3
Reykjanes, Haleyjabunga, measured	*88.96*		*0.181*		*0.221*										
Reykjanes, Lagafell	91.3	88.9	0.1744	0.0008	0.2548	0.0049	–1.606	3.878	–1.60607	1.60384	0	3.87827	–3.19683	0	32.3
Reykjanes, Sulur/Stapafell	89.1	80.2	0.1665	0.0006	0.3089	0.0031	–1.480	1.977	–1.47996	1.48364	0	1.97695	–1.45055	0	32.3
Hengill, Midfell/Maelifell	91.0	82.9	0.1678	0.0003	0.2818	0.0017	–1.516	2.649	–1.51599	1.51704	0	2.64856	–2.07544	0	32.3
Kistufell	89.6	84.6	0.1625	0.0002	0.3127	0.0010	–1.729	3.387	–1.72932	1.70158	0	3.38736	–2.70200	0	32.3
Theistareykir, Laufrandarhraun–1	91.1	85.4	0.1723	0.0003	0.2590	0.0014	–1.631	4.187	–1.63100	1.62386	0	4.18693	–3.46739	0	32.3
Theistareykir, Laufrandarhraun–2	89.9	86.3	0.1655	0.0005	0.3281	0.0029	–1.442	2.239	–1.44189	1.44874	0	2.23906	–1.66470	0	32.3
Theistareykir, Laufrandarhraun–3	88.7	86.9	0.1652	0.0008	0.3292	0.0032	–1.601	3.663	–1.60127	1.59035	0	3.66307	–2.93095	0	32.3
Theistareykir, Langavitishraun	91.7	86.8	0.1680	0.0006	0.2838	0.0026	–1.406	1.033	–1.40621	1.41950	0	1.03278	–0.63539	0	32.3
Theistareykir, Theistareykjahraun	90.4	86.9	0.1635	0.0003	0.3349	0.0015	–1.511	3.062	–1.51070	1.50799	0	3.06154	–2.38986	0	32.3
Snaefellsness, Enni	89.6	78.7	0.1635	0.0006	0.2997	0.0041	–1.397	3.829	–1.39718	1.40701	0	1.15922	13.41432	0.05690	32.3
Snaefellsness, Sydri–/Ytri–Raudamelur	89.7	83.4	0.1681	0.0008	0.2699	0.0027	–1.839	2.331	–1.83856	1.80437	0	2.33146	–1.80513	0	32.3
Sao Migel-1	88.9	77.8	0.1468	0.0003	0.3099	0.0006	–1.357	1.740	–0.39872	6.55957	0.33245	1.73965	–1.23839	0	67.6
Sao Migel-2	89.6	86.2	0.1441	0.0002	0.2687	0.0014	–1.686	16.733	–0.72637	20.10232	0.21386	19936723.76	170.23874	0.22036	67.6
Sao Migel-3	90.3	77.3	0.1600	0.0004	0.2825	0.0012	–1.888	6.350	–0.51185	10.92397	0.30335	7.71907	35.37976	0.15749	67.6
Treceria	89.4	72.5	0.1618	0.0006	0.3394	0.0023	–0.966	5.855	0.091192	–5.21045	–0.0055727	2.48761	19.49230	0.082781	47.2
Southeast Indian Ridge	90.6	83.5	0.1729	0.0002	0.2553	0.0013	–1.679	5.869	–1.67910	1.66732	0	5.19696	32.01483	0.13066	0
Garrett Fracture Zone.	91.1	89.2	0.1698	0.0007	0.2770	0.0086	–1.568	4.070	–1.56790	1.56528	0	4.07049	–3.34572	0	0
Siqueros Fracture Zone	91.0	89.6	0.1643	0.0007	0.2521	0.0046	–1.316	6.246	–1.31599	1.33549	0	6.24578	–5.30668	0	0
9°N Mid-Atlantic Ridge	90.1	86.4	0.1634	0.0007	0.3018	0.0018	–1.640	3.010	–1.64022	1.62320	0	3.01012	–2.37718	0	0
43°N Mid-Atlantic Ridge-1	90.3	89.4	0.1637	0.0006	0.2697	0.0022	–1.336	6.613	–1.33606	1.35280	0	6.61260	–5.61551	0	0
43°N Mid-Atlantic Ridge-2	91.8	86.6	0.1732	0.0005	0.2666	0.0034	–1.466	1.643	–1.46581	1.47773	0	1.64260	–1.19535	0	0
Famous	91.8	88.2	0.1679	0.0006	0.2349	0.0036	–1.513	3.808	–0.37516	10.54987	0.27757	3.80804	–3.15426	0	0
Bouvet	91.2	86.6	0.1720	0.0003	0.2448	0.0036	–1.615	5.522	–1.61521	1.60954	0	5.52202	–4.66981	0	0
Romanche Fracture Zone	90.6	79.8	0.1761	0.0002	0.2457	0.0010	–1.574	1.722	–1.57417	1.57707	0	1.72173	–1.28662	0	0
Galapagos, Cerro Azul	89.1	82.3	0.1689	0.0025	0.2792	0.0040	–0.832	1.363	0.031015	–8.73824	0.083028	1.36272	–0.93366	0	35.8
Galapagos, Fernandina	88.8	78.5	0.1541	0.0016	0.3138	0.0025	–1.512	2.365	–0.55953	3.74918	0.51556	2.36528	–1.79128	0	37
Galapagos, Floreana	90.8	83.1	0.1544	0.0014	0.3295	0.0042	–2.284	6.181	–1.21855	22.21810	0.24594	27.96944	46.99125	0.21246	42.1
Galapagos, San Cristobal 1	88.7	82.2	0.1579	0.0011	0.2987	0.0050	–1.477	2.139	–1.47745	1.47279	0	2.13946	–1.60539	0	35.5
Galapagos, San Cristobal2	91.1	69.7	0.1815	0.0132	0.2152	0.0095	–1.481	0.888	–1.48135	1.49993	0	0.88820	–0.57531	0	35.5
Galapagos, San Cristobal3	88.5	82.3	0.1700	0.0020	0.2806	0.0043	–1.797	4.095	–1.79661	1.76896	0	3.13786	25.40665	0.11811	35.5

Notes: Fo = 100Mg# where Mg# = Mg/(Mg+Fe), molar; max and min Fo values are the maximum and minimum Fo values at each locality. The three sample sets/localities in both plain text and italics are those where a small subset of olivine analyses are offset from the main body of data in MnO vs. Mg# and NiO vs. Mg# space; the plain text MnO and NiO values are those calculated using the regression equations and a Mg# of 0.89; those MnO and NiO values in italics represent measured values from the olivine in each "offset" population with a Fo value closest to 89 (Fo value reported under the combined Max Fo/Min Fo headings; see methods for further discussion). Values under the “a”, “b”, and “c” heading are the coefficients for the regressions lines used to calculate MnO_{89} [where the heading contains (Mn)] and NiO_{89} [where the heading contains (Ni)], respectively. Locations where the “c” coefficient is 0 means that a linear fit [$y = a(x) + b$] was used; where a non-zero “c” coefficient is reported, a power-law [$y = a(x^b) + c$] fit was used. LAB (km) refers to the depth of the lithosphere-asthenosphere boundary at the time of volcanism; data sources: ref. 15, 36 and references therein. The reported slopes for Galápagos, Floreana are simply the first derivative of the fits at a Fo of 89 due to the dearth of olivines with Fo contents between ~90.8 (the highest Fo olivine for this location) and 89. Samples used in fits Mull Island-1: BR-5; Mull Island-2: BR-2, BR-6, BHL-15; Mull Island-3: BHL-19, 34, BCH-14, 24, 27, 33, AM-7a, BB-22, B-26, 29; Ontong Java Plateau-1: 1185A 9R 2 92-96, 1187A 6R 6 116-119; Ontong Java Plateau-2: 1187A 10R 7 46-49, Karoo-1: P23-9, 32; Karoo-2: N365; Emeishan-1: EM-43; Emeishan-2: EM-55, 57, 58; Theistareykir, Laufrandarhraun–1: 01-55, 01-57-4, 01-56-1, 01-56-2 ; Theistareykir, Laufrandarhraun–2: 01-44, 01-54; Sao Migel-1: SM-10; Sao Migel-2: SM-16; Sao Migel-3: SM-6, 36, 36a, 4, 33; 43N Mid-Atlantic Ridge-1: 20; 43N Mid-Atlantic Ridge-2: AII-32 11-92, AII-32 12-6(i), (ii), AII-32 12-2, AII-32 12-7, AII-32 11-178; Galapagos, San Cristobal-1: 10.6D, 25.3D, 25.4, 27.6, SC-82-47; Galapagos, San Cristobal-2: SC-82-59; Galapagos, San Cristobal-3: SC-82-76.

Data sources used to fit equations (1), (6), (7), and (8)

S1 Agee, C. B. & Draper, D. S. Experimental constraints on the origin of Martian meteorites and the composition of the Martian mantle. *Earth and Planetary Science Letters* **224**, 415-429 (2004).

S2 Agee, C. B. & Walker, D. Aluminum partitioning between olivine and ultrabasic silicate liquid to 6 GPa. *Contributions to Mineralogy and Petrology* **105**, 243-254 (1990).

S3 Aulbach, S., Pearson, N. J., O'Reilly, S. Y. & Doyle, B. J. Origins of Xenolithic Eclogites and Pyroxenites from the Central Slave Craton, Canada. *Journal of Petrology* **48**, 1843-1873 (2007).

S4 Auwera, J. V. & Longhi, J. Experimental study of a jotunite (hypersthene monzodiorite): constraints on the parent magma composition and crystallization conditions (P,T, fO_2) of the Bjerkreim-Sokndal layered intrusion (Norway). *Contributions to Mineralogy and Petrology* **118**, 60-78 (1994).

S5 Baker, D. R. & Eggler, D. H. Compositions of anhydrous and hydrous melts coexisting with plagioclase, augite, and olivine or low-Ca pyroxene from 1-atm to 8 kbar: Application to the Aleutian volcanic center of Atka. *American Mineralogist* **72**, 12-28 (1987).

S6 Baker, M. B., Grove, T. L. & Price, R. Primitive basalts and andesites from the Mt. Shasta region, N. California: products of varying melt fraction and water content. *Contributions to Mineralogy and Petrology* **118**, 111-129 (1994).

S7 Balta, J. B., Asimow, P. D. & Mosenfelder, J. L. Manganese partitioning during hydrous melting of peridotite. *Geochimica et Cosmochimica Acta* **75**, 5819-5833 (2011).

S8 Bartels, K. S., Kinzler, R. J. & Grove, T. L. High pressure phase relations of primitive high-alumina basalts from Medicine Lake volcano, northern California. *Contributions to Mineralogy and Petrology* **108**, 253-270 (1991).

S9 Boyd, F. R. & Danchin, R. V. Lherzolites, eclogites and megacrysts from some kimberlites of Angola. *American Journal of Science* **280-A**, 528-549 (1980).

S10 Boyd, F. R. & Nixon, P. H. Ultramafic nodules from the Kimberley pipes, South Africa. *Geochimica et Cosmochimica Acta* **42**, 1367-1382 (1978).

S11 Conte, A. M. *et al.* Experimental constraints on evolution of leucite-basanite magma at 1 and 10^{-4} GPa: implications for parental compositions of Roman high-potassium magmas. *European Journal of Mineralogy* **21**, 763-782 (2009).

S12 Creighton, S. Unpublished data, Personal communication, 8/16/2016

S13 Dann, J. C., Holzheid, A. H., Grove, T. L. & McSween Jr., H. Y. Phase equilibria of the Shergotty meteorite: Constraints on pre-eruptive water contents of martian magmas and fractional crystallization under hydrous conditions. *Meteoritics & Planetary Science* **36**, 793-806 (2001).

S14 Davis, F. A., Humayun, M., Hirschmann, M. M. & Cooper, R. S. Experimentally determined mineral/melt partitioning of first-row transition elements (FRTE) during partial melting of peridotite at 3 GPa. *Geochimica et Cosmochimica Acta* **104**, 232-260 (2013).

S15 Draper, D. S. & Johnston, A. D. Anhydrous PT phase relations of an Aleutian high-MgO basalt: an investigation of the role of olivine-liquid reaction in the generation of arc high-alumina basalts. *Contributions to Mineralogy and Petrology* **112**, 501-519 (1992).

S16 Dunn, T. & Sen, C. Mineral/matrix partition coefficients for orthopyroxene, plagioclase, and olivine in basaltic to andesitic systems: A combined analytical and experimental study. *Geochimica et Cosmochimica Acta* **58**, 717-733 (1994).

S17 Elkins-Tanton, L. T., Chatterjee, N. & Grove, T. L. Experimental and petrological constraints on lunar differentiation from the Apollo 15 green picritic glasses. *Meteoritics and Planetary Science* **38**, 515-527 (2003).

S18 Elkins, L. T., Fernandes, V. A., Delano, J. W. & Grove, T. L. Origin of lunar ultramafic green glasses: Constraints from phase equilibrium studies. *Geochimica et Cosmochimica Acta* **64**, 2339-2350 (2000).

S19 Feig, S. T., Koepke, J. & Snow, J. E. Effect of water on tholeiitic basalt phase equilibria: an experimental study under oxidizing conditions. *Contributions to Mineralogy and Petrology* **152**, 611-638 (2006).

S20 Gaetani, G. A. & Grove, T. L. The influence of water on melting of mantle peridotite. *Contributions to Mineralogy and Petrology* **131**, 323-346 (1998).

S21 Grove, T. L., Donnelly-Nolan, J. & Housh, T. Magmatic processes that generated the rhyolite of Glass Mountain, Medicine Lake volcano, N. California. *Contributions to Mineralogy and Petrology* **147**, 205-223 (1997).

S22 Grove, T. L. *et al.* Fractional crystallization and mantle-melting controls on calc-alkaline differentiation trends. *Contributions to Mineralogy and Petrology* **145**, 515-533 (2003).

S23 Grove, T. L., Gerlach, D. C. & Sando, T. W. Origin of calc-alkaline series lavas at Medicine Lake Volcano by fractionation, assimilation and mixing. *Contributions to Mineralogy and Petrology* **80**, 160-182 (1982).

S24 Grove, T. L., Holbig, E. S., Barr, J. A., Till, C. B. & Krawczynski, M. J. Melts of garnet lherzolite: experiments, models and comparison to melts of pyroxenite and carbonated lherzolite. *Contributions to Mineralogy and Petrology* **166**, 887-910 (2013).

S25 Grove, T. L. & Juster, T. C. Experimental investigations of low-Ca pyroxene stability and olivine-pyroxene-liquid equilibria at 1-atm in natural basaltic and andesitic liquids. *Contributions to Mineralogy and Petrology* **103**, 287-305 (1989).

S26 Grove, T. L., Kinzler, R. R. & Bryan, W. B. in *Mantle Flow and Melt Generation at Mid-Ocean Ridges* (eds Jason Phipps Morgan, Donna K. Blackman, & John M. Sinton) (American Geophysical Union, Washington, D. C., 1992).

S27 Hesse, M. & Grove, T. L. Absarokites from the western Mexican Volcanic Belt: constraints on mantle wedge conditions. *Contributions to Mineralogy and Petrology* **146**, 10-27 (2003).

S28 Jago, B. C. & Mitchell, R. H. Ultrabasic xenoliths from the Ham kimberlite, Somerset Island, Northwest Territories. *Canadian Mineralogist* **25**, 515-525 (1987).

S29 Kinzler, R. J. & Grove, T. L. Crystallization and differentiation of Archean komatiite lavas from northeast Ontario: phase equilibrium and kinetic studies. *American Mineralogist* **70**, 40-51 (1985).

S30 Kinzler, R. J. & Grove, T. L. Primary magmas of mid-ocean ridge basalts 1. Experiments and methods. *Journal of Geophysical Research* **97**, 6885–6906 (1992).

S31 Le Roux, V., Dasgupta, R. & Lee, C. T. A. Mineralogical heterogeneities in the Earth's mantle: Constraints from Mn, Co, Ni and Zn partitioning during partial melting. *Earth and Planetary Science Letters* **307**, 395-408 (2011).

S32 Longhi, J. Liquidus equilibria of some primary lunar and terrestrial melts in the garnet stability field. *Geochimica et Cosmochimica Acta* **59**, 2375-2386 (1995).

S33 Longhi, J. Some phase equilibrium systematics of lherzolite melting: I. *Geochemistry, Geophysics, Geosystems* **3**, 10.1029/2001GC000204 (2002).

S34 Longhi, J., Durand, S. R. & Walker, D. The pattern of Ni and Co abundances in lunar olivines. *Geochimica et Cosmochimica Acta* **74**, 784-798 (2010).

S35 Longhi, J. & Pan, V. The parent magmas of the SNC meteorites. *Proceedings of the Nineteenth Lunar and Planetary Science Conference*, 451-464 (1989).

S36 Matzen, A. K., Baker, M. B., Beckett, J. R. & Stolper, E. M. Fe–Mg partitioning between olivine and high-magnesian melts and the nature of Hawaiian parental liquids. *Journal of Petrology* **52**, 1243-1263 (2011).

S37 Matzen, A. K., Baker, M. B., Beckett, J. R. & Stolper, E. M. The Temperature and Pressure Dependence of Nickel Partitioning between Olivine and Silicate Melt. *Journal of Petrology* **54**, 2521-2545 (2013).

S38 Menzies, A. *et al.* Peridotitic mantle xenoliths from kimberlites on the Ekati Diamond Mine property, N.W.T., Canada: major element compositions and implications or the lithosphere beneath the central Slave craton. *Lithos* **77**, 395-412 (2004).

S39 Mitchell, R. H. Garnet lherzolites from the Hanaus-I and Louwrensia kimberlites of Namibia. *Contributions to Mineralogy and Petrology* **86**, 178-188 (1984).

S40 Musselwhite, D. S., Dalton, H. A., Kiefer, W. S. & Treiman, A. H. Experimental petrology of the basaltic shergottite Yamato-980459: Implications for the thermal structure of the Martian mantle. *Meteoritics & Planetary Science* **41**, 1271-1290 (2006).

S41 Mysen, B. O. & Dubinsky, E. V. Melt structure control on olivine/melt element partitioning of Ca and Mn. *Geochimica et Cosmochimica Acta* **68**, 1617-1633 (2004).

S42 Parman, S. W., Dann, J. C., Grove, T. L. & deWit, M. J. Emplacement conditions of komatiite magmas from the 3.49 Ga Komati Formation, Barberton Greenstone Belt, South Africa. *Earth and Planetary Science Letters* **150**, 303-323 (1997).

S43 Parman, S. W. & Grove, T. L. Harzburgite melting with and without H2O: Experimental data and predictive modeling. *Journal of Geophysical Research* **109**, B02201 (2004).

S44 Sisson, T. W. & Grove, T. L. Temperatures and H2O contents of low-MgO high-alumina basalts. *Contributions to Mineralogy and Petrology* **113**, 167-184 (1993).

S45 Takagi, D., Sato, H. & Nakagawa, M. Experimental study of a low-alkali tholeiite at 1–5 kbar: optimal condition for the crystallization of high-An plagioclase in hydrous arc tholeiite. *Contributions to Mineralogy and Petrology* **149**, 527-540 (2005).

S46 Thy, P., Lesher, C. E. & Fram, M. S. in *Proceedings of the Ocean Drilling Program, Scientific Results* Vol. 152 (eds A. D. Saunders, H.C. Larsen, & S.W. Jr. Wise) 359-372 (Ocean Drilling Program, College Station, TX 1998).

S47 Tuff, J. & O'Neill, H. S. C. The effect of sulfur on the partitioning of Ni and other first-row transition elements between olivine and silicate melt. *Geochimica et Cosmochimica Acta* **74**, 6180-6205 (2010).

S48 Tuff, J., Takahashi, E. & Gibson, S. A. Experimental constraints on the role of garnet pyroxenite in the genesis of high-Fe mantle plume derived melts. *Journal of Petrology* **46**, 2023-2058 (2005).

S49 Wagner, T. P. & Grove, T. L. Experimental constraints on the origin of lunar high-Ti ultramafic glasses. *Geochimica et Cosmochimica Acta* **61**, 1315-1327 (1997).

S50 Wang, Z. & Gaetani, G. A. Partitioning of Ni between olivine and siliceous eclogite partial melt: experimental constraints on the mantle source of Hawaiian basalts. *Contributions to Mineralogy and Petrology* **156**, 661-678 (2008).

S51 Witt-Eickschen, G., Palme, H., O'Neill, H. S. C. & Allen, C. M. The geochemistry of the volatile trace elements As, Cd, Ga, In and Sn in the Earth's mantle: New evidence from in situ analyses of mantle xenoliths. *Geochimica et Cosmochimica Acta* **73**, 1755-1778 (2009).

S52 Yang, H.-J., Kinzler, R. J. & Grove, T. L. Experiments and models of anhydrous, basaltic olivine-plagioclase-augite saturated melts from 0.001 to 10 kbar. *Contributions to Mineralogy and Petrology* **124**, 1-18 (1996).